Cell Reports

Article

Structures of the human adult muscle-type nicotinic receptor in resting and desensitized states

Graphical abstract

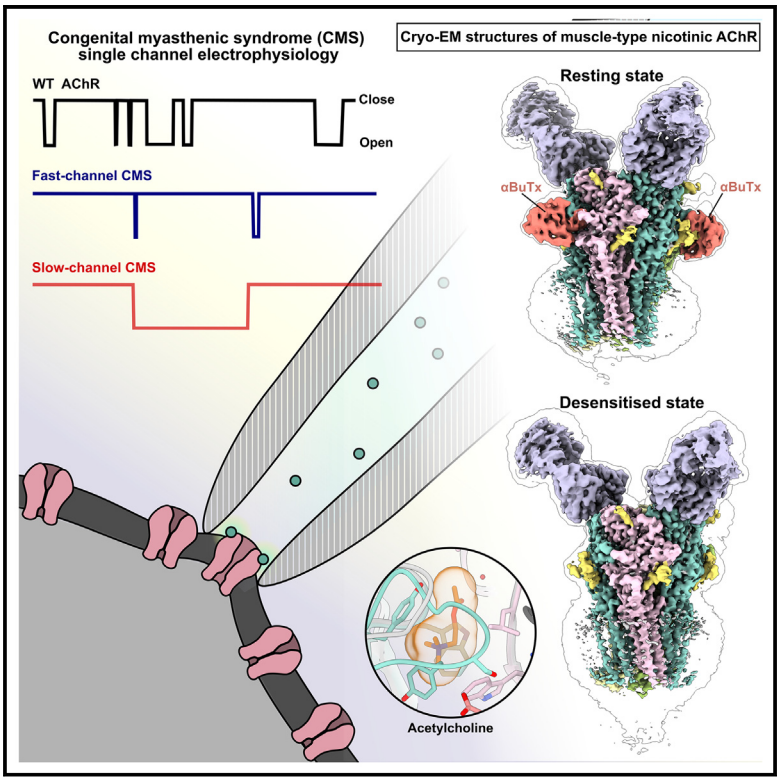

Highlights

- Expression of the human adult muscle-type AChR using a stable cell line
- Cryo-EM structures show conformational changes during recovery from desensitization
- Electrophysiological characterization of unreported congenital myasthenic syndrome variants
- N-terminal ATCUN sequence motif of the α subunit is capable of coordinating Cu^{2+}

Authors

Anna Li, Ashley C.W. Pike, Richard Webster, ..., David Beeson, David B. Sauer, Yin Yao Dong

Correspondence

anna.li@ndcn.ox.ac.uk (A.L.), yin.dong@ndcn.ox.ac.uk (Y.Y.D.)

In brief

Mutations in the muscle-type AChR are associated with a rare neuromuscular disorder known as congenital myasthenic syndrome (CMS). Li et al. report the cryo-EM structures of human adult muscle-type AChR in resting and desensitized states and provide structural explanations for eight unreported CMS variants causing gain or loss of function in AChR.

Li et al., 2025, Cell Reports *44*, 115581
May 27, 2025
https://doi.org/10.1016/j.celrep.2025.115581

CellPress

Cell Reports

CellPress
OPEN ACCESS

Article

Structures of the human adult muscle-type nicotinic receptor in resting and desensitized states

Anna Li,[1,2,*] Ashley C.W. Pike,[2] Richard Webster,[1] Susan Maxwell,[1] Wei-Wei Liu,[1] Gamma Chi,[2] Jacqueline Palace,[1,3] David Beeson,[1] David B. Sauer,[2] and Yin Yao Dong[1,4,*]

[1]Nuffield Department of Clinical Neurosciences, University of Oxford, OX3 9DS Oxford, UK
[2]Centre for Medicines Discovery, Nuffield Department of Medicine, University of Oxford, OX3 7FZ Oxford, UK
[3]Neurology Department, John Radcliffe Hospital, OX3 9DU Oxford, UK
[4]Lead contact
*Correspondence: anna.li@ndcn.ox.ac.uk (A.L.), yin.dong@ndcn.ox.ac.uk (Y.Y.D.)
https://doi.org/10.1016/j.celrep.2025.115581

SUMMARY

Muscle-type nicotinic acetylcholine receptor (AChR) is the key signaling molecule in neuromuscular junctions. Here, we present the structures of full-length human adult receptors in complex with Fab35 in α-bungarotoxin (αBuTx)-bound resting states and ACh-bound desensitized states. In addition to identifying the conformational changes during recovery from desensitization, we also used electrophysiology to probe the effects of eight previously unstudied AChR genetic variants found in patients with congenital myasthenic syndrome (CMS), revealing they cause either slow- or fast-channel CMS characterized by prolonged or abbreviated ion channel bursts. The combined kinetic and structural data offer a better understanding of both the AChR state transition and the pathogenic mechanisms of disease variants.

INTRODUCTION

Acetylcholine receptor (AChR) is a pentameric ligand-gated ion channel (pLGIC) found clustered on the post-synaptic membrane of neuromuscular junctions. Consisting of four different subunits (α, β, δ, and γ or ε), it is the most complex pLGIC by subunit heterogeneity. At the neuromuscular junction, the binding of ACh drives the transition from resting to open state, which results in the depolarization of the membrane and, eventually, muscle contraction. Subsequent dissociation of ACh causes the receptor to return to the resting state. Occasionally, high ACh concentrations may prolong the open state of AChR and prompt its transition to a non-conductive desensitized state, and this mechanism safeguards the post-synaptic membrane from overstimulation. In the neuromuscular junctions of developing mammals, AChR undergoes subunit switching, where its fetal γ subunit is substituted by an ε subunit, resulting in an adult-type receptor ($\alpha_2\beta\delta\varepsilon$) with shorter burst durations and higher single-channel conductance.[1,2]

Abnormalities in neuromuscular signaling lead to myasthenia (fatigable muscle weakness), which can affect all voluntary muscles in the body. When respiratory muscles are affected, patients may be at risk of myasthenic crises and, in rare cases, even death. Myasthenia can be caused by an autoimmune attack, in the case of myasthenia gravis, or genetic defects in proteins of the neuromuscular junction, in the case of congenital myasthenic syndrome (CMS). The prevalence of CMS varies between 2 and 22 per 1,000,000 people worldwide[3–6] and is most commonly driven by a mutation in AChR for half of all cases.[7,8] Variants in AChR genes can lead to CMS by three major pathogenic mechanisms—reduced receptor surface expression (AChR-deficiency syndrome), prolonged AChR activity (slow-channel CMS [SCCMS]), or abbreviated AChR activity (fast-channel CMS [FCCMS]).[9] Strategies for treating FCCMSs, SCCMSs, and AChR-deficiency syndrome are distinct and sometimes contraindicated; therefore, a correct diagnosis is vitally important.[10] As of 2024, at least 42 CMS-related missense variants have been reported to affect AChR kinetics.[7,11–20]

While protein structures are often key to understanding protein function or the effects of pathogenic mutations, structural study of the muscle-type AChR is particularly challenging due to difficulties in the recombinant expression of hetero-multimeric channels. Accordingly, existing receptor structures are of orthologs purified from native tissues. Receptor structures from the *Torpedo* electric ray have served as prototypes for AChR since the first 9 Å reconstruction in 1993, revealing its overall architecture, as well as its modulation by ligands, anesthetics, and toxins.[21–27] More recently, bovine AChR structures have shed light on structural components contributing to the different electrophysiological signatures of its fetal and adult isoforms.[28–35] Despite these advances, the structure of human muscle-type AChR remains elusive. Critically, the sequence of bovine AChR is only 92% identical to the human receptor, and this difference may affect the interpretation of AChR variants in relation to diseases such as CMS.

To address this ambiguity in the structure and function of human AChR, we resolved the structures of the human muscle-type receptor ($\alpha_2\beta\delta\varepsilon$) in α-bungarotoxin (αBuTx)-bound resting states and ACh-bound desensitized states using cryoelectron microscopy (cryo-EM). By comparing the two states of AChR, we uncovered structural changes associated with its recovery from desensitization. In addition, we used single-channel electrophysiology and structural models to understand the molecular consequences of eight CMS-causing AChR variants.

RESULTS

Structure of the resting-state human $\alpha_2\beta\delta\varepsilon$ AChR

In order to assemble an adult muscle-type AChR for structural and functional analyses, we generated a doxycycline-inducible cell line that simultaneously expresses human wild-type (WT) α, β, and δ subunits along with an ε subunit containing an enhanced green fluorescent protein (EGFP) insertion into the M3-M4 intracellular loop to monitor protein expression. After confirming that the receptor was properly folded and assembled, we obtained cell-attached single-channel recordings of this stable cell line, which showed WT AChR-like conductance and kinetics (Figures 1A and 1B), consistent with previous recordings of the transient expression of the same construct[36] and functional neuromuscular junctions in transgenic mice.[37] Recombinant AChR was solubilized in a detergent mixture of 1% n-dodecyl-β-D-maltopyranoside (DDM) and 0.1% cholesteryl hemisuccinate and then purified to homogeneity using a bromoacetylcholine affinity column (BAC), made by conjugating ligand onto Sepharose beads, followed by size-exclusion chromatography (Figure S1; Table S1). For cryo-EM, we added a Fab fragment of an anti-α IgG1 fragment (Fab35)[38] to act as a fiducial label and break the receptor's 5-fold pseudosymmetry.

To obtain a resting-like structure of AChR, purified protein was incubated before vitrification on cryo-EM grids with αBuTx, an 8 kDa α-neurotoxin from *Bungarus multicinctus* venom that prevents channel activation.[39,40] While AChR pentamers bound to either two Fabs or one Fab were present during cryo-EM data processing (Figure S2), likely a result of complex dissociation at the air-water interface during sample vitrification, we could nevertheless observe well-resolved structural features and side chains within these maps. To better resolve the mobile transmembrane domain (TMD), the two Fab subsets of particles were further classified based on TMD conformation (Figure S2). Ultimately, despite the significant compositional and structural heterogeneity present, we were able to select a subset of particles that yielded a 2.96 Å reconstruction (Table S2). The protein was well resolved throughout its extracellular domain (ECD), TMD, and intracellular domain (ICD). In general, the map quality enabled the modeling of the protein in the experimental map using N-glycans and identifiable sequence motifs to identify each chain, numbering each modeled chain after excluding the signal peptide, confirming we had captured the expected stoichiometry of $\alpha_2\beta\delta\varepsilon$.

The human AChR structure retains the classical architecture described for the previously reported *Torpedo* and bovine structures[21–28] (Figures S3A–S3E). The receptor subunits are arranged in the clockwise order α-β-δ-α-ε when viewed from the synaptic cleft (Figures 1C and 1D), with one Fab35 bound to the N terminus of each α subunit. The αBuTx binding sites are at the α-ε and α-δ extracellular interfaces, which coincide with the two orthosteric sites (Figures 1C and 1D). The ECD of each subunit consists of a β sandwich (β1–β10), followed by four membrane-spanning helices (M1–M4), with the M2 helix lining the pore. The C terminus of the M3 helix is followed by the MX helix that lies parallel to the inner leaflet of the plasma membrane. The MX helix then transitions into a disordered intracellular loop that becomes helical once more at the intracellular MA helix that precedes the M4 helix. We refer to the unresolved region between M3 and M4 helices as the M3-M4 loop.

Surprisingly, we observed poor occupancy of αBuTx in the Coulomb potential map, with the α-δ interface being the higher occupancy site (Figure S4A). We hypothesize that this partial occupancy of αBuTx was due to the reduced affinity of the detergent-solubilized receptor for the toxin. We also noted weak TMD density, corresponding to mobility in that domain, likely due to detergent molecules destabilizing the interhelical interactions in the TMD.[41] As these shortcomings in the detergent-solubilized AChR map make analyzing these regions difficult, we reconstituted the purified AChR into MSP2N2 lipidic nanodiscs to create a more native-like environment and collected a second cryo-EM dataset. We isolated particles of AChR in nanodiscs, which produced a 2.48 Å reconstruction map, with 2 Fabs bound and clear density for the distinctively shaped long C-terminal tail on the δ subunit that is similar to structural homologs (Figure S5; Table S2).[24] In this structure, both αBuTx binding sites were fully occupied, but the receptor's TMD and ICD appeared more dynamic than the detergent-solubilized structure, with no resolvable density for the ICD's MX and MA helices (Figures S6A–S6C and 1E).

In our αBuTx-bound structures, residues αBuTx-R36 and αBuTx-Y32 extend into the aromatic cage of the binding site, lined by αW149, αY190, αY198, and δW57 or εW55 (Figure 1F). We noted that the αBuTx binding mode to the human receptor is similar to that of the *Torpedo* receptor, consistent with having highly conserved interacting residues (Figures S3F–S3H).[42,43] The αBuTx competes with ACh and stabilizes the open conformation of α loop C, thus trapping the receptor in the resting state. The guanidinium group of αBuTx-R36 is sandwiched between αBuTx-F32 of the toxin and αY198 in a stacked cation-π interaction. Comparing the δ and ε subunits, we noted residue differences between the two ligand binding sites. On the δ subunit, δE59 on β2 strand forms a salt bridge with δK163 on loop F, while δE59 is also hydrogen bonded to αBuTx-S34. The equivalent salt bridge is reversed on the ε subunit, with εK34 of β1 strand and εD173 of loop F, while its hydrogen bond contact with αBuTx-S34 is maintained by εK34 (Figures 1F and 1G).[42,43]

Structural changes between desensitized and resting states

We next sought to characterize the structural changes between resting, desensitized, and possibly open states. Samples were prepared in nanodiscs as before, replacing αBuTx in the sample buffer with either 1 mM ACh to induce desensitization or a trio of 100 μM ACh, positive allosteric modulator (PAM), and fluoxetine

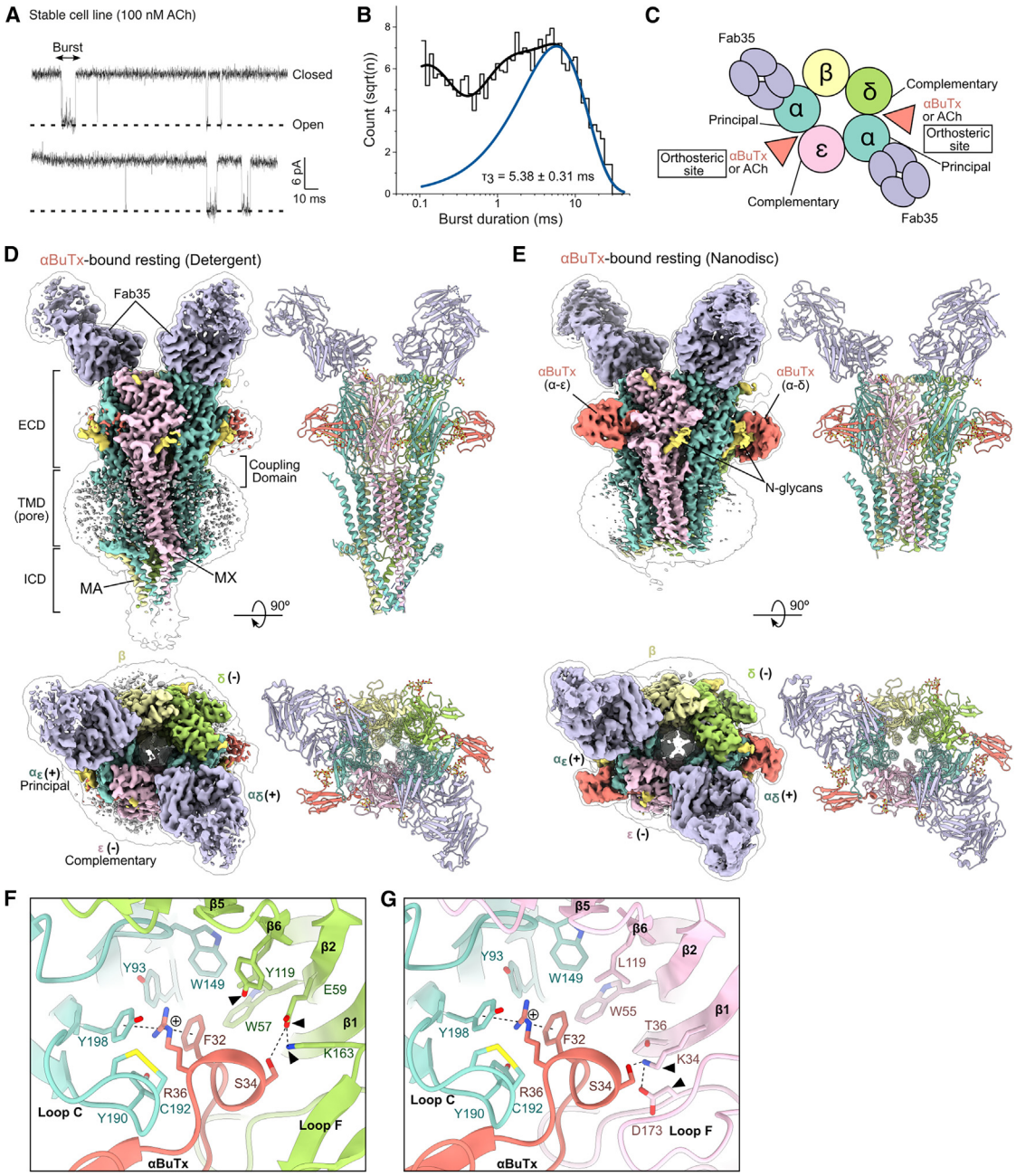

Figure 1. AChR in the αBuTx-bound resting state

(A and B) Single-channel currents and burst duration histograms produced by AChR-expressing stable cell line at +80 mV in the presence of 100 nM ACh, τ_3 = 5.38 ± 0.31 ms, n = 4.

(C) Schematic of AChR stoichiometry when viewed from the synapse. Orthosteric sites are formed by the principal α subunit and the complementary δ/ε subunit.

(D and E) Cryo-EM structures of the detergent- and nanodisc-reconstituted αBuTx-bound receptor.

(F and G) Comparison of αBuTx binding to the α-δ and α-ε interfaces in the nanodisc structure. Black triangles indicate key non-conserved residues in δ/ε subunits; cation-π interactions are denoted by dotted lines.

ECD, extracellular domain; TMD, transmembrane domain; ICD, intracellular domain.

in an attempt to stabilize the open state (see STAR Methods). The 100 μM ACh dataset gave rise to a 2.73 Å reconstruction, while the 1 mM ACh dataset produced a 2.64 Å map (Figures S7 and S8; Table S2). The 1 mM ACh dataset suffered from severe preferential orientation of the particles, resulting in the poor resolution of the TMD (Figures S6D and S4). Analyses of the 100 μM ACh-PAM-fluoxetine (Figure 2A) and 1 mM ACh structures revealed that both were bound to ACh only

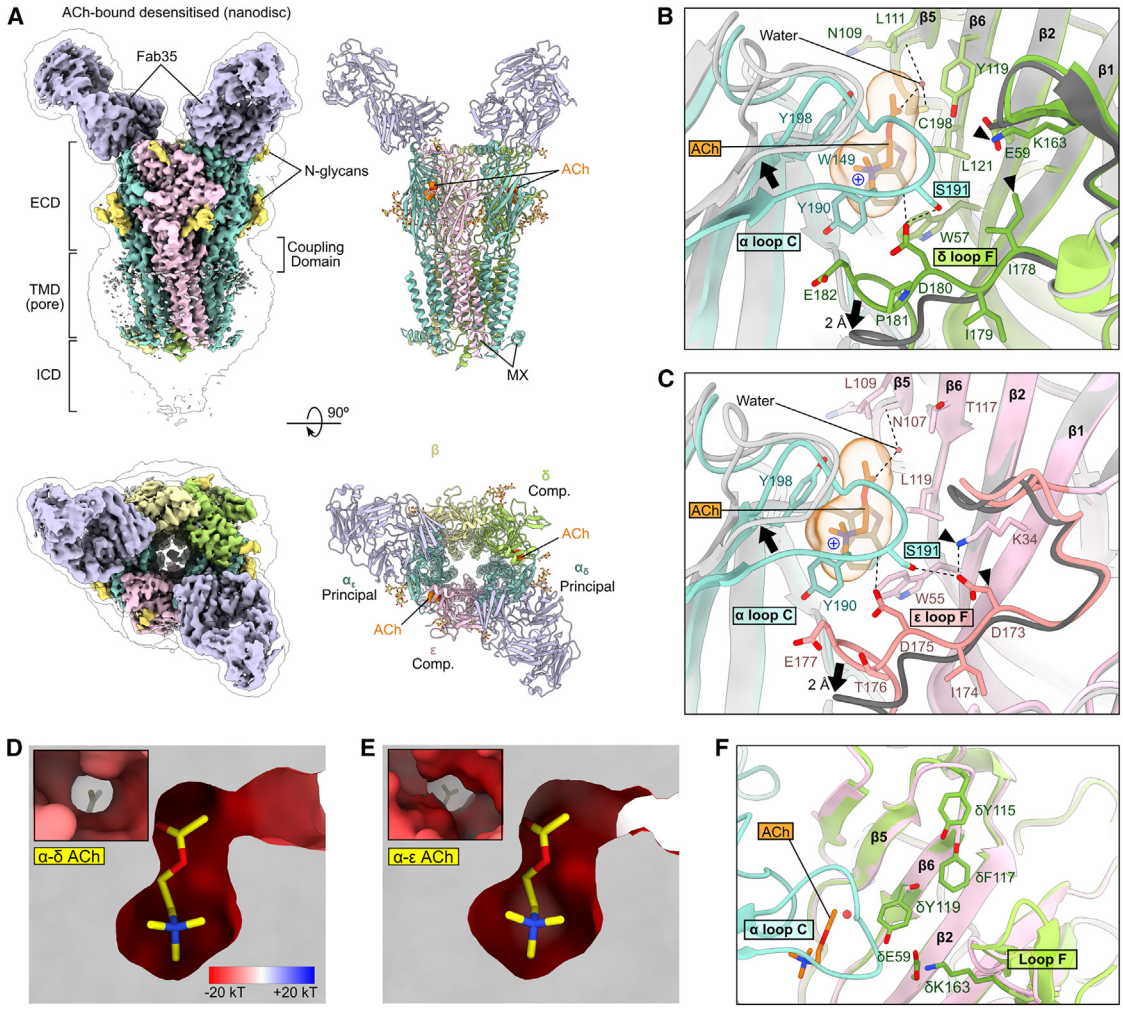

Figure 2. ACh binding sites in the desensitized state

(A) Cryo-EM structure of the nanodisc-reconstituted ACh-bound receptor.

(B and C) ACh binding site is stabilized by hydrogen bonding between αS191 and δ/ε loop F. For comparison, the resting-state structure in detergent is shown in gray, with an overall RMSD = 0.878 Å. Black triangles indicate differences between δ and ε subunits, and black arrows indicate the direction of movement associated with structural changes from the desensitized to the resting state.

(D and E) ACh binding site is more occluded and less electronegative at the α-δ site than the α-ε site.

(F) Bulky residues (δY115, δF117, δY119, δE59, and δK163) within 15 Å of the α-δ ACh binding site (the equivalent ε residues are εG113, εS115, εT117, εG57, and εA161).

(Figure S4B) and adopted identical desensitized conformations (root-mean-square deviation [RMSD] = 0.856 Å; Figures S3B and S9A), which we attributed to being a desensitized conformation because of a high degree of similarity with published desensitized structures (Figures S3B and S3D). Thus, the addition of PAM and fluoxetine failed to trap the receptor in an open state, and the binding sites for both compounds could not be elucidated. Our observed weak TMD density may also be caused by the previously noted collapsed pore phenomenon for purified heteromeric pLGICs,[44,45] which may be caused by the suboptimal composition of the membrane mimetic.[46–49]

The ACh binding sites are formed by α loop C on the principal α subunit and β strands β2, β5, and β6 on the complementary δ/ε subunits, with the pocket enclosed by the interaction between α loop C and δ/ε loop F (Figures 2). Compared to the αBuTx-bound structure, ACh binding is accompanied by the complete closure of α loop C, and this action is blocked by αBuTx binding. The positively charged tertiary amine group of ACh is stabilized by cation-π interactions with αY190, αW149, and αY198 on the principal subunit and with εW55 or δW57 on the complementary subunit. The acetyl group of ACh is coordinated by a water at both α-δ and α-ε orthosteric sites. These structural waters mediate an interaction between the carbonyl group of ACh and the mainchain carbonyl of εN107. Notably, the pose of ACh is slightly different from that of a bovine AChR structure, due to an intact disulfide between αC192 and αC193 in our human AChR structure, whereas the equivalent bond is broken in the bovine receptor structure[28] (Figures S3I and S3J).

The closed conformation of α loop C in the ACh-bound state is stabilized by a hydrogen bond network between αS191 on loop C and acidic residues on δ/ε loop F, a role that was previously described in AChR ortholog structures to stabilize the closed conformation of α loop C (Figures 2B and 2C).[26,28,50] Notably, the ε subunit contains one more acidic residue than the δ subunit, with this charge introduced by εD173. The ACh binding cavity appeared less occluded and more electronegative at the α-ε interface (Figures 2D and 2E). The occlusion at the α-δ site may be attributed to the five bulky residues δY115, δF117, δY119, δE59, and δK163 within 13 Å of the bound ACh at the α-δ site, while the equivalent residues εG113, εS115, εT117, εG57, and εA161 on the ε subunit are smaller (Figure 2F). The bovine AChR contains the same key residues at the α-δ and α-ε interfaces except for a serine-to-alanine substitution at αS191, resulting in the loss of hydrogen bonding between α loop C and δ/ε loop F.

Our aBuTx- and ACh-bound receptor structures show differences beyond the orthosteric site, revealing how local changes at this site transmit to the TMD via the coupling domain. In the desensitized structure, we identified a key hydrogen bond interaction between αS266 of the M2-M3 loop and εE184/δE189 of loop F (Figures 3A–3C).[51] The acidic loop F residues are also involved in a conserved tripartite salt bridge of εR218, εE184, εD45, and εD138 at the base of the ECD (Figures 3B and 3C). Interestingly, the αS266-εE184 hydrogen bond is observed only in the desensitized state, but the αS266-δE189 interaction persists in both resting and desensitized states. We hypothesize that the structural transition from a desensitized state back to a resting state involves first the dissociation of ACh, followed by the concerted opening of α loop C and a 2 Å downward movement of δ/ε loop F, uncoupling the hydrogen bond between αS191 and loop F of the δ or ε subunits (Figures 2B and 2C, dotted lines). These conformational changes are transmitted down to the coupling domain, which leads to αS266 of the M2-M3 loop moving away from the δE189/εE184, also on loop F (Figures 3B and 3C, yellow arrows). Moreover, the α_{δ} M2-M3 loop undergoes a 2 Å shift at αS266 and a 4 Å shift for the same residue on α_{ε}, thus contributing to the asymmetrical conformational changes within the AChR pentamer. Ultimately, M2-M3 loops propagate the signal of ACh binding to the TMD, where the alignment of five M2 helices determines the channel's ion permeability.

By convention, residues in the M2 helices of pLGICs are numbered from −1′ on the intracellular side, equivalent to αE241, to 20′ on the extracellular side, equivalent to αE262. For the αBuTx-bound structure, its pore is narrow throughout, which contains a 2.9 Å constriction at the 9′ hydrophobic gate (Figure 3D). In contrast, the desensitized ACh-bound channel has a funnel-shaped pore, wider at the 9′ position with a pore diameter of 6 Å, which tapers to a 4.2 Å constriction at the 6′ position (Figures 3D and 3E). Both pore conformations are similar to the corresponding resting and desensitized states of bovine and *Torpedo* receptors[24,26,28] (Figure S9). In our structures of the desensitized human AChR, the wider 9′ gate results from the five leucine residues rotating away from the pore axis (Figure 3F). At the 6′ position, βF259 causes a visible kink in the permeation pathway in all three structures with well-resolved TMDs, forming the desensitization gate that excludes the passage of hydrated Na^+ ions. This finding is supported by the observed faster desensitization of a βF259S targeted mutant.[28] Apart from the rotation, the M2 helices also tilt away from the pore axis in the desensitized state, with tilt angles ranging from 3° to 7° (Figures 3F and S9I).[28]

Characterization of eight CMS variants

Using our human AChR structures, we next sought to understand the effects of eight previously unstudied CMS AChR kinetic variants gathered from many years of clinical surveillance (Table S3; Figure 4A). The variants were found to have a negligible effect on the surface expression of AChR, defined as ≥50% of the WT, indicating that altered AChR kinetics, rather than AChR deficiency, likely underlies these patients' syndrome (Figure 4B). Therefore, we used single-channel recordings and burst duration statistics of the variants to classify the dominant pathogenic mechanism as either FCCMS or SCCMS, thereby enabling tailored therapeutic intervention. Simply defined, FCCMS is characterized by shortened burst durations compared to the WT, while SCCMS is characterized by prolonged bursts (Figure 4C). Three variants, αT133I, βI285S, and δD180N, led to a reduction in the longest time constant of AChR burst duration (1.86 ± 0.13, 1.81 ± 0.29, and 1.05 ± 0.04 ms) compared to WT (5.61 ± 0.38 ms) (Figures 4D and 4E; Table S4). The remaining five substitutions severely prolong the AChR bursts, with time constants ranging from 18.11 ± 2.43 ms for αT281S to 69.88 ± 0.07 ms for εS235A (Figures 4D and 4E; Table S4). While most of these CMS variants did not alter the single-channel conductance of AChR, the αI49T slow-channel variant resulted in markedly decreased current amplitudes at different holding potentials, with a single-channel conductance of 33 pS compared to 63 pS of the WT receptors (Figures 5A and 5B).

Examining our newly determined structures of human AChR to better understand the structural consequences of these variants, we found that three CMS variants are located within the ECD of AChR (αI49T, δD180N, and αT133I). The majority of SCCMS variants are located in the AChR TMD, whereas FCCMS variants may be scattered across all domains[7] (Figure 4A; Table S5). The αI49T variant, which causes SCCMS and a reduced conductance, is found in the extracellular vestibule and 11 Å from M2-M3 of the coupling domain (Figure 5C). Though its surroundings remain mostly static between desensitized and resting states, the introduction of a threonine increases the polarity of this region in the ion permeation pathway, though ultimately, how this causes such drastic changes in channel kinetics and conductance is unclear. Another fast-channel variant, δD180N altered the charge of the key δD180 loop F residue responsible for stabilizing α loop C in the ACh-bound state (Figure 2B), providing a structural explanation for its loss-of-function characteristics. A previously identified variant at the equivalent εD175N position also causes FCCMS.[52] The third FCCMS variant, αT133I, is in the Cys loop and immediately adjacent to the previously reported αV132L, which also causes fast-channel syndrome[53] (Figure 5D). Both αT133I and αV132L appear to exert their effects by increasing the hydrophobicity of the Cys loop, which may affect its coupling with the M2-M3 loop.

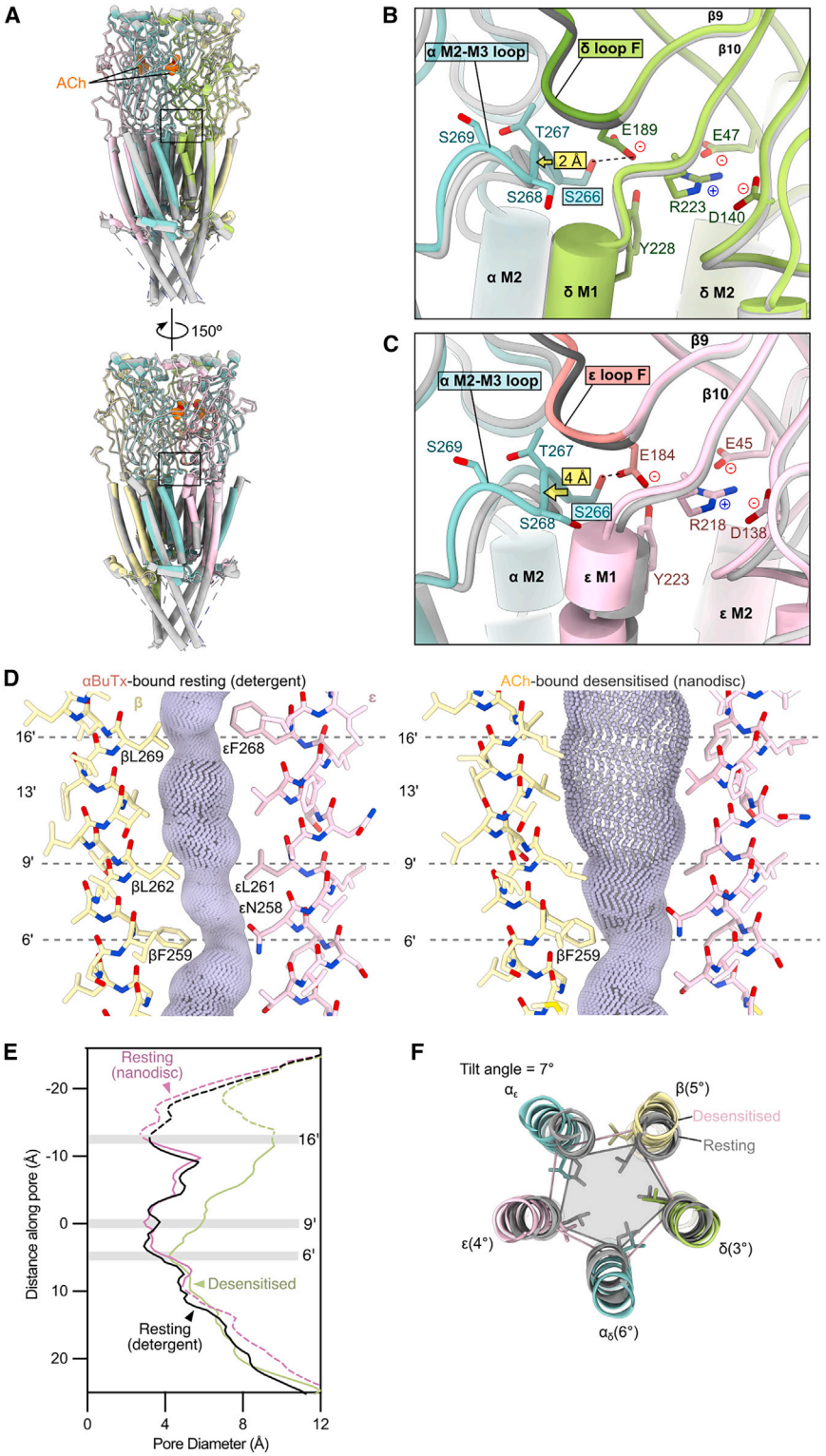

Figure 3. Structural transitions between desensitized and resting states

(A) Structural overlay of desensitized (colored) and resting (gray) states, with an overall RMSD = 0.859 Å. Boxes highlight the positions of inter-subunit interactions in the coupling domain.

(B) Hydrogen bonding between αS266 and δE189 as part of a tripartite salt bridge on the complementary subunit (δR223-E189-E47-D140).

(C) The same interaction between αS266 and εE184 at the equivalent position.

(D and E) Comparison of pore profiles of resting and desensitized states. Dashed lines in (E) indicate regions where some side-chain positions could not be experimentally determined but were reinstated for the purposes of profile generation (see STAR Methods).

(F) Pore dilation is achieved by 9′ leucine residues rotating away from central axis, accompanied by outward tilting of the M2 helices: 7° (α_ε), 5° (β), 3° (δ), 6° (α_δ), and 4° (ε).

See Figure S9.

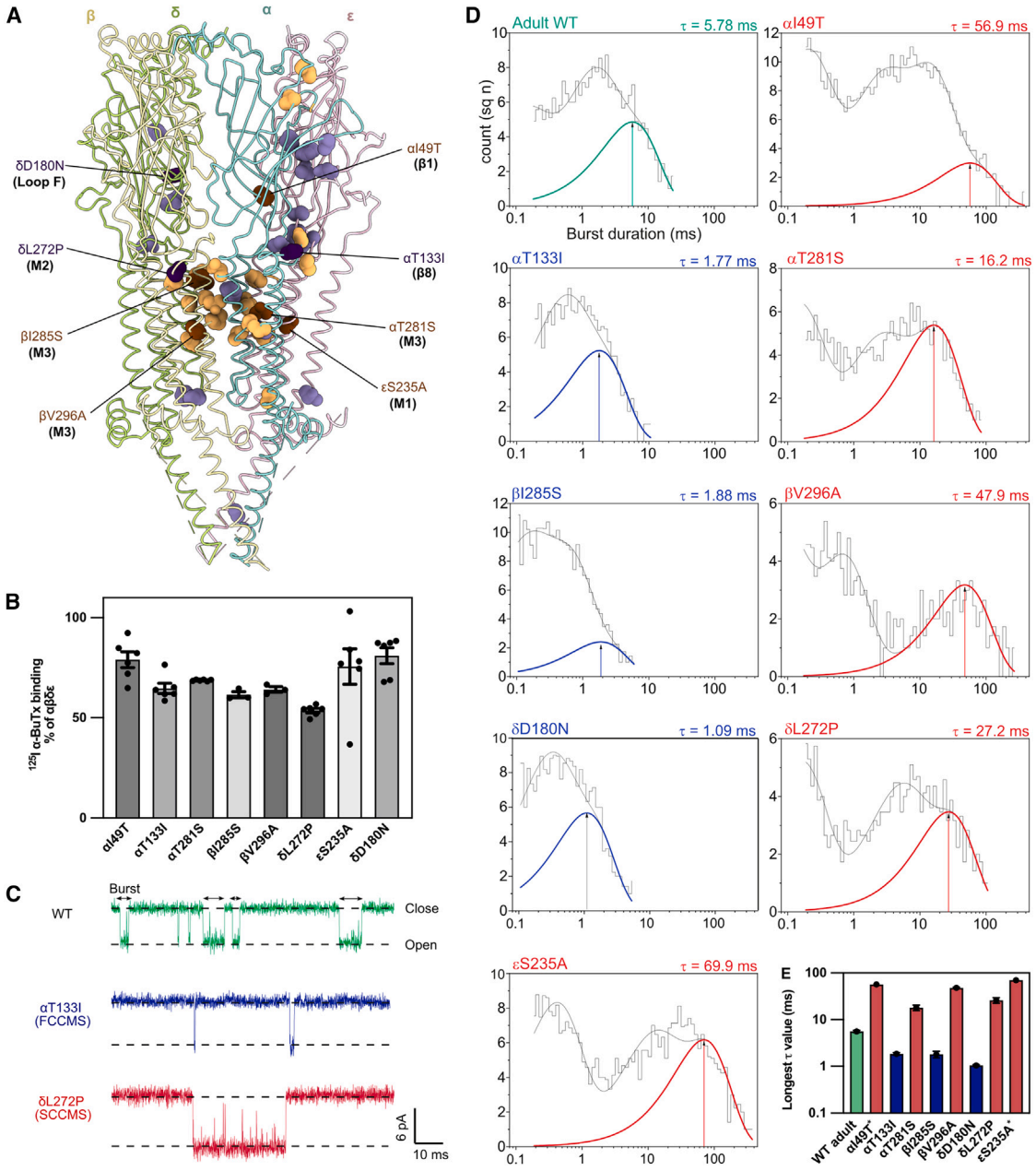

Figure 4. Characterization of CMS kinetic variants

(A) Locations of SCCMS (brown/orange spheres) and FCCMS (purple/lilac spheres) variants mapped onto the detergent-reconstituted resting-state structure.[7,11–19] Variants reported in this study are highlighted in a darker shade and labeled, and the α_δ subunit was omitted for clarity. See Table S5 for the full list of CMS variants on the diagram.

(B) Surface expression of CMS variants in transfected HEK293 cells measured by ^{125}I-αBuTx binding assay. Measurements were normalized to the expression of WT receptors, $n \geq 3$, mean ± SEM.

(C) Representative single-channel currents of WT, fast-channel variants (αT281I), and slow-channel variants (δL272P) at +80 mV holding potential in the presence of 100 nM extracellular ACh, $n \geq 4$. Channel openings are upward deflections.

(D) Burst duration histograms fitted with sum of exponentials for WT, slow-channel variants (αI49T, αT281S, βV296A, δL272P, and εS235A) in red, and fast-channel variants (αT133I, βI285S, and δD180N) in blue. The δD180N variant was recorded with 500 nM instead of 100 nM ACh.

(E) Summary bar chart of the longest burst duration time constant (τ) extracted from the histograms; the y axis scale is adjusted to $\log_{10}$. Data are presented as mean ± SEM except for the entries indicated with asterisks (*), which had fitting error instead of SEM (see Table S4).

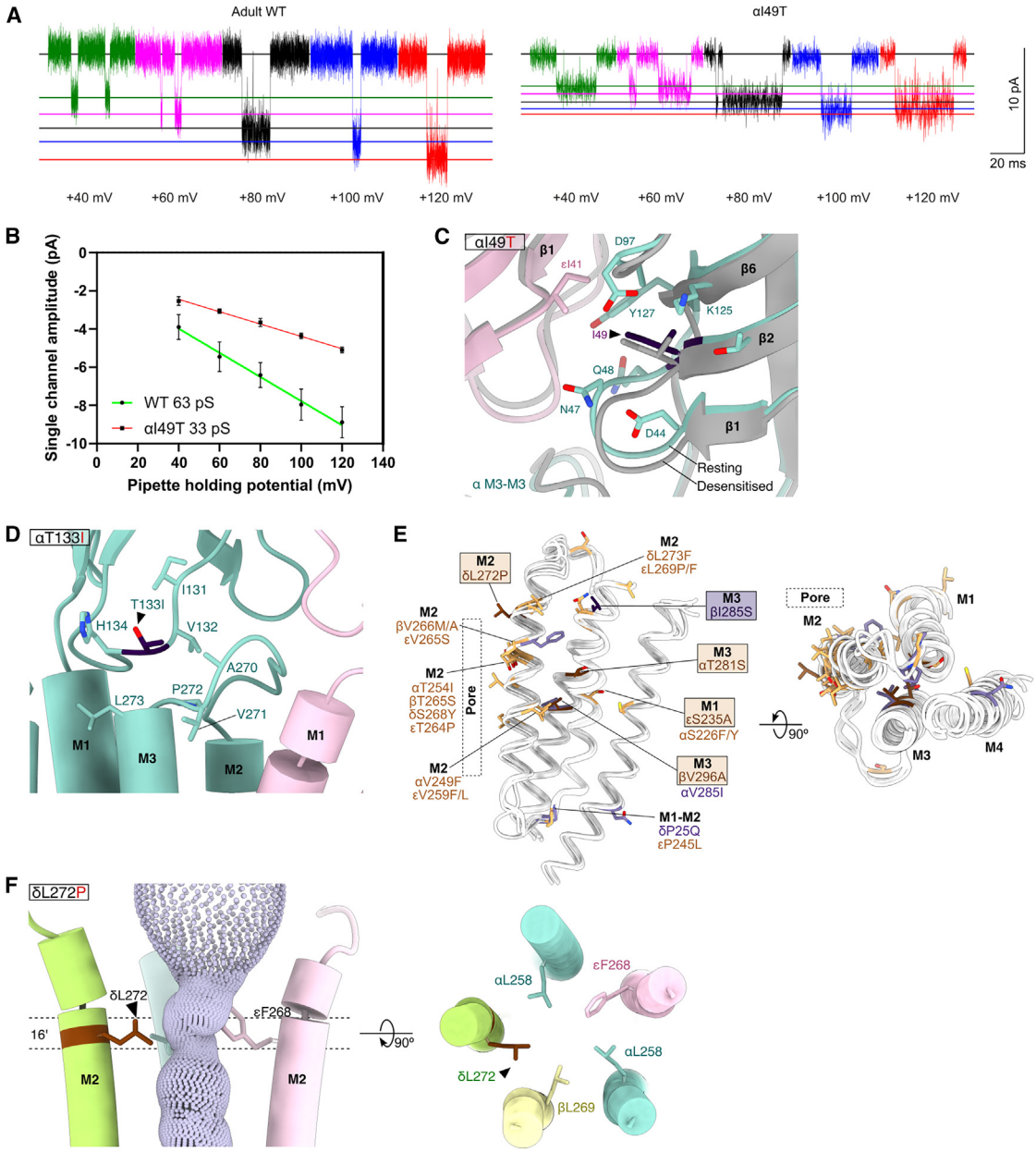

Figure 5. Structural analysis of CMS kinetic variants

(A and B) αI49T reduces AChR single-channel conductance from 63 ± 11 (WT) to 33 ± 3 pS, mean ± SEM. Current amplitudes of bursts recorded at +40 to +120 mV were plotted in a current-voltage curve, and single-channel conductance was the slope of its linear regression.

(C) αI49T at the extracellular vestibule does not undergo large conformational changes between resting and desensitized (gray) states.

(D) αT133I is located at the coupling domain.

(E) Mapping of CMS kinetic variants found in the transmembrane domain; FCCMS in purple, SCCMS in orange. Variants are shown on superposed TMDs.

(F) δL272P replaces a side chain at the 16′ pore constriction.

The remaining five CMS variants are located within the TMD: εS235A in M1, δL272P in M2, and βI285S, βV296A, and δL272P in M3 (Figure 5E). Firstly, the δL272P slow-channel variant removes a key side chain at the 16′ constriction of the pore while possibly disrupting the helicity within M2 through the introduction of more conformationally restricted amino acids (Figure 5F). This pore-facing side of the M2 helix is a slow-channel hotspot (Figure 5E), with the SCCMS variants αT254I, βT265S, δS268Y, and εT264P at the 13′ position, which lies one helix turn below δL272P. Similarly, βL262M is located a further helix turn away at the 9′ hydrophobic gate.[7] This suggests that missense variants in M2 likely affect channel gating by altering its ability to rotate open or shut in response to ACh binding.

Similar to the M2 SCCMS variants clustering on that helix, we noted that the εS235A variant on M1 coincides with the αS226F and αS226Y SCCMS variants on the α subunit.[7] Furthermore, of the βI285S, βV296A, and αT281S FCCMS variants on M3 described here, βV296A is located at the equivalent position of the αV285I FCCMS variant on the α subunit.[54] Notably, most M1 and M3 kinetic variants face the hydrophobic core of the four transmembrane helix bundles and are likely to affect proper helix packing and alignment.

N terminus of the α subunit contains a metal-binding motif

In examining our AChR structures determined on copper grids, the αBuTx-bound structure in nanodiscs and 100 μM ACh in nanodiscs, we observed strong non-protein density at the N terminus of the α_δ subunit (Figures 6A, 6B, and S10A). Its residues, 1–3, adopt a square planar arrangement, with their backbone nitrogen and a fourth nitrogen from the H3 imidazole group coordinating an unknown ion, which presumably is a Cu^{2+} derived from the EM grid (Figures 6B and S10). In contrast, the same residues in the detergent-solubilized αBuTx-bound sample on gold grids exhibit an open conformation (Figure 6C). This was immediately reminiscent of the amino-terminal copper and nickel (ATCUN) sequence motif X1-X2-H3, which was first described to coordinate divalent cations in human serum albumin.[55] This sequence motif is found only on the muscle-specific α1 subunit as S1-E2-H3 after the removal of the signal peptide, and it is conserved in both bovine and *Torpedo* orthologs (Figure 6D). Based on the location of the ATCUN sites within the structure, metal binding may be influenced by Fab35 binding, as well as the neighboring ε and β subunits (Figures 6E and S10).

Recombinantly expressed AChR can assemble into multiple stoichiometries

When processing the cryo-EM dataset of detergent-solubilized AChR, we isolated channels with subunit compositions other than the expected $\alpha_2\beta\delta\varepsilon$, indicating that multiple hetero-pentamer species were expressed in the recombinant cell line. To identify the oligomers present in our sample, we used ModelAngelo[57] to automatically identify and build the various well-resolved classes, and the results were confirmed by visual inspection of regions with distinctive protein side chains (Figures 7A and 7B). We identified particle subclasses with $\alpha_3\varepsilon_2$ (Figures 7C and 7D), where tilting of the ε M4 and a poorly resolved TMD suggest that this receptor has a collapsed pore and is likely non-functional. We also identified a tentatively assigned $\alpha_2\beta\delta_2$ subclass with a well-resolved TMD and ICD (Figures 7E and 7F). To probe whether this $\alpha_2\beta\delta_2$ receptor is functional on the cell surface, we transfected HEK293 cells with cDNAs encoding only the α, β, and δ subunits and observed ACh-elicited single-channel currents with current amplitudes between those of adult WT and fetal WT receptors (Figure 7G). This demonstrates that functional receptors can form on the cell surface without the ε/γ subunit. However, both automated subunit assignment using ModelAngelo and visual analysis indicated sequence ambiguities in its second δ subunit (in place of ε), which suggests a mixed δ/ε population at this subunit position (Figure 7F). Further classification was unable to resolve a complete "clean" $\alpha_2\beta\delta_2$. Nevertheless, this suggests that other AChR pentamers may be present at the human neuromuscular junction or, alternately, receptor assembly at the NMJ is regulated by proteins absent in our HEK293-based expression system.

Structural determinants of adult versus fetal AChR

The muscle-type AChR transitions from a fetal receptor to an adult receptor during development.[59] As both adult and fetal receptors consist of the same α, β, and δ subunits, functional differences, such as the adult receptor's shorter burst duration and higher conductance, are mostly down to the sequence differences between ε versus γ subunits, which are 48% non-identical (Figures S11A, in blue, and S12). Previous studies suggested that residues in the β5-β6 hairpin of the ε ECD dictate the adult receptor's open probability,[60] and acidic residues in the ε ICD contribute to its higher channel conductance.[28] We set out to investigate other regions of notable structural differences between the fetal and adult receptors. We used the structure of the bovine γ subunit (PDB: 9AWK) to guide this analysis, as it has an identical sequence to human AChR in loop F and the M2-M3 loop[28] (Figure S12). Examining our structures of the adult isoform AChR, we identified three ε-specific motifs that warrant further investigation: an εK34-εD173 salt bridge, an εC190-εC470 disulfide bond, and an εS280 M2-M3 loop residue that interacts with εT133 of the Cys loop (Figures S11A–S11C).

Firstly, we noted an εK34-εD173 salt bridge and an analogous interaction at δE59-δK163 earlier (Figures 1F and 1G). This salt bridge is replaced by γK34-γE163 in the fetal subunit, with an equivalent lysine residue of εK34 but a different acidic residue (Figure S11A). To test the importance of the εK34-εD173 interaction, we introduced the γ acidic residue by the εD163E substitution and, in a separate experiment, combined it with a second εD173F mutation to knock out the ε acidic residue. The εD173F mutation severely reduced surface expression, whereas the double mutant has 60% ± 2% of the surface expression of WT receptors (Figure S11D), and it did not alter the receptor's burst duration (Figure S11E; Table S4). Secondly, an ε-specific εC190-εC470 disulfide bond links its C terminus to the ECD (Figure S11A), and the same bond is observed on an ε-containing bovine AChR structure.[11] We found that the εC190A substitution severely reduced receptor expression, which corroborated a previous study that probed the other cysteine residue via an εC470A mutation.[26] Thirdly, we focused on an M2-M3 loop residue, εS280, which interacts with εT133 of the Cys loop (Figure S11C). Substituting εS280 to alanine, as present in the γ subunit, caused a marked reduction in AChR surface expression (Figure S11D). We conclude that all three sites on the ε subunit are key to receptor expression, though due to the low expression, we were unable to assess the effects on channel kinetics of εD173F, εC190A, and εS280A.

DISCUSSION

Conformational changes between desensitized and resting states

Comparisons between our desensitized- and resting-state structures reveal new insights into the conformational changes

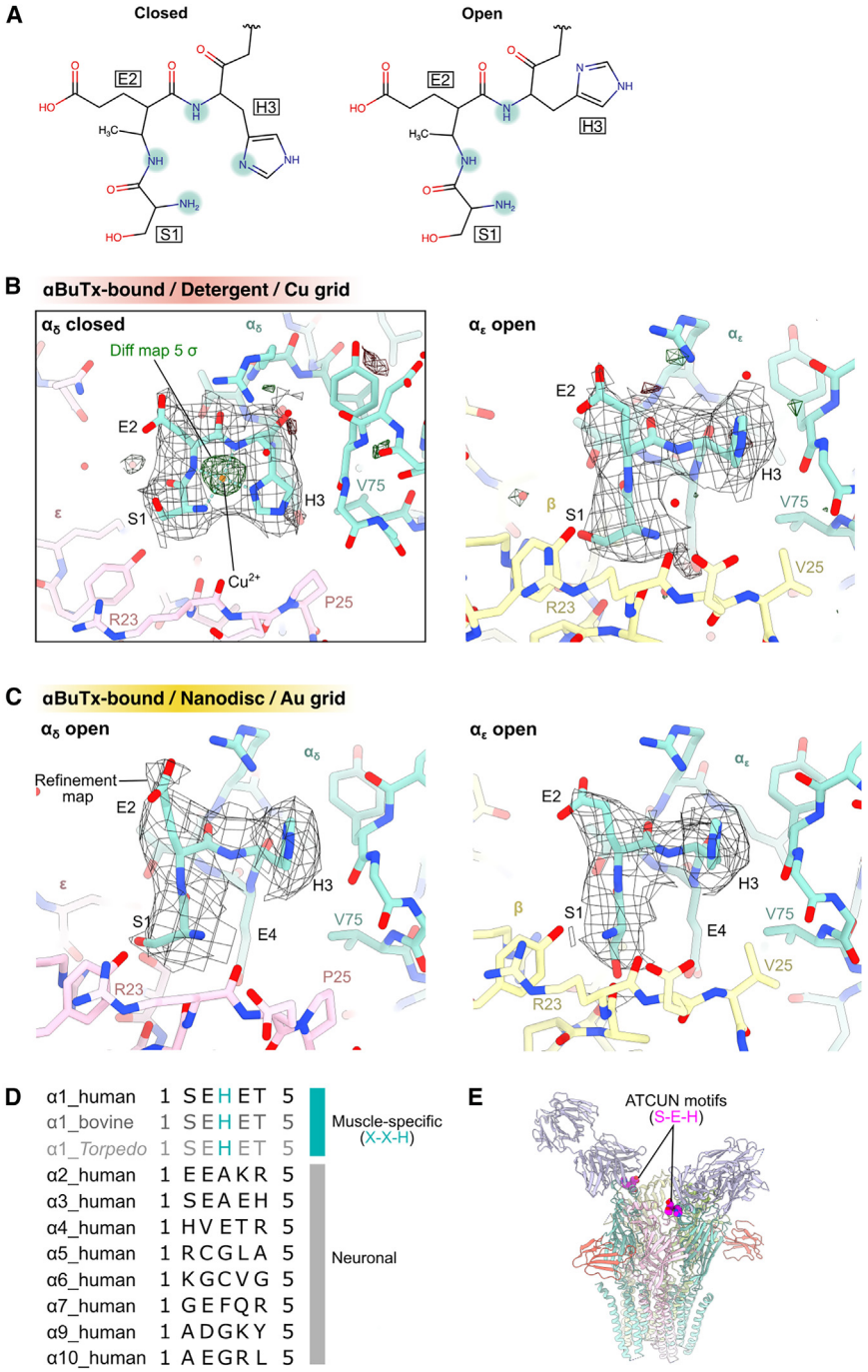

Figure 6. N terminus of the α subunit contains a metal-binding motif

(A) Schematic of the X1-X2-H3 amino-terminal Cu^{2+} and Ni^{2+} (ATCUN) motif in ion-coordinating (closed) and open conformations.

(B and C) Comparison of ATCUN conformations at the α_δ-ε and α_ε-β interfaces in structures solved from copper (in nanodiscs) versus gold (in detergent) cryo-EM grids. Coulomb potential maps are shown in gray, and mask-normalized F_o-F_c difference maps highlighting non-protein features are shown in green (positive density) and red (negative density), calculated with Servalcat (see STAR Methods).

(D) Comparison of N-terminal sequence of AChR α subunits. Sequences were sourced from UniProt[56] with signal peptides omitted.

(E) ATCUN motifs are located at the N terminus of the α subunits near Fab35 binding sites.

See Figure S10.

between desensitized and resting states. We found that the uncoupling of ACh is associated with asymmetrical movements in the two α M2-M3 loops away from δ or ε loop F, with distinct effects on the interactions between αS266 and δE189 or αS266 and εE184 (Figures 3B and 3C). The importance of the larger structural change at the αS266-δE189 interaction is supported by experimental mutation αS266A reducing AChR activity by 4-fold[51] and the FCCMS εE184K variant's effects on channel kinetics.[14] In contrast, an δE189A experimental mutation did not alter AChR function.[51] Therefore, we propose that the α-δ and α-ε interactions are non-equivalent, despite the sequence and structural homology of the δ and ε subunits. Additionally, our observation of another inter-subunit hydrogen bond between αS191 of loop C and δ/ε loop F, near the bound ACh, agrees with previous reports that this interaction stabilizes the closed conformation of the orthosteric site.[26,28,50,52] Thus, loop F is an important component of signal transduction between the orthosteric sites and the coupling domain.

Structural insights into CMS-causing variants

Inappropriate treatment of CMS will lead to disease deterioration and can be life threatening. Thus, the correct identification of AChR variants as a gain or loss of function is critical. The current gold standard for such identification is through functional assays such as single-channel electrophysiology, which requires specialized expertise and equipment that is not accessible to most clinics. While *in silico* prediction may provide a faster alternative, current technologies such as AlphaMissense are insufficient for clinical application in CMS due to an accuracy of 64% for predicting AChR missense variants.[61,62] Our cryo-EM structures and characterization of eight CMS variants provide valuable information to help construct such a tool in the future. For example, by mapping the positions of known FCCMS and SCCMS variants, we found that the variants are distributed differently across the AChR domains (Figures 4 and 5). FCCMS variants can be found throughout the

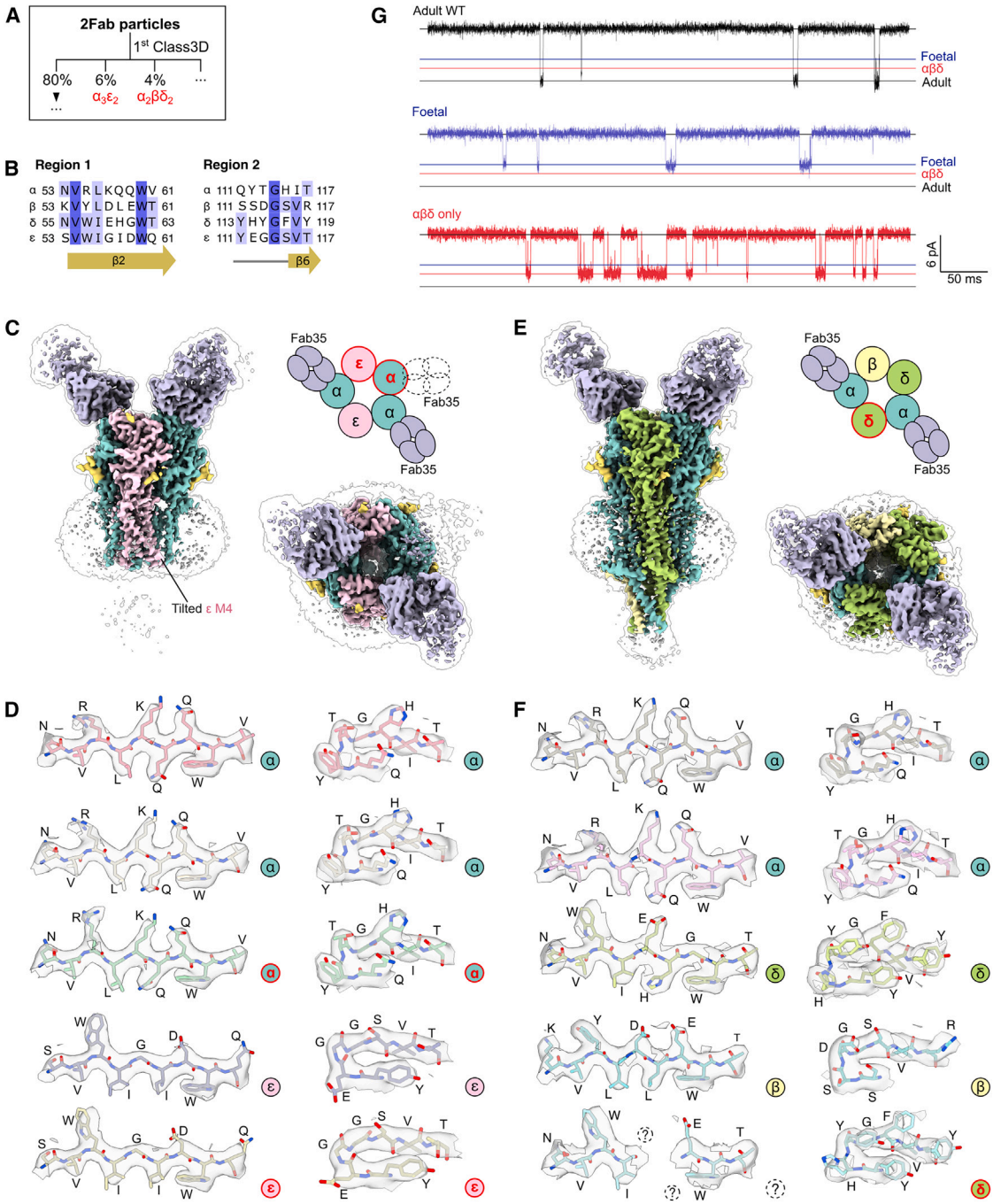

Figure 7. Recombinantly expressed AChR can assemble into multiple stoichiometries

(A) The $\alpha_3\varepsilon_2$ and $\alpha_2\beta\delta_2$ particles were isolated from the 2 Fab particles during RELION[58] Class3D of the detergent-solubilized cryo-EM dataset.

(B) Two ECD regions (equivalent to α53-61 and α111-117) with distinctive protein side chains were used for visual confirmation of subunit assignment. Structural models for $\alpha_3\varepsilon_2$ and $\alpha_2\beta\delta_2$ particle subclasses were built by ModelAngelo based on protein sequence and Coulomb potential maps.[27]

(C) A 3.2 Å map of $\alpha_3\varepsilon_2$ was reconstructed from 25,453 particles.

(D) Model-map agreement for $\alpha_3\varepsilon_2$ subunits in regions 1 and 2.

(E) A 3.2 Å map of predominantly $\alpha_2\beta\delta_2$ as reconstructed from 18,001 particles.

(F) Model-map agreement for $\alpha_2\beta\delta_2$ subunits in regions 1 and 2.

(G) Single-channel currents from HEK293T cells expressing adult WT (αβδε), fetal WT (αβδγ), or αβδ subunits at +80 mV with 100 nM ACh.

AChR, while SCCMS variants concentrate in the TMD.[7] We reported five kinetic CMS variants on M3 that likely affect helical packing (Figure 5E), yet our static structures alone are insufficient to explain the pathogenic mechanism of all the new variants we identified, most notably, why αI49T causes SCCMS and reduces channel conductance (Figures 5A–5C). Nevertheless, our findings provide an initial understanding of the mutants' physical effects. Building from these results and insights may enable the categorization of future *de novo* CMS variants in AChR.

Muscle-type AChR contains ion-coordinating ATCUN motifs

While unexpected, our structures provided a discovery of metal binding at the N terminus of the receptor's α subunits. We observed the α_δ ATCUN motif in an ion-bound conformation on structures obtained from copper grids (Figures 6B, S10A, and S10B), while it is in an open conformation on gold grids (Figure 6C). Intriguingly, the bound conformation of ATCUN has not been observed in the *Torpedo* or bovine AChR structures despite the sequence conservation, and the bovine AChR samples were also prepared on copper grids.[24,28] We propose that the proximity of Fab35 binding to the ATCUN motifs may help to stabilize the α N terminus to enable resolving this structural motif. Moreover, sequence differences between human and ortholog receptors adjacent to the ATCUN motifs may influence the site's affinity for divalent cations. In the case of the *Torpedo* receptor, an isoleucine at the equivalent position as αV75 could disfavor the closed conformation of residue H3. In the case of the bovine receptor, a glutamine instead of εR23 at the α_δ-ε interface causes the same effect. To further support our structural modeling, the bound AChR ATCUN motif also bears a striking resemblance to other ion-coordinating ATCUN structures, such as that of a Gly-Gly-His modified tripeptide,[63] with a backbone RMSD of 0.22 Å, and the c-Src-SH3 domain,[64] with a backbone RMSD of 0.31 Å (Figures S10C and S10D). Importantly, the functional significance of this newly identified metal-binding site unclear, as it is distinct from known divalent-cation-binding sites of other pLGICs.[65–67]

Assembly of muscle-type AChR subunits *in vitro*

Observations of the $\alpha_3\varepsilon_2$ and $\alpha_2\beta\delta_2$ pentamers in our overexpression system provide insights into AChR folding, assembly, and trafficking *in vitro*, as well as diagnosis of myasthenia gravis and CMS. These varied stoichiometries are of particular medical importance because cell-based assays are routinely used as diagnostic tests to detect anti-AChR antibodies in myasthenia gravis and for functional categorization of novel CMS variants.[10,68] Therefore, inconsistencies between the native tissue and experimental model system could lead to erroneous clinical guidance.

The existence of multiple AChR stoichiometries in recombinant cells highlights the complexity of receptor assembly. Notably, while chaperones such as RIC-3 and NACHO are required for the overexpression of certain neuronal AChRs,[69] no chaperones have been definitively associated with the muscle-type AChR. Therefore, it is unclear whether the observed $\alpha_3\varepsilon_2$ and $\alpha_2\beta\delta_2$ stoichiometries are due to the absence of a necessary chaperone in the HEK293 cells or reflect assemblies present but not previously identified at the neuromuscular junction. However, our single-channel recordings demonstrated that α-β-δ-containing receptors appeared to function as an ACh-gated channel (Figure 7E). Furthermore, ACh-elicited currents were also recorded from α-β-δ-containing receptors expressed in *Xenopus* oocytes,[70] and zebrafish knocked out for ε or γ subunits still produced synaptic currents at the neuromuscular junction.[71] This evidence suggests that the $\alpha_2\beta\delta_2$ receptor may play a physiological role *in vivo*.

Our observation of the $\alpha_3\varepsilon_2$ pentamer suggests that AChR can form stoichiometries that have not been reported previously. The presence of these various stoichiometries has implications for the possible assembly mechanisms of this pLGIC.[72] However, it is not possible to infer all the *in cellulo* subunit assemblies in this dataset, as the necessary protein purification by the BAC biases the final sample to channels with at least one ACh binding site.

Limitations of the study

To resolve the cryo-EM structures of AChR in the resting and desensitized states, we used detergent to extract the protein from the cell membrane, and for three out of four structures, we performed an additional reconstitution step to produce lipidic nanodiscs. We observed flexibility in the TMD, especially in the nanodisc samples, which may have prevented the resolution of any bound molecules from the cryo-EM map. More extensive method optimization may help to stabilize the TMD and therefore improve cryo-EM maps in the future. Additionally, we observed AChR pentamers with different subunit combinations within the cryo-EM dataset, which is an inherent limitation of recombinant protein expression. Apart from technical limitations, our results also highlighted areas demanding further investigation. For example, we could not explain why the SCCMS variant αI49T causes both prolonged burst duration and reduced single-channel conductance. We also discovered a divalent-cation-binding motif on the N terminus of the α subunits with unknown functional significance.

Conclusion

Here, we demonstrated the recombinant overexpression of functional human muscle-type AChR using a stable cell line in quantities sufficient for structural biology. Having captured the resting and desensitized states of AChR by cryo-EM, our results reveal the receptor's structural changes when converting from a desensitized to a resting state, in agreement with findings from previous ortholog structures.[21–28] Furthermore, our structures illuminate the underlying molecular pathophysiology of eight previously unstudied CMS variants. Finally, we identified a putative metal-binding ATCUN motif at the α subunit's N terminus, which may represent a possible regulatory site for AChR modulation by divalent cations. Ultimately, our models and results provide a new basis for understanding the structure-function relationship of the human AChR and may help explain the molecular pathogenic mechanism of more CMS variants in the future.

RESOURCE AVAILABILITY

Lead contact

Further information and requests for resources and reagents should be directed to and will be fulfilled by the lead contact, Yin Yao Dong (yin.dong@ndcn.ox.ac.uk).

Materials availability

All unique reagents generated in this study are available from the lead contact with a completed materials transfer agreement.

Data and code availability

- Data: the cryo-EM maps were deposited at the EM Data Bank under accession codes EMD-51568 (αBuTx-detergent), EMD-51569 (αBuTx-nanodisc), EMD-51570 (100 μM ACh-nanodisc), and EMD-51571 (1 mM ACh-nanodisc). The atomic models were deposited at the PDB under accession codes PDB: 9GU0 (αBuTx-detergent), 9GU1 (αBuTx-nanodisc), 9GU2 (100 μM ACh-nanodisc), and 9GU3 (1 mM ACh-nanodisc). They are publicly available as of the date of publication. Accession numbers are listed in the key resources table.
- Code: this paper does not report original code.
- Other items: any additional information required to reanalyze the data reported in this paper is available from the lead contact, Yin Yao Dong (yin.dong@ndcn.ox.ac.uk), upon request.

ACKNOWLEDGMENTS

We thank neuromuscular clinicians for referring AChR sequence variants to the "Oxford highly specialised clinical service for CMS" for functional analysis. We thank Hayley Spearman for conducting the initial surface expression experiments for the βV296A mutant; Professor Angela Vincent and Professor Alex Bullock, as well as members of the Yin Dong and David Sauer labs, for useful discussions; Dr. Karin Rödström for training A.L. to purify proteins; Professor Liz Carpenter for advice and help supervising A.L.; Dr. Philip Hublitz and his team at the Genome Engineering Facility in the WIMM for cloning the AChR lentiviral constructs; Dr. Ryan Beveridge at the Virus Screening Facility in the WIMM for generating the lentiviral particles and calculating the virus titer; Craig Waugh, Dr. Paul Sopp, and Kevin Clark for assisting with cell sorting at the WIMM FACS facility; Dr. Rod Chalk and Dr. Kavya Clement for assisting with LC-MS/MS analysis; and Professor Brian Marsden and Elizabeth Maclean (Center for Medicines Discovery) for cryo-EM support. Cryo-EM datasets were collected at the Oxford Particle Imaging Center (OPIC), Central Oxford Structural Molecular Imaging Center (COSMIC), and the Electron Bio-Imaging Centre (eBIC) inside Diamond Light Source (BAG proposal bi28713). We acknowledge funding from the Wellcome Trust (102161/Z/13/Z, studentship to A.L.). This research was funded in whole, or in part, by the UKRI Medical Research Council (grant numbers MR/S007180/1 & MR/Z504099/1 to Y.Y.D and MR/Y012623/1 to A.L., Y.Y.D., and D.B.S.). For the purpose of Open Access, the author has applied a CC BY public copyright licence to any Author Accepted Manuscript version arising from this submission. D.B.S. and A.C.W.P. were supported by the Innovative Medicines Initiative 2 Joint Undertaking (JU) under grant agreement no. 875510 (EUbOPEN). The JU receives support from the European Union's Horizon 2020 research and innovation programme, EFPIA, the Ontario Institute for Cancer Research, the Royal Institution for the Advancement of Learning McGill University, Kungliga Tekniska Högskolan, and Diamond Light Source Limited. OPIC is an Instruct-ERIC Centre funded by a Wellcome Trust JIF award (060208/Z/00/Z) and equipment grant (093305/Z/10/Z). COSMIC is supported by the Wellcome Trust (grant no. 201536), the EPA Cephalosporin Trust, and a Royal Society/Wolfson Foundation Laboratory Refurbishment grant (no. WL160052). Molecular graphics and analyses were performed with UCSF ChimeraX, developed by the Resource for Biocomputing, Visualization, and Informatics at the University of California, San Francisco, with support from National Institutes of Health R01-GM129325 and the Office of Cyber Infrastructure and Computational Biology, National Institute of Allergy and Infectious Diseases.

AUTHOR CONTRIBUTIONS

Y.Y.D. and A.L. designed the experiments. A.L. performed the cell line generation, protein production, and cryo-EM sample preparation and also drafted the manuscript. A.L., A.C.W.P., and G.C. conducted cryo-EM screening and data collection. A.L. and A.C.W.P. performed cryo-EM data analysis, model building, and structural analysis. R.W. performed single-channel electrophysiology. S.M. and W.-W.L. carried out mutagenesis cloning and surface expression assay. J.P. led the "Oxford Congenital MS." Y.Y.D., D.B.S., and D.B. obtained funding and supervised the research. A.L., D.B.S., A.C.W.P., and Y.Y.D. revised the manuscript with input from all authors.

DECLARATION OF INTERESTS

J.P. has received honorariums and grants from Argenx and Amplo Biotechnology and acknowledges partial funding to the trust by Highly Specialised Services NHS England. Y.Y.D. has received research funding from Argenx and Amplo Biotechnology.

STAR★METHODS

Detailed methods are provided in the online version of this paper and include the following:

SUPPLEMENTAL INFORMATION

Supplemental information can be found online at https://doi.org/10.1016/j.celrep.2025.115581.

Received: December 2, 2024
Revised: February 18, 2025
Accepted: March 28, 2025
Published: April 17, 2025

REFERENCES

1. Kopta, C., and Steinbach, J.H. (1994). Comparison of mammalian adult and fetal nicotinic acetylcholine receptors stably expressed in fibroblasts. J. Neurosci. *14*, 3922–3933. https://doi.org/10.1523/JNEUROSCI.14-06-03922.1994.
2. Mishina, M., Takai, T., Imoto, K., Noda, M., Takahashi, T., Numa, S., Methfessel, C., and Sakmann, B. (1986). Molecular distinction between fetal and adult forms of muscle acetylcholine receptor. Nature *321*, 406–411. https://doi.org/10.1038/321406a0.
3. Parr, J.R., Andrew, M.J., Finnis, M., Beeson, D., Vincent, A., and Jayawant, S. (2014). How common is childhood myasthenia? The UK incidence and prevalence of autoimmune and congenital myasthenia. Arch. Dis. Child. *99*, 539–542. https://doi.org/10.1136/archdischild-2013-304788.
4. Mihaylova, V., Scola, R.H., Gervini, B., Lorenzoni, P.J., Kay, C.K., Werneck, L.C., Stucka, R., Guergueltcheva, V., von der Hagen, M., Huebner, A., et al. (2010). Molecular characterisation of congenital myasthenic syndromes in Southern Brazil. J. Neurol. Neurosurg. Psychiatry *81*, 973–977. https://doi.org/10.1136/jnnp.2009.177816.

5. Natera-de Benito, D., Töpf, A., Vilchez, J.J., González-Quereda, L., Domínguez-Carral, J., Díaz-Manera, J., Ortez, C., Bestué, M., Gallano, P., Dusl, M., et al. (2017). Molecular characterization of congenital myasthenic syndromes in Spain. Neuromuscul. Disord. *27*, 1087–1098. https://doi.org/10.1016/j.nmd.2017.08.003.

6. Troha Gergeli, A., Neubauer, D., Golli, T., Butenko, T., Loboda, T., Maver, A., and Osredkar, D. (2020). Prevalence and genetic subtypes of congenital myasthenic syndromes in the pediatric population of Slovenia. Eur. J. Paediatr. Neurol. *26*, 34–38. https://doi.org/10.1016/j.ejpn.2020.02.002.

7. Engel, A.G., Shen, X.M., Selcen, D., and Sine, S.M. (2015). Congenital myasthenic syndromes: pathogenesis, diagnosis, and treatment. Lancet Neurol. *14*, 461. https://doi.org/10.1016/S1474-4422(15)00010-1.

8. Gilhus, N.E., Tzartos, S., Evoli, A., Palace, J., Burns, T.M., and Verschuuren, J.J.G.M. (2019). Myasthenia gravis. Nat. Rev. Dis. Primers *5*, 30. https://doi.org/10.1038/s41572-019-0079-y.

9. Vanhaesebrouck, A.E., Webster, R., Maxwell, S., Rodriguez Cruz, P.M., Cossins, J., Wickens, J., Liu, W.W., Cetin, H., Cheung, J., Ramjattan, H., et al. (2019). beta2-Adrenergic receptor agonists ameliorate the adverse effect of long-term pyridostigmine on neuromuscular junction structure. Brain *142*, 3713–3727. https://doi.org/10.1093/brain/awz322.

10. Rodriguez Cruz, P.M., Palace, J., and Beeson, D. (2018). The Neuromuscular Junction and Wide Heterogeneity of Congenital Myasthenic Syndromes. Int. J. Mol. Sci. *19*, 1677. https://doi.org/10.3390/ijms19061677.

11. Ohno, K., Quiram, P.A., Milone, M., Wang, H.L., Harper, M.C., Pruitt, J.N., 2nd, Brengman, J.M., Pao, L., Fischbeck, K.H., Crawford, T.O., et al. (1997). Congenital myasthenic syndromes due to heteroallelic nonsense/missense mutations in the acetylcholine receptor epsilon subunit gene: identification and functional characterization of six new mutations. Hum. Mol. Genet. *6*, 753–766. https://doi.org/10.1093/hmg/6.5.753.

12. Croxen, R., Hatton, C., Shelley, C., Brydson, M., Chauplannaz, G., Oosterhuis, H., Vincent, A., Newsom-Davis, J., Colquhoun, D., and Beeson, D. (2002). Recessive inheritance and variable penetrance of slow-channel congenital myasthenic syndromes. Neurology *59*, 162–168. https://doi.org/10.1212/wnl.59.2.162.

13. Peyer, A.K., Abicht, A., Heinimann, K., Sinnreich, M., and Fischer, D. (2013). Quinine sulfate as a therapeutic option in a patient with slow channel congenital myasthenic syndrome. Neuromuscul. Disord. *23*, 571–574. https://doi.org/10.1016/j.nmd.2013.04.001.

14. Shen, X.M., Brengman, J.M., Shen, S., Durmus, H., Preethish-Kumar, V., Yuceyar, N., Vengalil, S., Nalini, A., Deymeer, F., Sine, S.M., and Engel, A.G. (2018). Mutations causing congenital myasthenia reveal principal coupling pathway in the acetylcholine receptor epsilon-subunit. JCI Insight *3*, e97826. https://doi.org/10.1172/jci.insight.97826.

15. Shen, X.M., Milone, M., Wang, H.L., Banwell, B., Selcen, D., Sine, S.M., and Engel, A.G. (2019). Slow-channel myasthenia due to novel mutation in M2 domain of AChR delta subunit. Ann. Clin. Transl. Neurol. *6*, 2066–2078. https://doi.org/10.1002/acn3.50902.

16. Shen, X.M., Di, L., Shen, S., Zhao, Y., Neumeyer, A.M., Selcen, D., Sine, S.M., and Engel, A.G. (2020). A novel fast-channel myasthenia caused by mutation in beta subunit of AChR reveals subunit-specific contribution of the intracellular M1-M2 linker to channel gating. Exp. Neurol. *331*, 113375. https://doi.org/10.1016/j.expneurol.2020.113375.

17. Tawara, N., Yamashita, S., Takamatsu, K., Yamasaki, Y., Mukaino, A., Nakane, S., Farshadyeganeh, P., Ohno, K., and Ando, Y. (2021). Efficacy of salbutamol monotherapy in slow-channel congenital myasthenic syndrome caused by a novel mutation in CHRND. Muscle Nerve *63*, E30–E32. https://doi.org/10.1002/mus.27166.

18. Kondo, H., Tsuji, Y., Lee, T., Saito, Y., and Nishino, I. (2022). Severe congenital myasthenic syndrome with novel variants in the CHRND gene. Pediatr. Int. *64*, e15342. https://doi.org/10.1111/ped.15342.

19. Brugnoni, R., Maggi, L., Canioni, E., Moroni, I., Pantaleoni, C., D'Arrigo, S., Riva, D., Cornelio, F., Bernasconi, P., and Mantegazza, R. (2010). Identification of previously unreported mutations in CHRNA1, CHRNE and RAPSN genes in three unrelated Italian patients with congenital myasthenic syndromes. J. Neurol. *257*, 1119–1123. https://doi.org/10.1007/s00415-010-5472-0.

20. Dresser, L., Wlodarski, R., Rezania, K., and Soliven, B. (2021). Myasthenia Gravis: Epidemiology, Pathophysiology and Clinical Manifestations. J. Clin. Med. *10*, 2235. https://doi.org/10.3390/jcm10112235.

21. Unwin, N. (1993). Nicotinic acetylcholine receptor at 9 A resolution. J. Mol. Biol. *229*, 1101–1124. https://doi.org/10.1006/jmbi.1993.1107.

22. Miyazawa, A., Fujiyoshi, Y., and Unwin, N. (2003). Structure and gating mechanism of the acetylcholine receptor pore. Nature *423*, 949–955. https://doi.org/10.1038/nature01748.

23. Unwin, N. (2005). Refined structure of the nicotinic acetylcholine receptor at 4A resolution. J. Mol. Biol. *346*, 967–989. https://doi.org/10.1016/j.jmb.2004.12.031.

24. Rahman, M.M., Teng, J., Worrell, B.T., Noviello, C.M., Lee, M., Karlin, A., Stowell, M.H.B., and Hibbs, R.E. (2020). Structure of the Native Muscle-type Nicotinic Receptor and Inhibition by Snake Venom Toxins. Neuron *106*, 952–962.e5. https://doi.org/10.1016/j.neuron.2020.03.012.

25. Nys, M., Zarkadas, E., Brams, M., Mehregan, A., Kambara, K., Kool, J., Casewell, N.R., Bertrand, D., Baenziger, J.E., Nury, H., and Ulens, C. (2022). The molecular mechanism of snake short-chain alpha-neurotoxin binding to muscle-type nicotinic acetylcholine receptors. Nat. Commun. *13*, 4543. https://doi.org/10.1038/s41467-022-32174-7.

26. Rahman, M.M., Basta, T., Teng, J., Lee, M., Worrell, B.T., Stowell, M.H.B., and Hibbs, R.E. (2022). Structural mechanism of muscle nicotinic receptor desensitization and block by curare. Nat. Struct. Mol. Biol. *29*, 386–394. https://doi.org/10.1038/s41594-022-00737-3.

27. Goswami, U., Rahman, M.M., Teng, J., and Hibbs, R.E. (2023). Structural interplay of anesthetics and paralytics on muscle nicotinic receptors. Nat. Commun. *14*, 3169. https://doi.org/10.1038/s41467-023-38827-5.

28. Li, H., Teng, J., and Hibbs, R.E. (2024). Structural switch in acetylcholine receptors in developing muscle. Nature *632*, 1174–1180. https://doi.org/10.1038/s41586-024-07774-6.

29. Burke, S.M., Avstrikova, M., Noviello, C.M., Mukhtasimova, N., Changeux, J.P., Thakur, G.A., Sine, S.M., Cecchini, M., and Hibbs, R.E. (2024). Structural mechanisms of alpha7 nicotinic receptor allosteric modulation and activation. Cellule *187*, 1160–1176. https://doi.org/10.1016/j.cell.2024.01.032.

30. Prevost, M.S., Barilone, N., Dejean de la Batie, G., Pons, S., Ayme, G., England, P., Gielen, M., Bontems, F., Pehau-Arnaudet, G., Maskos, U., et al. (2023). An original potentiating mechanism revealed by the cryo-EM structures of the human alpha7 nicotinic receptor in complex with nanobodies. Nat. Commun. *14*, 5964. https://doi.org/10.1038/s41467-023-41734-4.

31. Noviello, C.M., Gharpure, A., Mukhtasimova, N., Cabuco, R., Baxter, L., Borek, D., Sine, S.M., and Hibbs, R.E. (2021). Structure and gating mechanism of the alpha7 nicotinic acetylcholine receptor. Cell *184*, 2121–2134. https://doi.org/10.1016/j.cell.2021.02.049.

32. Mukherjee, S., Erramilli, S.K., Ammirati, M., Alvarez, F.J.D., Fennell, K.F., Purdy, M.D., Skrobek, B.M., Radziwon, K., Coukos, J., Kang, Y., et al. (2020). Synthetic antibodies against BRIL as universal fiducial marks for single-particle cryoEM structure determination of membrane proteins. Nat. Commun. *11*, 1598. https://doi.org/10.1038/s41467-020-15363-0.

33. Gharpure, A., Teng, J., Zhuang, Y., Noviello, C.M., Walsh, R.M., Jr., Cabuco, R., Howard, R.J., Zaveri, N.T., Lindahl, E., and Hibbs, R.E. (2019). Agonist Selectivity and Ion Permeation in the alpha3beta4 Ganglionic Nicotinic Receptor. Neuron *104*, 501–511. https://doi.org/10.1016/j.neuron.2019.07.030.

34. Walsh, R.M., Jr., Roh, S.H., Gharpure, A., Morales-Perez, C.L., Teng, J., and Hibbs, R.E. (2018). Structural principles of distinct assemblies of the human alpha4beta2 nicotinic receptor. Nature *557*, 261–265. https://doi.org/10.1038/s41586-018-0081-7.

35. Morales-Perez, C.L., Noviello, C.M., and Hibbs, R.E. (2016). X-ray structure of the human alpha4beta2 nicotinic receptor. Nature *538*, 411–415. https://doi.org/10.1038/nature19785.

36. Ealing, J., Webster, R., Brownlow, S., Abdelgany, A., Oosterhuis, H., Muntoni, F., Vaux, D.J., Vincent, A., and Beeson, D. (2002). Mutations in congenital myasthenic syndromes reveal an epsilon subunit C-terminal cysteine, C470, crucial for maturation and surface expression of adult AChR. Hum. Mol. Genet. *11*, 3087–3096. https://doi.org/10.1093/hmg/11.24.3087.

37. Webster, R.G., Cossins, J., Lashley, D., Maxwell, S., Liu, W.W., Wickens, J.R., Martinez-Martinez, P., de Baets, M., and Beeson, D. (2013). A mouse model of the slow channel myasthenic syndrome: Neuromuscular physiology and effects of ephedrine treatment. Exp. Neurol. *248*, 286–298. https://doi.org/10.1016/j.expneurol.2013.06.012.

38. Tzartos, S.J., Rand, D.E., Einarson, B.L., and Lindstrom, J.M. (1981). Mapping of surface structures of electrophorus acetylcholine receptor using monoclonal antibodies. J. Biol. Chem. *256*, 8635–8645.

39. Changeux, J.P., Kasai, M., and Lee, C.Y. (1970). Use of a snake venom toxin to characterize the cholinergic receptor protein. Proc. Natl. Acad. Sci. USA *67*, 1241–1247. https://doi.org/10.1073/pnas.67.3.1241.

40. Chang, C.C., and Lee, C.Y. (1963). Isolation of Neurotoxins from the Venom of Bungarus Multicinctus and Their Modes of Neuromuscular Blocking Action. Arch. Int. Pharmacodyn. Ther. *144*, 241–257.

41. Popot, J.-L. (2018). Membrane Proteins in Aqueous Solutions : From Detergents to Amphipols. Biological and Medical Physics, Biomedical Engineering, 1st ed. (Springer International Publishing).

42. Vincent, A., Jacobson, L., and Curran, L. (1998). Alpha-Bungarotoxin binding to human muscle acetylcholine receptor: measurement of affinity, delineation of AChR subunit residues crucial to binding, and protection of AChR function by synthetic peptides. Neurochem. Int. *32*, 427–433. https://doi.org/10.1016/s0197-0186(97)00118-6.

43. Nayak, T.K., Bruhova, I., Chakraborty, S., Gupta, S., Zheng, W., and Auerbach, A. (2014). Functional differences between neurotransmitter binding sites of muscle acetylcholine receptors. Proc. Natl. Acad. Sci. USA *111*, 17660–17665. https://doi.org/10.1073/pnas.1414378111.

44. Zhu, S., Noviello, C.M., Teng, J., Walsh, R.M., Jr., Kim, J.J., and Hibbs, R.E. (2018). Structure of a human synaptic GABA(A) receptor. Nature *559*, 67–72. https://doi.org/10.1038/s41586-018-0255-3.

45. Laverty, D., Desai, R., Uchanski, T., Masiulis, S., Stec, W.J., Malinauskas, T., Zivanov, J., Pardon, E., Steyaert, J., Miller, K.W., and Aricescu, A.R. (2019). Cryo-EM structure of the human alpha1beta3gamma2 GABA(A) receptor in a lipid bilayer. Nature *565*, 516–520. https://doi.org/10.1038/s41586-018-0833-4.

46. Unwin, N. (2024). Influence of lipid bilayer on the structure of the muscle-type nicotinic acetylcholine receptor. Proc. Natl. Acad. Sci. USA *121*, e2319913121. https://doi.org/10.1073/pnas.2319913121.

47. Baenziger, J.E., Morris, M.L., Darsaut, T.E., and Ryan, S.E. (2000). Effect of membrane lipid composition on the conformational equilibria of the nicotinic acetylcholine receptor. J. Biol. Chem. *275*, 777–784. https://doi.org/10.1074/jbc.275.2.777.

48. Criado, M., Eibl, H., and Barrantes, F.J. (1982). Effects of lipids on acetylcholine receptor. Essential need of cholesterol for maintenance of agonist-induced state transitions in lipid vesicles. Biochemistry *21*, 3622–3629. https://doi.org/10.1021/bi00258a015.

49. Fong, T.M., and McNamee, M.G. (1986). Correlation between acetylcholine receptor function and structural properties of membranes. Biochemistry *25*, 830–840. https://doi.org/10.1021/bi00352a015.

50. Zarkadas, E., Pebay-Peyroula, E., Thompson, M.J., Schoehn, G., Uchański, T., Steyaert, J., Chipot, C., Dehez, F., Baenziger, J.E., and Nury, H. (2022). Conformational transitions and ligand-binding to a muscle-type nicotinic acetylcholine receptor. Neuron *110*, 1358–1370.e5. https://doi.org/10.1016/j.neuron.2022.01.013.

51. Thompson, M.J., Mansoub Bekarkhanechi, F., Ananchenko, A., Nury, H., and Baenziger, J.E. (2024). A release of local subunit conformational heterogeneity underlies gating in a muscle nicotinic acetylcholine receptor. Nat. Commun. *15*, 1803. https://doi.org/10.1038/s41467-024-46028-x.

52. Sine, S.M., Shen, X.M., Wang, H.L., Ohno, K., Lee, W.Y., Tsujino, A., Brengmann, J., Bren, N., Vajsar, J., and Engel, A.G. (2002). Naturally occurring mutations at the acetylcholine receptor binding site independently alter ACh binding and channel gating. J. Gen. Physiol. *120*, 483–496. https://doi.org/10.1085/jgp.20028568.

53. Shen, X.M., Ohno, K., Tsujino, A., Brengman, J.M., Gingold, M., Sine, S.M., and Engel, A.G. (2003). Mutation causing severe myasthenia reveals functional asymmetry of AChR signature cystine loops in agonist binding and gating. J. Clin. Investig. *111*, 497–505. https://doi.org/10.1172/JCI16997.

54. Wang, H.L., Milone, M., Ohno, K., Shen, X.M., Tsujino, A., Batocchi, A.P., Tonali, P., Brengman, J., Engel, A.G., and Sine, S.M. (1999). Acetylcholine receptor M3 domain: stereochemical and volume contributions to channel gating. Nat. Neurosci. *2*, 226–233. https://doi.org/10.1038/6326.

55. Noormagi, A., Golubeva, T., Berntsson, E., Warmlander, S., Tougu, V., and Palumaa, P. (2023). Direct Competition of ATCUN Peptides with Human Serum Albumin for Copper(II) Ions Determined by LC-ICP MS. ACS Omega *8*, 33912–33919. https://doi.org/10.1021/acsomega.3c04649.

56. UniProt Consortium (2023). UniProt: the Universal Protein Knowledgebase in 2023. Nucleic Acids Res. *51*, D523–D531. https://doi.org/10.1093/nar/gkac1052.

57. Jamali, K., Käll, L., Zhang, R., Brown, A., Kimanius, D., and Scheres, S.H.W. (2024). Automated model building and protein identification in cryo-EM maps. Nature *628*, 450–457. https://doi.org/10.1038/s41586-024-07215-4.

58. Zivanov, J., Nakane, T., Forsberg, B.O., Kimanius, D., Hagen, W.J., Lindahl, E., and Scheres, S.H. (2018). New tools for automated high-resolution cryo-EM structure determination in RELION-3. Elife *7*, e42166. https://doi.org/10.7554/eLife.42166.

59. Hesselmans, L.F., Jennekens, F.G., Van den Oord, C.J., Veldman, H., and Vincent, A. (1993). Development of innervation of skeletal muscle fibers in man: relation to acetylcholine receptors. Anat. Rec. *236*, 553–562. https://doi.org/10.1002/ar.1092360315.

60. Nayak, T.K., Chakraborty, S., Zheng, W., and Auerbach, A. (2016). Structural correlates of affinity in fetal versus adult endplate nicotinic receptors. Nat. Commun. *7*, 11352. https://doi.org/10.1038/ncomms11352.

61. Cheng, J., Novati, G., Pan, J., Bycroft, C., Žemgulytė, A., Applebaum, T., Pritzel, A., Wong, L.H., Zielinski, M., Sargeant, T., et al. (2023). Accurate proteome-wide missense variant effect prediction with AlphaMissense. Science *381*, eadg7492. https://doi.org/10.1126/science.adg7492.

62. Ryan-Phillips, F., Henehan, L., Ramdas, S., Palace, J., Beeson, D., and Dong, Y.Y. (2024). Assessing the Utility of ColabFold and AlphaMissense in Determining Missense Variant Pathogenicity for Congenital Myasthenic Syndromes. Biomedicine *12*, 2549. https://doi.org/10.3390/biomedicines12112549.

63. Camerman, N., Camerman, A., and Sarkar, B. (1976). Molecular design to mimic the copper(II) transport site of human albumin. The crystal and molecular structure of copper(II) – glycylglycyl-L-histidine-N-methyl amide monoaquo complex. Can. J. Chem. *54*, 1309–1316. https://doi.org/10.1139/v76-185.

64. Camara-Artigas, A. (, Bacarizo, J., (2015). Crystal structure of the c-Src-SH3 domain in complex with the high affinity peptide VSL12. https://doi.org/10.2210/pdb4RTZ/pdb.

65. Miller, P.S., Da Silva, H.M.A., and Smart, T.G. (2005). Molecular basis for zinc potentiation at strychnine-sensitive glycine receptors. J. Biol. Chem. *280*, 37877–37884. https://doi.org/10.1074/jbc.M508303200.

66. Hubbard, P.C., and Lummis, S.C. (2000). Zn(2+) enhancement of the recombinant 5-HT(3) receptor is modulated by divalent cations.

Eur. J. Pharmacol. *394*, 189–197. https://doi.org/10.1016/s0014-2999(00)00143-6.

67. Smart, T.G., and Constanti, A. (1990). Differential effect of zinc on the vertebrate GABAA-receptor complex. Br. J. Pharmacol. *99*, 643–654. https://doi.org/10.1111/j.1476-5381.1990.tb12984.x.
68. Lazaridis, K., and Tzartos, S.J. (2020). Autoantibody Specificities in Myasthenia Gravis; Implications for Improved Diagnostics and Therapeutics. Front. Immunol. *11*, 212. https://doi.org/10.3389/fimmu.2020.00212.
69. Matta, J.A., Gu, S., Davini, W.B., and Bredt, D.S. (2021). Nicotinic acetylcholine receptor redux: Discovery of accessories opens therapeutic vistas. Science *373*, eabg6539. https://doi.org/10.1126/science.abg6539.
70. Jackson, M.B., Imoto, K., Mishina, M., Konno, T., Numa, S., and Sakmann, B. (1990). Spontaneous and agonist-induced openings of an acetylcholine receptor channel composed of bovine muscle alpha-beta- and delta-subunits. Pflügers Archiv *417*, 129–135. https://doi.org/10.1007/BF00370689.
71. Mongeon, R., Walogorsky, M., Urban, J., Mandel, G., Ono, F., and Brehm, P. (2011). An acetylcholine receptor lacking both gamma and epsilon subunits mediates transmission in zebrafish slow muscle synapses. J. Gen. Physiol. *138*, 353–366. https://doi.org/10.1085/jgp.201110649.
72. Wanamaker, C.P., Christianson, J.C., and Green, W.N. (2003). Regulation of nicotinic acetylcholine receptor assembly. Ann. N. Y. Acad. Sci. *998*, 66–80. https://doi.org/10.1196/annals.1254.009.
73. Shiono, H., Roxanis, I., Zhang, W., Sims, G.P., Meager, A., Jacobson, L.W., Liu, J.L., Matthews, I., Wong, Y.L., Bonifati, M., et al. (2003). Scenarios for autoimmunization of T and B cells in myasthenia gravis. Ann. N. Y. Acad. Sci. *998*, 237–256. https://doi.org/10.1196/annals.1254.026.
74. Webster, R.G., Alabaf, S., Beerli, R., Gerwin, N., Dong, Y., and Beeson, D. (2022). Characterization of novel muscle acetylcholine receptor modifier, its action on channel kinetics and potential for treatment of fast channel congenital myasthenic syndrome. MUS MGFA. Muscle & Nerve *65*, S16.
75. Noridomi, K., Watanabe, G., Hansen, M.N., Han, G.W., and Chen, L. (2017). Structural insights into the molecular mechanisms of myasthenia gravis and their therapeutic implications. Elife *6*, e23043. https://doi.org/10.7554/eLife.23043.
76. Barger, C.J., Branick, C., Chee, L., and Karpf, A.R. (2019). Pan-Cancer Analyses Reveal Genomic Features of FOXM1 Overexpression in Cancer. Cancers (Basel) *11*, 251. https://doi.org/10.3390/cancers11020251.
77. Susac, L., Vuong, M.T., Thomas, C., von Bulow, S., O'Brien-Ball, C., Santos, A.M., Fernandes, R.A., Hummer, G., Tampe, R., and Davis, S.J. (2022). Structure of a fully assembled tumor-specific T cell receptor ligated by pMHC. Cell *185*, 3201–3213. https://doi.org/10.1016/j.cell.2022.07.010.
78. Cetin, H., Epstein, M., Liu, W.W., Maxwell, S., Rodriguez Cruz, P.M., Cossins, J., Vincent, A., Webster, R., Biggin, P.C., and Beeson, D. (2019). Muscle acetylcholine receptor conversion into chloride conductance at positive potentials by a single mutation. Proc. Natl. Acad. Sci. USA *116*, 21228–21235. https://doi.org/10.1073/pnas.1908284116.
79. Cormack, B.P., Valdivia, R.H., and Falkow, S. (1996). FACS-optimized mutants of the green fluorescent protein (GFP). Genewatch *173*, 33–38. https://doi.org/10.1016/0378-1119(95)00685-0.
80. Shaner, N.C., Campbell, R.E., Steinbach, P.A., Giepmans, B.N.G., Palmer, A.E., and Tsien, R.Y. (2004). Improved monomeric red, orange and yellow fluorescent proteins derived from Discosoma sp. red fluorescent protein. Nat. Biotechnol. *22*, 1567–1572. https://doi.org/10.1038/nbt1037.
81. Subach, O.M., Gundorov, I.S., Yoshimura, M., Subach, F.V., Zhang, J., Grüenwald, D., Souslova, E.A., Chudakov, D.M., and Verkhusha, V.V. (2008). Conversion of red fluorescent protein into a bright blue probe. Chem. Biol. *15*, 1116–1124. https://doi.org/10.1016/j.chembiol.2008.08.006.
82. Yu, D., Baird, M.A., Allen, J.R., Howe, E.S., Klassen, M.P., Reade, A., Makhijani, K., Song, Y., Liu, S., Murthy, Z., et al. (2015). A naturally monomeric infrared fluorescent protein for protein labeling in vivo. Nat. Methods *12*, 763–765. https://doi.org/10.1038/nmeth.3447.
83. Perkins, D.N., Pappin, D.J., Creasy, D.M., and Cottrell, J.S. (1999). Probability-based protein identification by searching sequence databases using mass spectrometry data. Electrophoresis *20*, 3551–3567. https://doi.org/10.1002/(SICI)1522-2683(19991201)20:18<3551::AID-ELPS3551>3.0.CO;2.
84. Punjani, A., Rubinstein, J.L., Fleet, D.J., and Brubaker, M.A. (2017). cryoSPARC: algorithms for rapid unsupervised cryo-EM structure determination. Nat. Methods *14*, 290–296. https://doi.org/10.1038/nmeth.4169.
85. Zheng, S.Q., Palovcak, E., Armache, J.P., Verba, K.A., Cheng, Y., and Agard, D.A. (2017). MotionCor2: anisotropic correction of beam-induced motion for improved cryo-electron microscopy. Nat. Methods *14*, 331–332. https://doi.org/10.1038/nmeth.4193.
86. Caesar, J., Reboul, C.F., Machello, C., Kiesewetter, S., Tang, M.L., Deme, J.C., Johnson, S., Elmlund, D., Lea, S.M., and Elmlund, H. (2020). SIMPLE 3.0. Stream single-particle cryo-EM analysis in real time. J. Struct. Biol. X *4*, 100040. https://doi.org/10.1016/j.yjsbx.2020.100040.
87. Asarnow, D., Palovcak, E., and Cheng, Y. (2019). asarnow/pyem: UCSF pyem v0.5 (v0.5). Zenodo. https://doi.org/10.5281/zenodo.3576630.
88. Jumper, J., Evans, R., Pritzel, A., Green, T., Figurnov, M., Ronneberger, O., Tunyasuvunakool, K., Bates, R., Žídek, A., Potapenko, A., et al. (2021). Highly accurate protein structure prediction with AlphaFold. Nature *596*, 583–589. https://doi.org/10.1038/s41586-021-03819-2.
89. Meng, E.C., Goddard, T.D., Pettersen, E.F., Couch, G.S., Pearson, Z.J., Morris, J.H., and Ferrin, T.E. (2023). UCSF ChimeraX: Tools for structure building and analysis. Protein Sci. *32*, e4792. https://doi.org/10.1002/pro.4792.
90. Punjani, A., Zhang, H., and Fleet, D.J. (2020). Non-uniform refinement: adaptive regularization improves single-particle cryo-EM reconstruction. Nat. Methods *17*, 1214–1221. https://doi.org/10.1038/s41592-020-00990-8.
91. Camacho, C., Boratyn, G.M., Joukov, V., Vera Alvarez, R., and Madden, T.L. (2023). ElasticBLAST: accelerating sequence search via cloud computing. BMC Bioinf. *24*, 117. https://doi.org/10.1186/s12859-023-05245-9.
92. Emsley, P., Lohkamp, B., Scott, W.G., and Cowtan, K. (2010). Features and development of Coot. Acta. Crystallogr. D. Biol. Crystallogr. *66*, 486–501. https://doi.org/10.1107/S0907444910007493.
93. Croll, T.I. (2018). ISOLDE: a physically realistic environment for model building into low-resolution electron-density maps. Acta Crystallogr. D Struct. Biol. *74*, 519–530. https://doi.org/10.1107/S2059798318002425.
94. Liebschner, D., Afonine, P.V., Baker, M.L., Bunkóczi, G., Chen, V.B., Croll, T.I., Hintze, B., Hung, L.W., Jain, S., McCoy, A.J., et al. (2019). Macromolecular structure determination using X-rays, neutrons and electrons: recent developments in Phenix. Acta Crystallogr. D Struct. Biol. *75*, 861–877. https://doi.org/10.1107/S2059798319011471.
95. Smart, O.S., Sharff, A., Holstein, J., Womack, T.O., Flensburg, C., Keller, P., Paciorek, W., Vonrhein, C., and Bricogne, G. (2021). Grade2 version 1.6.0. https://gphl.gitlab.io/grade2_docs/index.html
96. Bruno, I.J., Cole, J.C., Kessler, M., Luo, J., Motherwell, W.D.S., Purkis, L.H., Smith, B.R., Taylor, R., Cooper, R.I., Harris, S.E., and Orpen, A.G. (2004). Retrieval of crystallographically-derived molecular geometry information. J. Chem. Inf. Comput. Sci. *44*, 2133–2144. https://doi.org/10.1021/ci049780b.
97. Dialpuri, J.S., Bagdonas, H., Atanasova, M., Schofield, L.C., Hekkelman, M.L., Joosten, R.P., and Agirre, J. (2023). Analysis and validation of

overall N-glycan conformation in Privateer. Acta Crystallogr. D Struct. Biol. *79*, 462–472. https://doi.org/10.1107/S2059798323003510.

98. Smart, O.S., Neduvelil, J.G., Wang, X., Wallace, B.A., and Sansom, M.S. (1996). HOLE: a program for the analysis of the pore dimensions of ion channel structural models. J. Mol. Graph. *14*, 354–376. https://doi.org/10.1016/s0263-7855(97)00009-x.
99. Yamashita, K., Palmer, C.M., Burnley, T., and Murshudov, G.N. (2021). Cryo-EM single-particle structure refinement and map calculation using Servalcat. Acta Crystallogr. D Struct. Biol. *77*, 1282–1291. https://doi.org/10.1107/S2059798321009475.
100. Bhushan, A., and McNamee, M.G. (1990). Differential scanning calorimetry and Fourier transform infrared analysis of lipid-protein interactions involving the nicotinic acetylcholine receptor. Biochim. Biophys. Acta *1027*, 93–101. https://doi.org/10.1016/0005-2736(90)90053-q.
101. Stevens, R. (2008). Large Scale Preparation of Membrane Containing Over-expressed Proteins from SF9 Cells. https://commonfund.nih.gov/sites/default/files/JCIMPT_MembranePrep.pdf.
102. Agirre, J., Iglesias-Fernández, J., Rovira, C., Davies, G.J., Wilson, K.S., and Cowtan, K.D. (2015). Privateer: software for the conformational validation of carbohydrate structures. Nat. Struct. Mol. Biol. *22*, 833–834. https://doi.org/10.1038/nsmb.3115.
103. Hamill, O.P., Marty, A., Neher, E., Sakmann, B., and Sigworth, F.J. (1981). Improved patch-clamp techniques for high-resolution current recording from cells and cell-free membrane patches. Pflügers Archiv *391*, 85–100. https://doi.org/10.1007/BF00656997.
104. Clapham, D.E., and Neher, E. (1984). Substance P reduces acetylcholine-induced currents in isolated bovine chromaffin cells. J. Physiol. *347*, 255–277. https://doi.org/10.1113/jphysiol.1984.sp015065.

STAR★METHODS

KEY RESOURCES TABLE

REAGENT or RESOURCE	SOURCE	IDENTIFIER
Antibodies		
ε subunit-specific polyclonal rabbit antiserum	Shiono et al.Cou[73]	N/A
Goat anti-rabbit IgG	Phoenix Pharmaceuticals	RK-GAR
Chemicals, peptides, and recombinant proteins		
Freestyle 293 medium	Gibco	Cat# 12338018
Penicillin-Streptomycin-Amphotericin B mix	Lonza	Cat# 17-745E
Hexamidine bromide	Merck	Cat# H9268
Puromycin	Merck	Cat# P8833
Doxycycline	Merck	Cat# D3072
Fetal bovine serum	PAA Laboratories	N/A
Fetal bovine serum	Gibco	Cat# 10062-147
Trypsin-EDTA	Gibco	Cat# 15400054
Dulbecco modified Eagle Medium (DMEM)	Gibco	Cat# 11965092
Penicillin-streptomycin	Gibco	Cat# 15140122
Immobilized papain (agarose resin)	Thermo Scientific	Cat# 20341
Sodium butyrate	Merck	Cat# 8451440100
EDTA-free protease inhibitor cocktail	Roche	Cat# 04693132001
n-Dodecyl-β-D-Maltopyranoside (DDM)	Anatrace	Cat# D310LA
Cholesteryl hemisuccinate (CHS)	Merck	Cat# C6512
Bromoacetylcholine bromide	Santa-Cruz	Cat# sc-252517
Affi-Gel 10 media	Bio-Rad	Cat# 1536099
Carbachol (carbamylcholine)	Alfa Aesar	Cat# L06674.14
α-bungarotoxin	Invitrogen	Cat# B1601
Soy polar lipids	Avanti	Cat# 541602
(1-palmitoyl-2-oleoyl-*glycero*-3-phosphocholine) POPC	Avanti	Cat# 850457
MSP2N2	Merck	Cat# MSP12
Bio-Beads SM-2 resin	Bio-Rad	Cat# 1523920
Acetylcholine chloride	Alfa Aesar	Cat# L02168.14
Fluoxetine hydrochloride	Fluorochem	Cat# F375072
DC-98-LC-74 ('PAM')	Webster et al.[74]	N/A
Polyethylenimine (PEI)	Sigma-Aldrich	Cat# 408727
^{125}I-α-bungarotoxin	Revvity	Cat# NEX126050UC
Phosphate buffered saline (PBS)	Oxoid	Cat# BR0014G
Bovine serum albumin	Sigma-Aldrich	Cat# A9418
Triton X-100	Sigma-Aldrich	Cat# X100
Critical commercial assays		
R80 Congenital myasthenic syndrome gene panel	NHS genomics medicine service	https://panelapp.genomicsengland.co.uk/panels/232/
Superose 6 Increase 10/300 GL	Cytiva	Cat# 29091596
Deposited data		
Coordinates of resting AChR in detergent with alpha-bungarotoxin	This paper	9GU0
Cryo-EM map of resting AChR in detergent with alpha-bungarotoxin	This paper	EMD-51568

(*Continued on next page*)

Continued

REAGENT or RESOURCE	SOURCE	IDENTIFIER
Coordinates of resting AChR in nanodisc with alpha-bungarotoxin	This paper	9GU1
Cryo-EM map of resting AChR in nanodisc with alpha-bungarotoxin	This paper	EMD-51569
Coordinates of desensitised AChR in nanodisc with 100 μM acetylcholine	This paper	9GU2
Cryo-EM map of desensitised AChR in nanodisc with 100 μM acetylcholine	This paper	EMD-51570
Coordinates of desensitised AChR in nanodisc with 1 mM acetylcholine	This paper	9GU3
Cryo-EM map of desensitised AChR in nanodisc with 1 mM acetylcholine	This paper	EMD-51571
Coordinates of Fab35 in-complex with human nAChR alpha1	Noridomi et al.[75]	5HBT
Coordinates of bovine adult muscle nAChR resting state	Li et al.[28]	9AVV
Coordinates of bovine adult muscle nAChR bound to ACh	Li et al.[28]	9AWJ
Coordinates of *Torpedo* acetylcholine receptor in complex with alpha-bungarotoxin	Rahman et al.[24]	6UWZ
Coordinates of c-Src-SH3 domain	Camara-Artigas[64]	4RTZ
Experimental models: Cell lines		
HEK293	ATCC	Cat# CRL-1573
Expi293F	Gibco	Cat# A14527
mAb35	ATCC	Cat# TIB-175
Recombinant DNA		
TLCV2	Barger et al.[76]	Addgene 87360
pCMV delta8.91 (p8.91)	Susac et al.[77]	Addgene 187441
psPAX2	psPAX2 was a gift from Didier Trono	Addgene 12260
pMDG	Susac et al.[77]	Addgene 187440
pMD2.G	pMD2.G was a gift from Didier Trono	Addgene 12259
pcDNA3.1-hygro-CHRNA1 (P3A negative isoform)	Cetin et al.[78]	N/A
pcDNA3.1-hygro-CHRNB1	Cetin et al.[78]	N/A
pcDNA3.1-hygro-CHRND	Cetin et al.[78]	N/A
pcDNA3.1-hygro-CHRNE-EGFP	Ealing et al.[36]	N/A
EGFP	Cormack et al.[79]	N/A
mCherry	Shaner et al.[80]	N/A
TagBFP	Subach et al.[81]	N/A
mIFP	Yu et al.[82]	N/A
pEGFP-N1	Clontech	N/A
Software and algorithms		
MASCOT	Matrix Science[83]	https://www.matrixscience.com/
EPU	Thermo Scientific	https://www.thermofisher.com/uk/en/home/electron-microscopy/products/software-em-3d-vis/epu-software.html
cryoSPARC	Punjani et al.[84]	https://cryosparc.com/
RELION	Zivanov et al.[58]	https://www3.mrc-lmb.cam.ac.uk/relion/index.php/Main_Page

(*Continued on next page*)

Continued

REAGENT or RESOURCE	SOURCE	IDENTIFIER
MotionCor2	Zheng et al.[85]	https://emcore.ucsf.edu/ucsf-software
SIMPLE 3.0	Caesar et al.[86]	N/A
UCSF pyem v0.5	Asarnow et al.[87]	https://zenodo.org/records/3576630
Alfafold2	Jumper et al.[88]	https://alphafold.ebi.ac.uk/
UCSF ChimeraX	Meng et al.[89]	https://www.cgl.ucsf.edu/chimerax/
Non-uniform refinement (cryoSPARC)	Punjani et al.[90]	https://guide.cryosparc.com/processing-data/all-job-types-in-cryosparc/3d-refinement/job-non-uniform-refinement-new
ModelAngelo	Jamali et al.[57]	https://github.com/3dem/model-angelo
Blast	Camacho et al.[91]	https://blast.ncbi.nlm.nih.gov/Blast.cgi
Coot	Emsley et al.[92]	https://www2.mrc-lmb.cam.ac.uk/personal/pemsley/coot/
ISOLDE	Croll[93]	https://tristanic.github.io/isolde/
PHENIX 1.21	Liebschner et al.[94]	https://phenix-online.org/
GRADE2	Smart et al.[95]	https://gphl.gitlab.io/grade2_docs/index.html
MOGUL	Bruno et al.[96]	https://www.ccdc.cam.ac.uk/solutions/software/mogul/
Privateer	Dialpuri et al.[97]	https://privateer.york.ac.uk/
HOLE	Smart et al.[98]	https://www.holeprogram.org/
ICM Browser Pro	Molsoft L.L.C	https://www.molsoft.com/icm_browser_pro.html
Refmac Servalcat	Yamashita et al.[99]	https://servalcat.readthedocs.io/en/latest/overview.html
PyMOL	Schrödinger, LLC	https://pymol.org/
pCLAMP10	Molecular Devices	https://www.moleculardevices.com/products/axon-patch-clamp-system/acquisition-and-analysis-software/pclamp-software-suite
Prism 10	GraphPad	https://www.graphpad.com/
Inkscape	Inkscape Project	https://inkscape.org/cs/
Other		
UltrAuFoil R1.2/1.3 300 mesh gold grid	Quantifoil	Cat# N1-A21nAu30-50
Quantifoil R1.2/1.3 200 mesh copper grid	Quantifoil	Cat# N1-C14nCu20-01
Quantifoil R1.2/1.3 300 mesh copper grid	Quantifoil	Cat# N1-C14nCu30-01

EXPERIMENTAL MODEL AND STUDY PARTICIPANT DETAILS

Cells

Expi293F cells (Gibco) were bought from Thermo Fischer Scientific just prior to the initiation of this study, with authentication data from the company. They were maintained in Freestyle 293 medium (Gibco) supplemented with 0.1% v/v penicillin-streptomycin-amphotericin B mix (PSA, Lonza), and cultured at 37°C, 100–250 rpm, 75% humidity and 8% CO_2. HEK293 cells were maintained in Dulbecco modified Eagle Medium (Gibco) supplemented with 1% PSA (Lonza) and 10% fetal bovine serum (PAA Laboratories or Gibco) and cultured at 37°C and 5% CO_2 for electrophysiology and radioactive binding assays. The newly generated AChR-expressing cell lines were grown in the same condition as the parental Expi293F cells, we did not authenticate the cells nor tested for mycoplasma contamination during the course of this study.

METHOD DETAILS

Cell line generation and selection

Lentivirus was generated by first transfecting HEK293 cells with the AChR gene-containing TLCV2 plasmids, along with 2nd or 3rd generation lentiviral packaging and envelope plasmids (pCMV delta8.91/psPAX2 and pMDG/pMD2.G). Cell culture medium consisted of Freestyle 293 medium (Gibco) with 0.1% v/v penicillin-streptomycin-amphotericin B mix (PSA, Lonza). Lentivirus particles were harvested from the supernatant on day 4. To generate cell lines stably expressing AChR, on day 1 of cell line generation, 3 mL of

Expi293F cells at 0.3x10^6 cells/mL with 5 mg/mL hexamidine bromide (Merck) were seeded in a 24-well block (VWR). Lentivirus for each AChR subunit were then each added to the cells at a final concentration of 0.15x10^6-0.3x10^6 transducing units (TU) per mL to achieve an approximate multiplicity of infection (MOI) of 1. The block was covered with porous adhesive film (VWR) and grown in a shaking incubator (Infors HT Multitron) for 2 days at 37°C, 250 rpm, 75% humidity and 8% CO_2, before exchanging to fresh medium on day 3. On day 4, induced cells were selected by adding 2.5 mg/mL puromycin. The medium was replaced every 2–5 days with an increasing amount of puromycin, until it reached 10 mg/mL. Selection was considered complete when the negative control of untransfected Expi293F cells undergoing the same puromycin selection were all dead (day 15).

Cells were then selected for AChR expression by first inducing expression with 0.1 μg/mL doxycycline (Merck) and then maintaining the cells at 0.3-3x10^6/mL until GFP fluorescence appeared (day 17). The cells were then separated by FACS, using cell sorters (BD Aria FUSION or Sony MA900 FACS) fitted with a 100 mm nozzle and fluorescent filters (405–450/50, 561–610/20, 640–710/50 and 488–525/50) to select for quadruple positive cells (tagBFP$^+$mIFP$^+$mCherry$^+$EGFP$^+$) expressing all AChR subunits. Single cells were seeded into 100 μL medium with 10% v/v fetal bovine serum (FBS, PAA Laboratories or Gibco) in 96-well round bottom plates (Corning). Cells collected from FACS were cultured at 37°C, 75% humidity and 8% CO_2 in a static incubator, replacing half of the supernatant with fresh medium every 1–3 days until colonies contained hundreds of cells before being dissociated with trypsin-EDTA (Gibco) and transferred to 48-well plates (Corning). Once confluent, the cells were transferred to 24-well plates (Corning), followed by suspension-adaptation by growing in 24-well blocks and incubating with shaking at 250 rpm, passaging every 1-3 days to maintain a density of 0.3-3x10^6 cells/mL. A final selection for AChR surface –expression was performed by radioactive ^{125}I-αBuTx-binding assay, selecting the cell line with the highest receptor surface expression for large-scale protein production.

Generation of Fab35

Mab35 is an IgG1 antibody against the AChR-α subunit produced by a rat immunised with *Electrophorus* AChR.[38] Mab35-expressing hybridoma cells (ATCC) were cultured in growth medium consisting of Dulbecco modified Eagle Medium (DMEM, Gibco) with 10% v/v FBS and 1% v/v penicillin-streptomycin (Gibco) at 37°C and 8% CO_2. Cells were sub-cultured every 2 to 3 days to maintain a density of 0.1-1x10^6 cells/mL and expanded from a T25 flask (Corning) to a T175 flask (Corning). When cell reached complete confluency, the flask was filled with ~450 mL growth medium and incubated until the medium turned orange at 2–3 weeks, with the semi-adherent cells resuspended every 3–5 days. The mAb35 was harvested from the cell culture supernatant, purified, and cleaved with papain (Thermo Scientific) to produce Fab35.[75]

AChR expression, purification and nanodisc reconstitution

The AChR-expressing cell line was grown in Freestyle 293 medium (Invitrogen) with 0.1% v/v penicillin-streptomycin-amphotericin B mix in disposable roller bottles (Greiner Bio-One or Corning) or Erlenmeyer flasks (Jet Biofil or Corning) in a shaking incubator at 37°C, 100–170 rpm, 75% humidity and 8% CO_2. Cells were maintained at 0.3-3x10^6 cells/mL. Protein was expressed by first seeding one liter of cells (1x10^6/mL) into each roller bottle, and then inducing expression the following day by adding 0.1 μg/mL doxycycline and 5 mM sterile-filtered sodium butyrate (Merck). Cells were then grown at 30°C, 170 rpm for 3 days, and harvested by centrifugation at 1,500 g for 20 min at 4°C. Cell pellets were flash frozen in liquid nitrogen and stored at −80°C until use.[100]

Membrane preparation was based on a protocol by Stevens et al.[101] Briefly, cell pellets from a 10 L of cell culture were thawed on ice, resuspended in 200 mL low salt buffer (50 mM HEPES-NaOH pH 7.5, 10 mM NaCl, 5% v/v glycerol, 5 mM $MgCl_2$ and EDTA-free protease inhibitors (Roche)) using a Dounce homogeniser (Merck), then lysed by 2 passes through a C3 or C5 Emulsiflex homogeniser (Avestin) at 10,000–15,000 psi. Lysate was brought to 400 mL with low salt buffer, then ultracentrifuged at 150,000 g for 45 min in a Ti45 rotor (Beckman Coulter). The membrane pellet was then washed by resuspending in low salt buffer with a Dounce homogeniser, then the volume adjusted to 400 mL and pelleting by ultracentrifugation again. Two additional washes were performed in high salt buffer (50 mM HEPES-NaOH pH 7.5, 1 M NaCl, 5% v/v glycerol, 5 mM $MgCl_2$ and EDTA-free protease inhibitors) before the pellet was resuspended in 50 mL extraction buffer (50 mM HEPES-NaOH pH 7.5, 250 mM NaCl, 5% v/v glycerol), flash frozen in liquid nitrogen, and stored at −80°C until use.

To purify AChR, prepared membrane was thawed and resuspended in extraction buffer using a Dounce homogeniser. All steps of protein purification and cryo-EM sample preparation were performed at 4°C or on ice. A concentrated detergent stock was made by dissolving 10% w/v DDM (Anatrace) and 1% w/v CHS (Merck) in water, referred to as 10% DDM/CHS. Protease inhibitor (Roche) and a final concentration of 1% DDM/CHS were added to 400 mL resuspended membrane, and the sample was stirred for 1 h. Solubilised lysate was clarified by ultracentrifugation for 1 h at 100,000 g, then the supernatant was nutated with 5 mL pre-equilibrated bromoacetylcholine (BAC) affinity resins for 2 h. Bromoacetylcholine affinity resin was generated by coupling bromoacetylcholine bromide (Santa-Cruz) to Affi-Gel 10 (BioRad) according to Bhushan and McNamee.[100] Briefly, a 25 mL bottle of Affi-Gel 10 media was reacted with 0.054 M cystamine hydrochloride in 20 mM MOPS at pH 7.4 for 1 h. The resin was washed with water and reacted with 0.1 M dithiothreitol in 0.1 M MOPS at pH 8 for >30 min. The gel was washed with water and mixed with 500 mg bromoacetylcholine bromide in 0.1 M MOPS pH 7.4 for >1hr. The resin was washed with water, reacted with 50 mg iodoacetamide for <30 min, followed by washes with 0.1 M sodium acetate pH 4 and water and stored at 4°C until use. Flow-through was removed by centrifugation at 600*g* for 5–7 min, with the resin transferred to a gravity column and washed with 5 mL extraction buffer (with 0.026% DDM/CHS). Protein was eluted with elution buffer (50 mM HEPES-NaOH pH 7.5, 250 mM NaCl, 5% v/v glycerol, 100 mM carbamylcholine, 0.026% DDM/CHS).

For detergent-solubilised AChR samples, EGFP-positive fractions detected by a ChemiDoc (BioRad) were pooled and incubated overnight with Fab35 and α-bungarotoxin (Invitrogen) 1:3:3 molar ratio. Next day, the sample was concentrated to 500 μL with 100 kDa concentrator (Sartorious), and then purified by Size-Exclusion Chromatography (SEC) using an ÄKTA Pure FPLC system (Cytiva) with a Superose 6 Increase 10/300 GL column (Cytiva) in gel filtration buffer (20 mM HEPES-NaOH pH 7.5, 150 mM NaCl, 0.013% w/v DDM/CHS). EGFP-positive fractions were concentrated to 1–2 mg/mL and used immediately for making cryo-EM grids.

For nanodisc reconstitution of the αBuTx-bound sample, EGFP-positive elution fractions were exchanged into extraction buffer with PD-10 columns (Cytiva) to remove detergent, then concentrated to 1 mL. POPC (Avanti) was dissolved in 20% DDM to create a 50 mM stock solution. A reconstitution mixture comprising protein to MSP2N2 to lipid molar ratio of 1:3:120 was nutated overnight. Next day, Bio-Beads (BioRad) were added at the rate of 4 mg/h which was gradually increased to 20 mg/h, with the used Biobeads removed after every 3-5 additions, until the total mass of Biobeads exceeded 6 times the mass of detergent in the sample. During the final incubation with Biobeads, Fab35 and αBuTx were added to the protein at an estimated molar ratio of 3:3:1 and the mixture was rotated overnight. Next day, the supernatant was concentrated to 500 μL and separated by SEC in gel filtration buffer without detergent (20 mM HEPES-NaOH pH 7.5, 150 mM NaCl). GFP-positive fractions were pooled and concentrated to 1–2 mg/mL, spun at 17,000 g for >30 min to remove aggregates, and the supernatant was collected to make cryo-EM grids.

Preparation of the desensitised sample followed the same protocol as the nanodisc-reconstituted sample with αBuTx, except soy polar lipids (Avanti) was used instead of POPC, and the reconstitution ratio of protein to MSP2N2 to lipids was 1:6:240. In addition, αBuTx was replaced by 1 mM ACh or 100 μM ACh, 200 μM fluoxetine and 250 μM PAM,[74] which were incubated for >1 h with the protein before sample vitrification.

In-gel digest mass spectrometry

The presence of AChR subunits in Coomassie-stained SDS-PAGE of purified samples was confirmed by tryptic digestion and tandem mass spectrometry (LC-MS/MS) at the Center for Medicines Discovery (CMD) Mass Spec Facility. Coomassie-stained SDS-PAGE gel bands were excised using a gel cutting tip (GeneCatcher, Web Scientific) and stored in 10% MeOH at 4°C. Prior to digestion, the methanol solution was removed and replaced with 100% acetonitrile for 2–5 min. The solution was then removed and replaced with 100 μL of 100 mM NH_4HCO_3 (pH 8.0). A further 1 μL of 1 M dithiothreitol was added and incubated at 56°C for 40 min, followed by the addition of 4 μL of 1 M iodoacetamide and the reaction incubated at ambient temperature in the dark for 20 min. Then, 1 μL of 1 M dithiothrietol, 200 μL of 100 mM NH_4HCO_3 and 1 μL of trypsin solution (sequencing grade, Sigma-Aldrich, 1 mg/mL in 0.01 M HCl) was added. Tryptic digestion proceeded at 37°C for 16 h and was terminated by the addition of 3 μL formic acid. Extracted peptides were analyzed by TimsTOF 2 pro mass spectrometer (Bruker) with a nanoElute liquid chromatography system (Brucker), proteomics analysis was performed in MASCOT (Matrix Science).[83]

Cryo-EM sample preparation

The detergent-solubilised αBuTx-bound dataset was prepared on a UltrAuFoil R1.2/1.3 300 mesh gold grid, and the remaining three nanodisc-reconstituted datasets were prepared on Quantifoil R1.2/1.3 200 or 300 mesh copper grids. EM grids were glow-discharged for 60 s in air. Samples were vitrified using a Vitrobot Mark IV (FEI/Thermo Scientific) at 4°C and 100% humidity by applying to the grid 2.5–3 μL freshly prepared protein sample at 2–4 mg/mL, blotting for 2–4.5 s with a blot force of −10, and then immediate plunge freezing in liquid ethane.

Cryo-EM data collection

Data collection parameters are summarised in Table S2.

For the αBuTx-bound detergent-solubilised dataset, a total of 18,672 movies were recorded on a Titan Krios microscope at Oxford Particle Imaging Center (OPIC, Oxford) using EPU control software (Thermo Scientific) and a Falcon 4i direct electron detector with a target defocus range of −1.2 to −2.4μm, a dose rate of 9.81 e^-/pixel/s, and a total dose of 50 $e^-/Å^2$. Data were collected at a nominal magnification of 130,000×, corresponding to a calibrated pixel size of 0.932Å.

For the αBuTx-bound nanodisc dataset, a total of 30,556 movies were collected on a Titan Krios microscope at Central Oxford Structural Molecular Imaging Center (COSMIC, Oxford) using EPU control software (Thermo Scientific) and a Gatan K3 detector with an energy filter slit width set to 20 eV. Data were recorded at a magnification of 105,000×, corresponding to a calibrated pixel size of 0.832 Å, using a target defocus range of −0.8 to −2.2 μm, a dose rate of 11.32 e^-/pixel/s and a total dose of 46 $e^-/Å^2$. Movies were dose fractionated into 45 frames.

For the ACh-bound (100 μM) nanodisc dataset, 13,868 movies were recorded on Titan Krios with a Falcon 4i camera at Electron Bio-Imaging Center (KriosIII, Diamond-eBIC, Harwell) using EPU control software (Thermo Scientific) at a nominal magnification of 130,000× for a calibrated pixel size of 0.921 Å. The grid was imaged using a target defocus range of −0.8 to −2.4 μm, a dose rate of 6.64 e^-/pixel/s, and total dose 50 $e^-/Å^2$. The Selectris X energy filter slit width was set at 10 eV.

For the ACh-bound (1 mM) 'desensitised' nanodisc dataset, a total of 19,925 movies were collected on a Titan Krios microscope at Central Oxford Structural Molecular Imaging Center (COSMIC, Oxford) using EPU control software (Thermo Scientific) with a Gatan K3 detector using a nominal magnification of 130,000× for acalibrated pixel size 0.65 Å. The energy filter slit width was set to 20 eV, the target defocus range was −1.0 to −2.2 μm, with a dose rate of 13.90 e^-/pixel/s, and a total dose of 52.2 $e^-/Å^2$. Movies were dose fractionated into 50 frames.

Cryo-EM image processing

Data processing workflows are summarised in Figures S2–S8. Data were processed with cryoSPARC (v3.3.1/4.4.1)[84] and RELION (v3.1/v5.0).[58] Electron Event Representation (EER) movies were fractionated into frames with a dose of 1 $e^{-}/Å^{2}$ for the detergent solubilised image set and 0.476 $e^{-}/Å^{2}$ for the 100 μM ACh image set, which were collected on a Falcon 4i detector, prior to motion-correction. Motion correction was carried out using cryoSPARC's patch motion correction for the detergent-solubilised sample, SIMPLE for the αBuTx-bound AChR in nanodisc, and RELION for the two remaining ACh-bound datasets; this was followed by patch CTF-correction, particle-picking and 2D classification in cryoSPARC.[58,84–86] Particles from well resolved 2D classes were used for *ab initio* model generation followed by rounds of heterogeneous refinement to isolate particles with either one or two bound Fab35 molecules. Initial processing of all datasets highlighted the presence of several non-$\alpha_2\beta\delta\varepsilon$ stoichiometries so further downstream processing focused on the 2Fab class. After non-uniform refinement, aligned particles were exported from cryoSPARC to RELION using *csparc2star.py* from the PYEM package.[87] Particles from the nanodisc-reconstituted datasets underwent per particle CTF refinement and Bayesian polishing in RELION. All particle sets also underwent static 3D classification in RELION using focused masks generated from Alphafold2[88] initial models using UCSF ChimeraX[89] (Table S2 and Figures S2–S8). Less rounds of static 3D classification were performed on the nanodisc image sets due to their overall preferential particle orientational bias. After static 3D classification, final particle sets were reimported into cryoSPARC for a final round of non-uniform refinement to yield the final reconstructions.[90] Subunit stoichiometries were checked at each stage of data processing using unsupervised automated model building with ModelAngelo,[57] with the longest traced sequence of each subunit identified using the 'Blast Protein' tool within UCSF ChimeraX.[88,91]

Model building and refinement

Coordinates for αBuTx and Fab35 were derived from PDB entry 5HBT.[75] Coordinates for AChR subunits were derived from the AlphaFold2 model database, which was used to generate the initial models.[88] Initial models were fitted into the maps using UCSF ChimeraX[89] and then adjusted and real-space refined in COOT.[92] In addition, models built using ModelAngelo[57] were used to guide manual model building in COOT. Residue numbering for AChR subunits start after the signal peptide sequences, in accordance with the established AChR nomenclature where αL251 is situated at the 9′ midpoint position of the pore.[23] Rebuilt models were then refined against appropriately *B*-factor sharpened maps in ISOLDE[93] before final global real-space refinement in PHENIX 1.21[94] using appropriate reference model and geometric restraints. The αBuTx peptides were modeled into the low occupancy density of the detergent-solubilised sample by docking αBuTx from 5HBT into a blurred map, and their location confirmed in the better resolved αBuTx density of the nanodisc dataset. For the ACh-bound structures, an initial model was built using the map from 100 μM ACh data as this was visually superior to the 1 mM ACh map. ACh was well-defined in the Coulomb potential map and could be placed unambiguously. Ligand restraints were generated using GRADE2[95] and the modeled ACh conformation was validated with MOGUL.[96] In all structures, a disulphide bond was apparent and modeled between αC192 and αC193 in loop C although there was some evidence of partial S-S reduction particularly in the resting nanodisc structure. In general, the M1-M4 transmembrane helices were worse resolved in all the nanodisc datasets (Figure S6) and it was not possible to unambiguously assign the position of all sidechains in the TMD, thus, the ambiguous sidechains were built to polyalanine. N-glycan structures were validated with Privateer assuming hybrid chains and human expression system.[97,102] Pore profiles were generated from structures using the HOLE[98] implementation in COOT[92] after reinstating any truncated side chains using ICM Browser Pro (Molsoft L.L.C).

To highlight significant non-protein density, mask-normalised F_o-F_c difference maps were generated by refining the final model with all non-protein atoms removed using Refmac Servalcat[99] within the CCPEM-1.6.0 suite and the refinement mask from cryoSPARC's non-uniform refinement to normalise the sigma levels. Prior to difference map calculation, models were refined for 30 cycles against sharpened half maps using jelly-body restraints.

Sequence-independent structural superpositions of the relevant AChR chains were carried out in PyMOL (The PyMOL Molecular Graphics System, Version 3.0 Schrödinger, LLC) using the 'super' command, and the output RMSD values are for all equivalent atoms after structural outlier rejection.

CMS patient variants

Suspected cases of congenital myasthenic syndrome are referred to the 'Oxford highly specialised clinical service for CMS' for genetic analysis and/or AChR functional assessment to determine pathogenicity. Variants in the AChR subunit genes were identified by next-generation whole genome/exome sequencing by NHS Genomics Medicine Service using the R80 Congenital myasthenic syndrome gene panel (see Key Resources Table), and confirmed in the patient DNA by Sanger sequencing. Confirmed variants were introduced into respective AChR subunit cDNAs by site-directed mutagenesis. Following mutagenesis, constructs were revalidated by Sanger sequencing and then used in functional or electrophysiological studies (see construct design, electrophysiology and radioactive ^{125}I-αBuTx-binding assay for measuring AChR surface expression).

Construct design

Complementary DNAs (cDNA) encoding human wildtype AChR α1- (P3A negative isoform), β1-, and δ-subunits were cloned into pcDNA3.1-hygro.[78] The ε_{EGFP} construct was generated by inserting EGFP from pEGFP-N1 (BD Biosciences) into the M3-M4 loop of wildtype ε sequence using the *Sfi*I restriction site.[36] The doxycycline-inducible lentiviral TLCV2 vector (AddGene) was first modified by a) removing the Cas9 sequence from the original vector, b) inserting a KOZAK sequence, and b) inserting an internal ribosome

entry site (IRES2) followed by fluorescent protein cDNA of tagBFP, mCherry, mIFP, or EGFP,[79–82] before the AChR cDNA was cloned into the vector between the KOZAK and IRES2 to create the co-expression constructs: α-tagBFP, β-mIFP, and δ-mCherry. The construct for the ε_{EGFP} fusion protein contained no fluorescent protein following IRES2. Final constructs were verified by Sanger sequencing.

Electrophysiology

Recordings were made from HEK293 cells 48 h after polyethylenimine (PEI, Sigma-Aldrich) transfection with AChR subunit cDNAs in pcDNA3.1 vector, with pEGFP-N1 (Clonetech) included as a marker of transfection. Recordings were performed in the cell-attached patch configuration at 20°C–22°C.[103] The cells were bathed in a solution containing 150 mM NaCl, 2.8 mM KCl, 2 mM $MgCl_2$, 1 mM $CaCl_2$, 10 mM HEPES-NaOH, 10 mM glucose, at pH 7.4. The pipette solution was the same as bath solution, except glucose was omitted and ACh added to 100 nM or 500 nM (for δD180N variant only). Single-channel currents were amplified with an Axopatch 200B amplifier (Molecular Devices, Sunnyvale, California), and sampled at 100 kHz, initially filtered at 5 kHz (−3 dB, Bessel filter), with a resolution of 50 μs. Burst duration recordings were made with the pipette potential set at +80 mV. For the determination of channel conductance, pipette holding potentials was varied from +20 mV to +120 mV. Channel transitions were detected by 50% amplitude threshold crossings (pClamp10). Bursts were defined as groups of openings separated by closed intervals longer than a critical duration (t_{crit}). t_{crit} was determined for each patch using Equation 1,[104]:

$$a_1 \times e^{-t_{crit}/\tau_1} = a_2 \times \left(1 - e^{\frac{-t_{crit}}{\tau_2}}\right) \quad \text{(Equation 1)}$$

where a and τ indicate area and time constant for within and between bursts. Histograms of burst duration were fitted to the sum of exponentials by maximum log likelihood. Wildtype $\alpha_2\beta\delta\varepsilon$ channels and most mutants were typically best fit by the sum of 3 exponential functions, though αI49T that was best fit by 4 exponentials. In some cases, insufficient channel activity was recorded from individual patches; in those cases, recorded burst from multiple patches were combined and then fit by the sum of exponentials. In these cases, the fitting error is reported. The τ values of the population with longest duration are reported and compared with WT values.

Radioactive ^{125}I-αBuTx-binding assay for measuring AChR surface expression

HEK293 cells were grown in DMEM (Gibco) supplemented with 10% FCS and 1% PSA at 37°C and 5% CO_2. Cells were seeded at $3x10^5$ cells per well of a 6-well plate and PEI-transfected the following day with 3 μg DNA per well with a ratio of 2:1:1:1 of human muscle AChR α1, β1, δ, and ε subunits. Forty-eight hours post-transfection, ^{125}I-αBuTx (Revvity/PerkinElmer) was added to the cells at 1×10^6 counts per minute (cpm) per well in 1 mL phosphate buffered saline (PBS, Oxoid) with 1 mg/mL bovine serum albumin (Sigma-Aldrich) and incubated at room temp for 1 h. Each well of adherent cells was washed three times for 5 min with PBS, removed from the plate using 0.5 mL lysis buffer (10 mM Tris-HCl, 100 mM NaCl, 1 mM EDTA, 1% Triton X-100, pH 7.5), and levels of gamma radiation (in cpm) were recorded by a Cobra-II Auto Gamma Counter (Packard).

To analyze the εS235A CMS variant, an extra immunoprecipitation step was performed on the transfected cells to eliminate the contaminating effects of αβδ receptors. Cells were labeled with ^{125}I-αBuTx, washed in PBS, and removed from plates in lysis buffer as described before. This ensures only receptors on the cell surface were labeled. For immunoprecipitation, the lysate was incubated with 5 μL of the ε subunit-specific polyclonal rabbit antiserum[73] overnight at 4°C. Following day, 75 μL of goat anti-rabbit IgG (Phoenix Pharmaceuticals) was added for 2 h at room temperature with rotation. Precipitate was spun down at 15,000–20,000 g for 5 min and analyzed for the residual gamma radiation.

QUANTIFICATION AND STATISTICAL ANALYSIS

Quantitative data is analyzed in Prism 10 software (GraphPad) and presented as mean ± standard error of the mean (SEM). Figures were prepared in Inkscape (Inkscape Project).

Cell Reports, Volume *44*

Supplemental information

Structures of the human adult muscle-type nicotinic receptor in resting and desensitized states

Anna Li, Ashley C.W. Pike, Richard Webster, Susan Maxwell, Wei-Wei Liu, Gamma Chi, Jacqueline Palace, David Beeson, David B. Sauer, and Yin Yao Dong

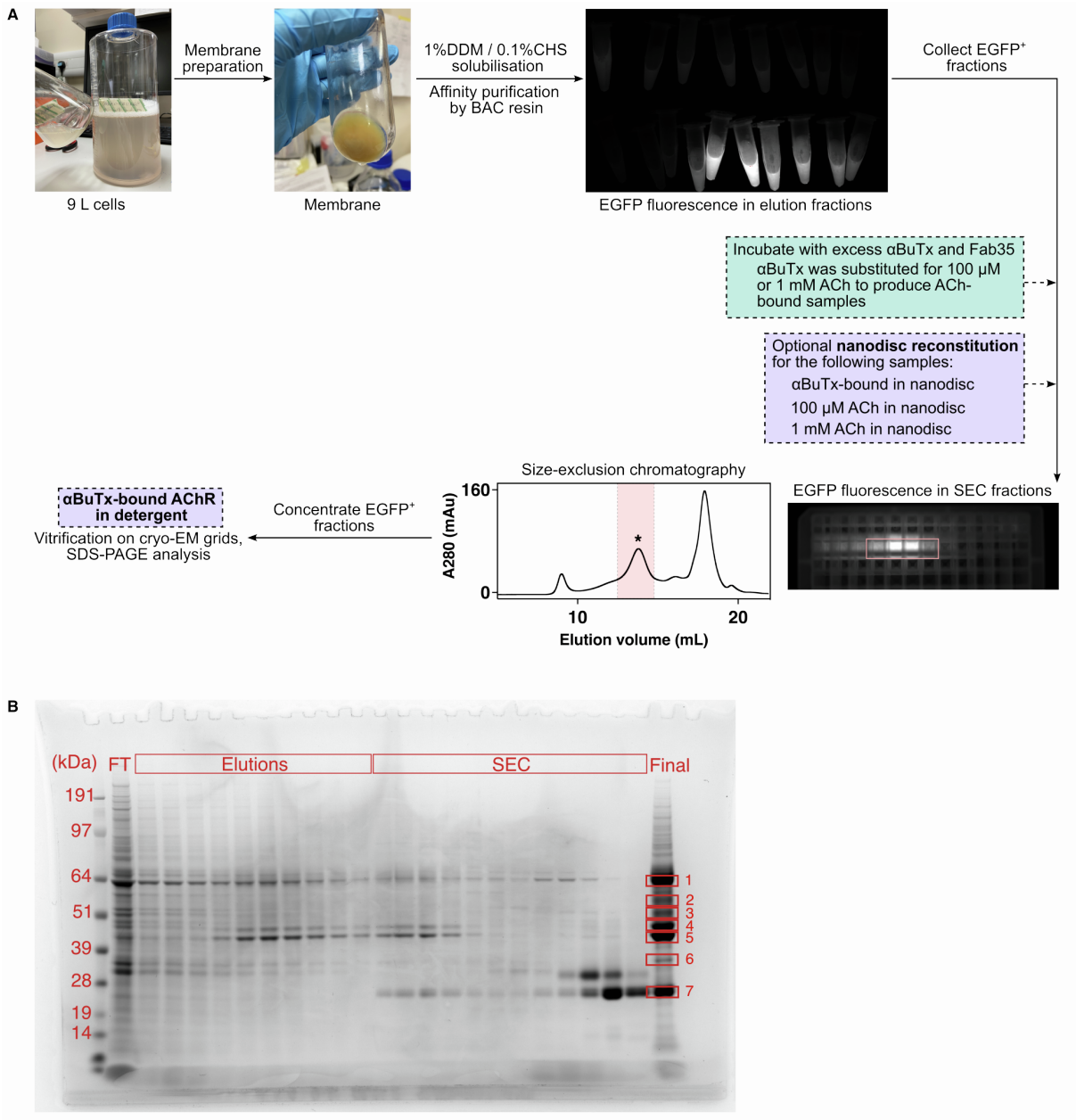

Figure S1: Expression and purification of AChR from stable cell line. (A) Purification workflow of αBuTx-bound AChR in detergent. Lilac, optional nanodisc reconstitution step was performed for the following datasets: αBuTx-bound in nanodisc, 100 μM ACh in nanodisc and 1 mM ACh in nanodisc. Turquoise, purified AChR was incubated with excess ACh instead of αBuTx to produce the ACh-bound samples. (B) SDS-PAGE of purified AChR with added Fab35, bands 1-7 (in boxes) were excised for protein identification (see Table S1).

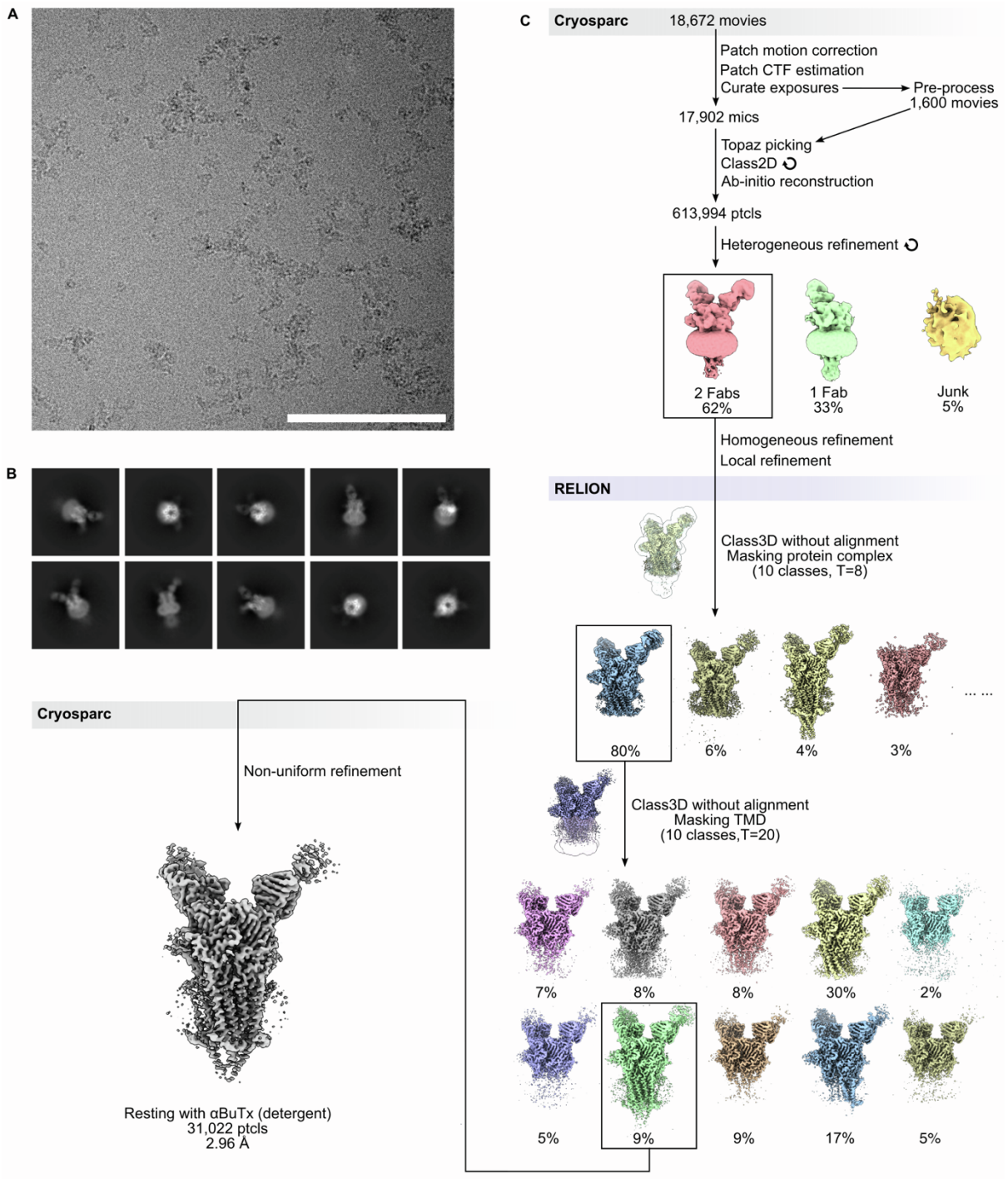

Figure S2: Cryo-EM data processing flowchart for resting state structure in detergent. (A) Representative micrograph, scale bar is 100 nm. (B) Representative 2D classes. (C) Data processing workflow. AChR particles were Topaz-picked from motion-corrected movies and subjected to 3D reconstruction and heterogeneous refinement in CryoSPARC v3.3.1[1-3]. The 2Fab particles were imported into RELION 3.1.3[4] for static Class3D with a mask covering the entire protein complex for the first round, and another mask covering the TMD for the second round. The particles were re-imported into CryoSPARC[5] for non-uniform refinement to produce a reconstruction map of 2.96 Å with 31,022 particles.

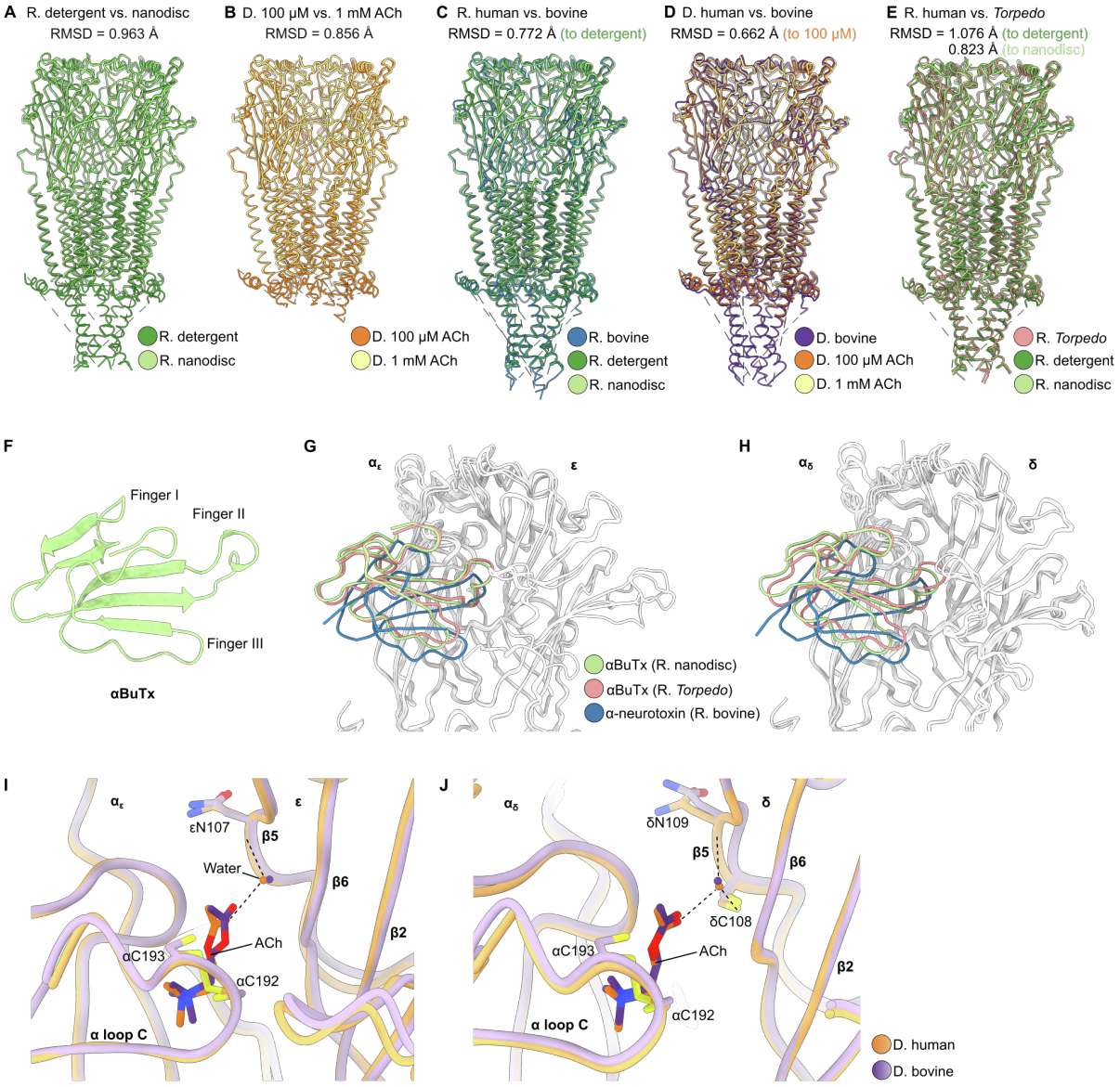

Figure S3: Comparisons of αBuTx and ACh binding to ortholog structures. (A-E) Structural overlay of two human resting state (R.) structures, two human desensitised (D.) structures, human versus bovine in the resting state (PDB: 9AVV), human versus bovine in the desensitised state (PDB: 9AWJ), and human versus *Torpedo* in the resting state (PDB: 6UWZ) [6,7]. All resting state structures are bound to α-neurotoxins. C-alpha RMSD values (in Å) are 0.963, 0.856, 0.772, 0.662 and 1.076 (to detergent) or 0.823 (to nanodisc). (F) The αBuTx is a three-finger α-neurotoxin. (G-H) An engineered α-neurotoxin binds α-ε and α-δ interfaces in a different manner to αBuTx. (I-J) ACh adopts a different pose compared a bovine AChR structure (9AWJ) possibly due to different oxidation states of the αC192-αC193 disulphide bond.

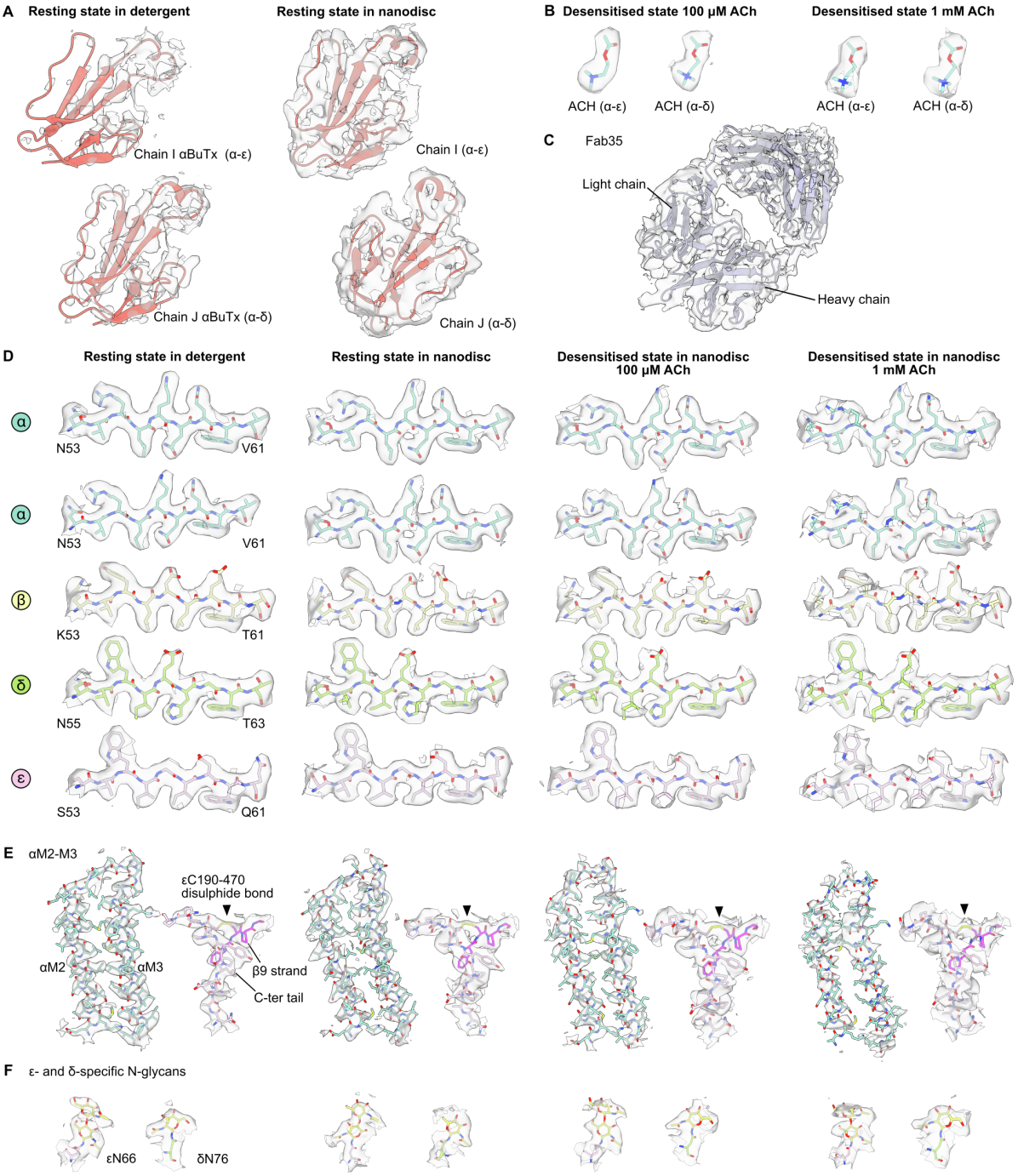

Figure S4: Cryo-EM map quality. Map quality of αBuTx (A), ACh (B), Fab35 (C), subunit signature sequence in ECD-β2 strands of the five subunits for all 4 structures (D), M2-M3 helices with ε C-terminal disulphide bond (εC190-εC470) (E), and N-glycans (F).

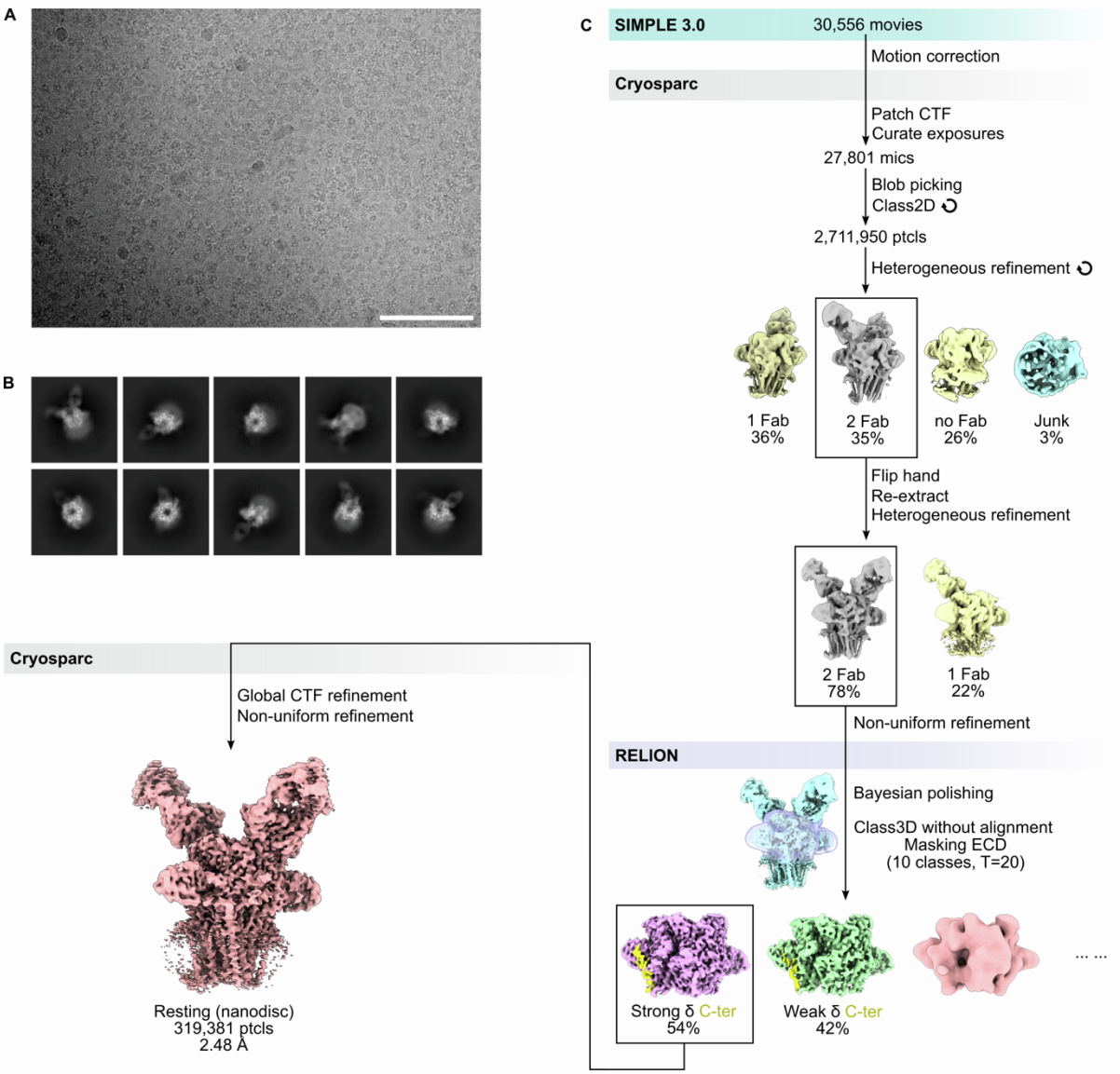

Figure S5: Cryo-EM data processing flowchart for resting state structure in nanodisc. (A) Representative micrograph, scale bar is 100 nm. (B) Representative 2D classes. (C) Data processing workflow. The classification steps were simplified compared to Figure S2 due to severe orientation bias. A mask covering the ECD was generated from initial model (see Methods) and used for RELION Class3D of 2Fab particles. This step selected for high-resolution particles with full αBuTx occupancy at both binding sites, as well as correctly aligned α-β-δ-α-ε subunits. Two high-resolution particle subclasses emerged, one with strong densities for the long δ C-terminal tail (54%) and the other with weak density for the δ signature motif (42%). The subclass with strong δ C-terminal tail density showing unambiguous subunit stoichiometry was selected for refinement, which produced a final reconstruction at 2.48 Å with 319,381 particles.

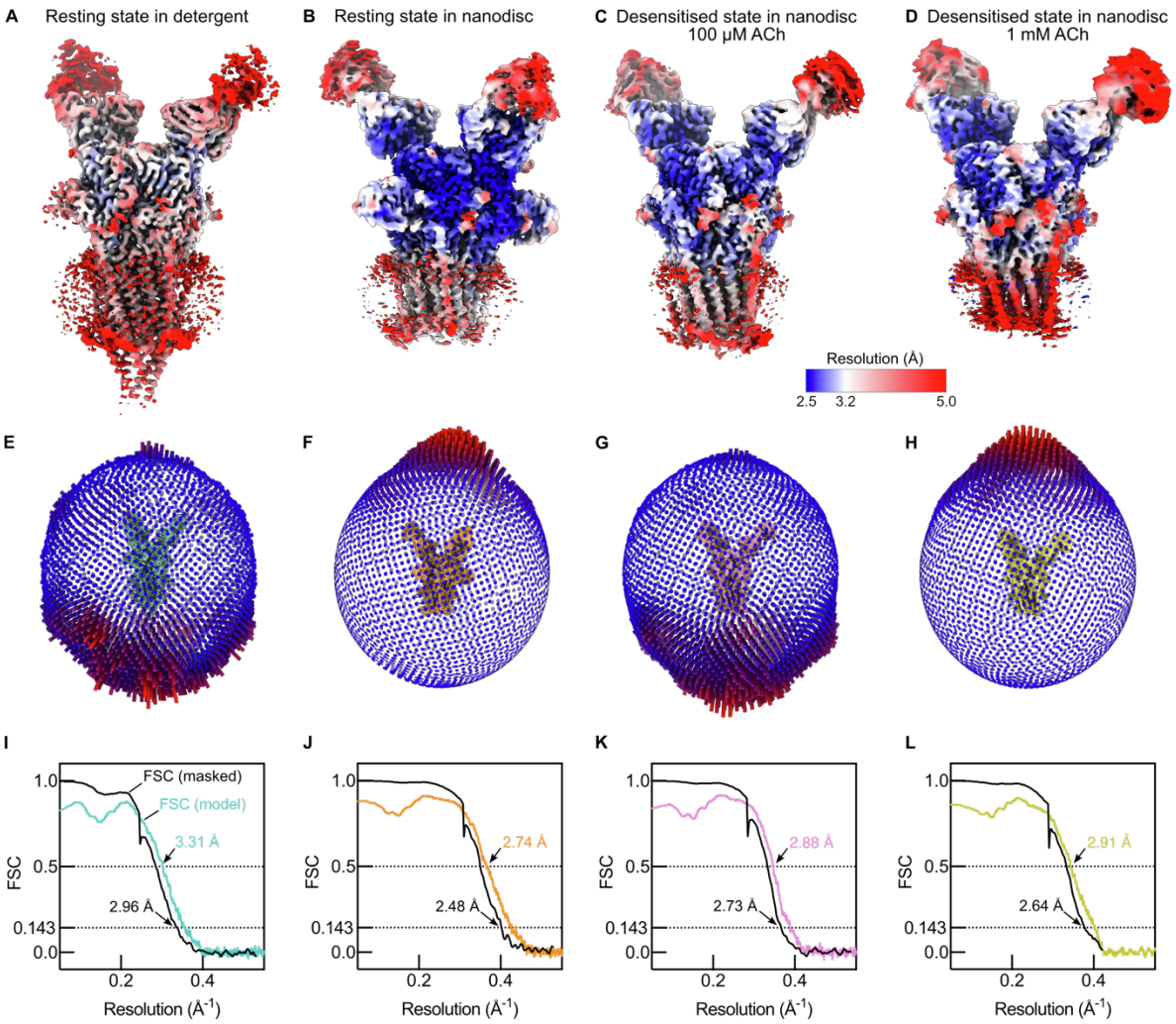

Figure S6: Cryo-EM local resolution maps, angular distribution and FSC curves. (A-D) Local resolution of cryo-EM maps. (E-H) Angular distribution of particles for each dataset. (I-L) Masked gold-standard FSC curves (black) and map-to-model FSC curves (coloured).

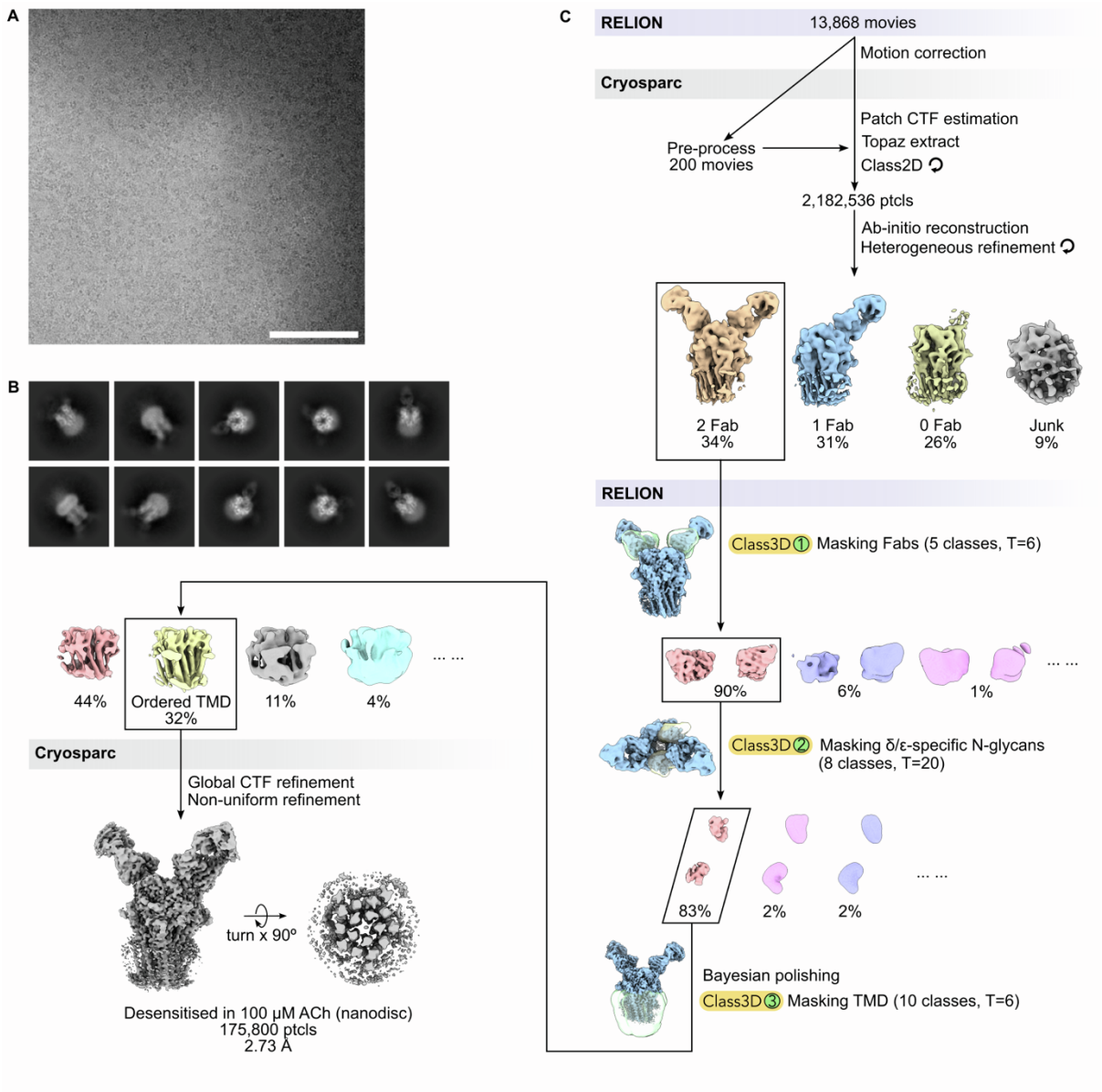

Figure S7: Cryo-EM data processing flowchart for desensitised state structure in nanodisc with 100 µM acetylcholine. (A) Representative micrograph, scale bar is 100 nm. (B) Representative 2D classes. (C) Data processing workflow. Two-Fab particles were initially isolated in CryoSPARC, then subjected to three rounds of RELION static Class3D. The first round involved a mask covering the two Fabs to select for particles with two α subunits, the second round used a different mask covering the δ/ε-specific N-glycans to ensure the resultant pentamer contains a δ or ε subunit at the correct position, and finally, the third round involved yet another mask covering the TMD to select for particle subclasses with ordered helices at the pore. From the final round of static class3D, a high-resolution particle subclass with ordered TMD (32%) emerged, and after refinement, it produced a 2.73 Å final reconstruction with 175,800 particles.

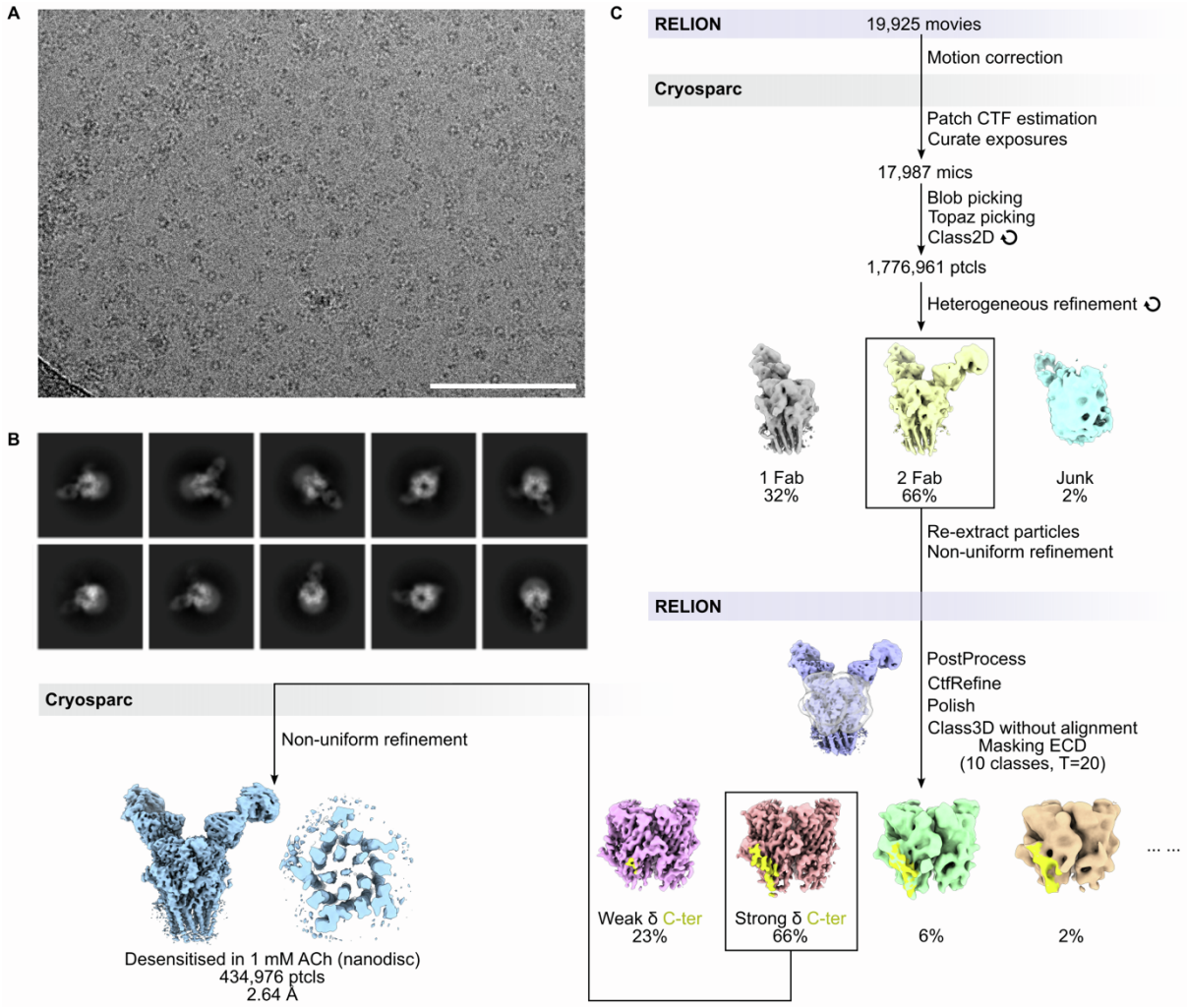

Figure S8: Cryo-EM data processing flowchart for desensitised state structure in nanodisc with 1 mM acetylcholine. (A) Representative micrograph, scale bar is 100 nm. (B) Representative 2D classes. (C) Data processing workflow. The classification steps were similar to Figure S5 due to severe orientation bias. A mask covering the ECD was used for static Class3D of 2Fab particles, which isolated a high-resolution particle subclass with strong densities for the long δ C-terminal tail (66%). Refinement of this particle subclass produced a final reconstruction at 2.64 Å with 434,976 particles.

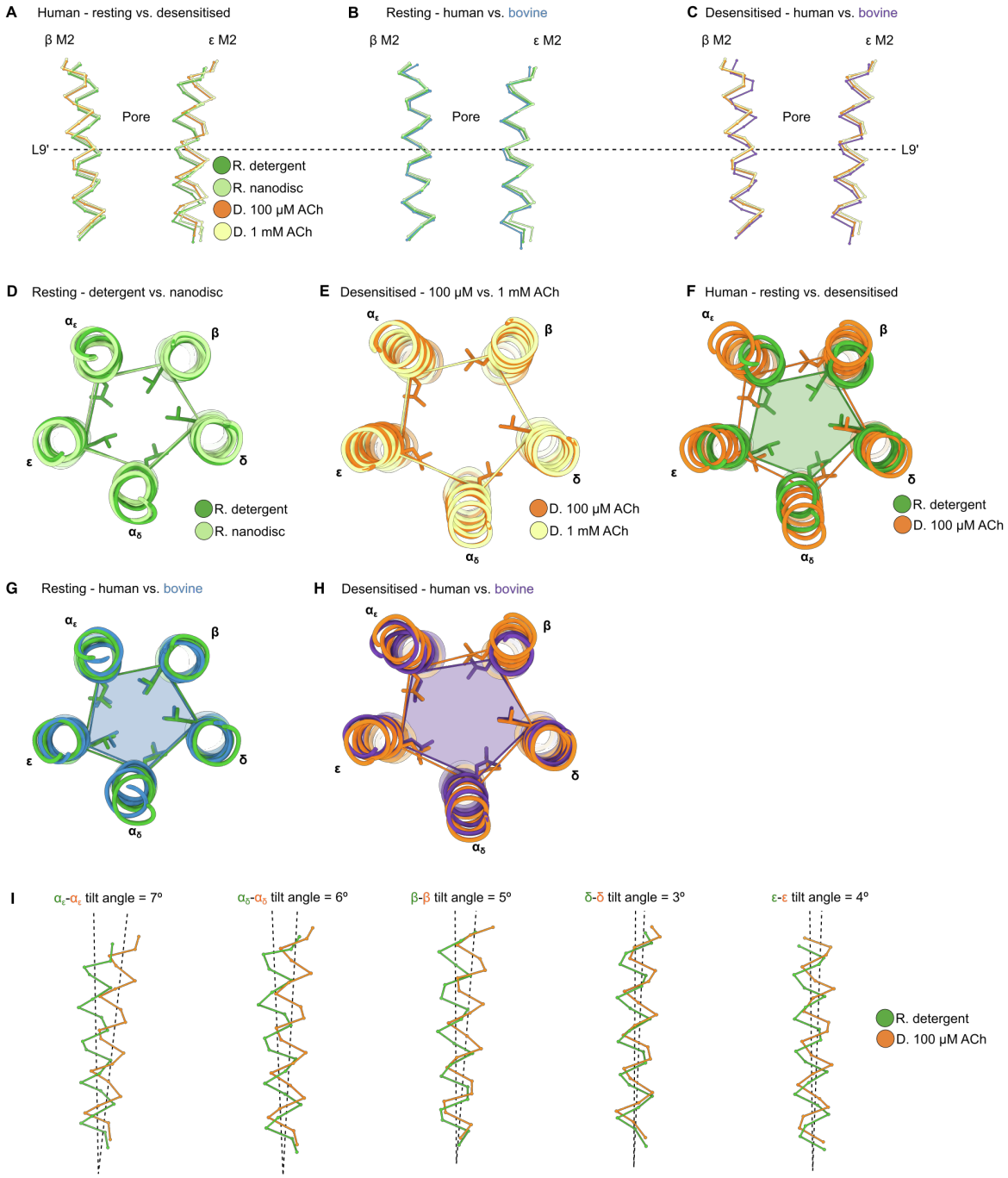

Figure S9: Comparisons of human versus bovine AChR pore conformations. Related to Figure 3F. (A) Superposition of four human receptor structures from the present study showing the cross-section at β M2 and ε M2. (B-C) Comparison of human versus bovine M2 conformations in the resting and desensitised states (PDB: 9AVV and 9AWJ)[6]. (D-E) Comparison of pore dilation at the 9' gate for the two resting and two desensitised structures. The vertices of each pentagon are positioned at C-alpha atoms of 9' leucine residues. (F) The 9' leucine residues rotate away from the pore axis in the desensitised conformation. (G) Human and bovine resting state structures show the same level of dilation at the 9' position, whereas (H) in the desensitised state, β subunit of the human receptor is located further away from the pore axis. (I) M2 tilt angles between resting and desensitised M2 helices were calculated with PyMOL (Version 1.20 Schrödinger, LLC.).

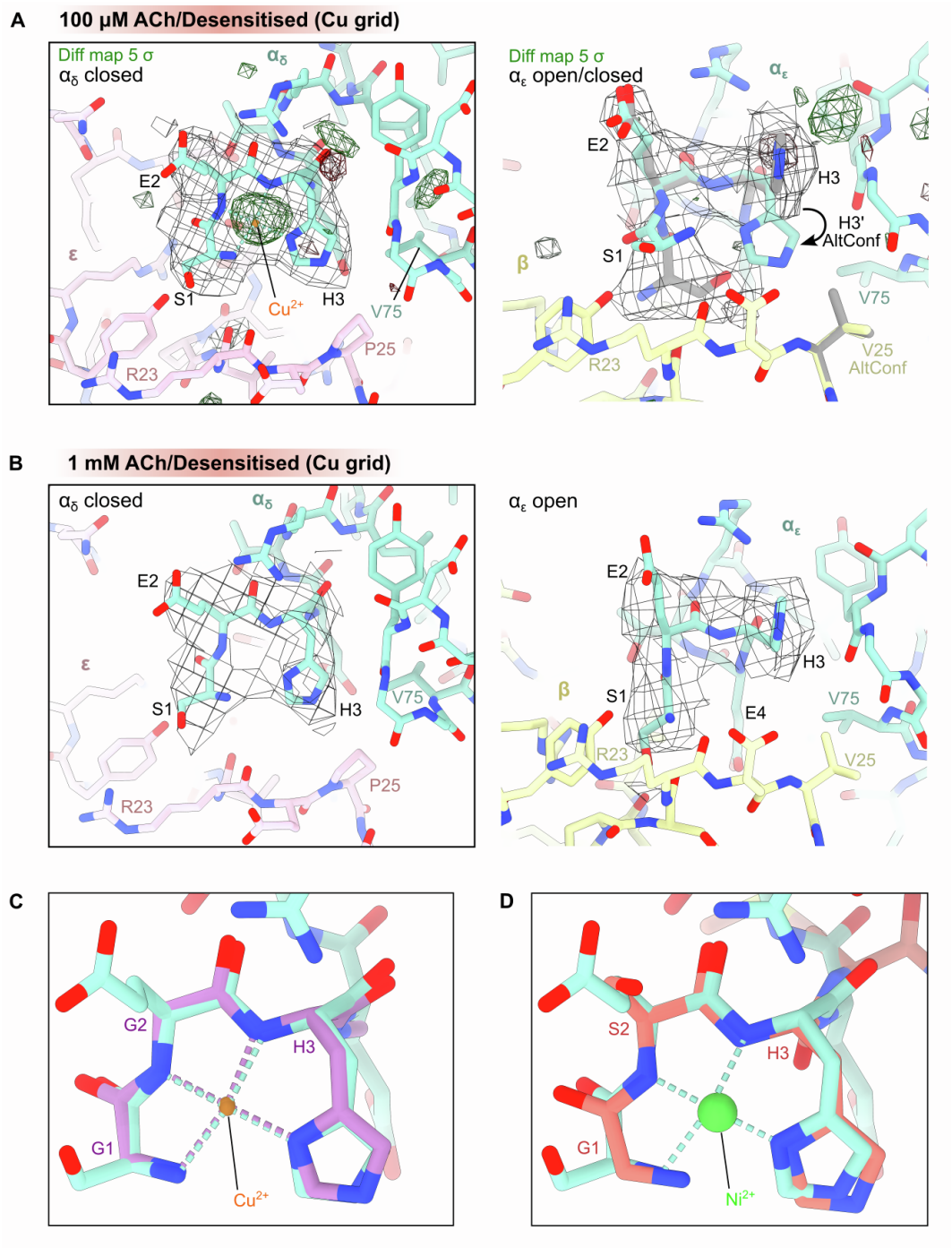

Figure S10: Comparison of amino terminal Cu^{2+} and Ni^{2+} (ATCUN) binding motifs. (A) The desensitised AChR structure in 100 µM ACh contains closed ATCUN motif (X1-X2-H3) at α_δ-ε site and open ATCUN at α_ε-β site. Alternative conformations were observed for α_εH3 and βV25. Coulomb potential maps are shown in grey, mask-normalised F_o-F_c difference maps highlighting non-protein features are shown in green (positive density) and red (negative density), calculated with Servalcat (see Methods). (B) The second desensitised structure (in 1 mM ACh) adopts closed and open conformations at corresponding sites. (C) Overlay of copper-bound glycylglycyl-L-histidine-N-methyl amide structure[8] and α_δ ATCUN motif of resting state nanodisc AChR structure, C-alpha RMSD=0.22 Å. Structure of peptide was obtained from the Cambridge Structural database[9]. (D) Overlay of ATCUN motifs on nickel-bound c-Src-SH3 domain (PDB:4RTZ) and resting state AChR, C-alpha RMSD=0.31 Å[8,10].

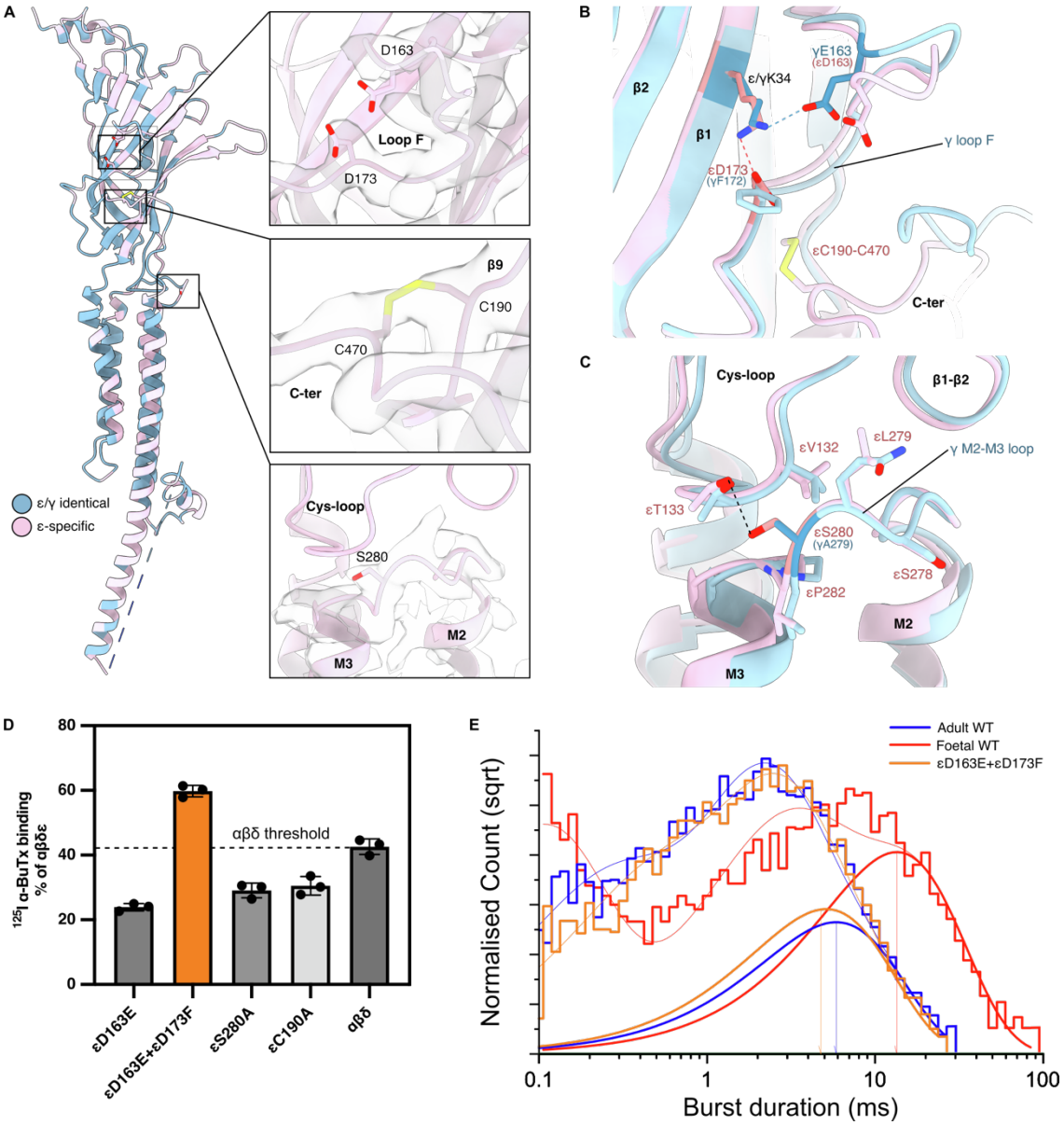

Figure S11: Characterisation of ε to γ mutants. (A) Structure of the resting state ε subunit coloured by ε-specific residues (pink) or ε/γ consensus residues. Positions of mutated ε residues on loop F (D163 and D173), β9 strand (C190), and M2-M3 loop (S280) shown on the structure. The resting state human ε subunit adopts the same conformation as the resting state bovine γ subunit (PDB: 9AWK), C-alpha RMSD=0.658[6]. (B) εD173F forms a salt bridge with εK34 in the resting state. εD163E knocks in the equivalent γ residue, and εD163E+εD173F knocks out the formation of ε-specific salt bridge. (C) εS280A transforms a key M2-M3 loop residue to the γ equivalent. (D) All mutants reduced AChR surface expression by ^{125}-I-αBuTx radioligand binding assay, mean ± SEM. (E) Burst duration histograms of ε to γ mutants, longest time constant (ms) equals 5.58±0.34, 11.28±0.73, and 4.17±1.05 for adult WT, foetal WT, and εD163E+εD173F respectively, n≥4. Related Figure 6.

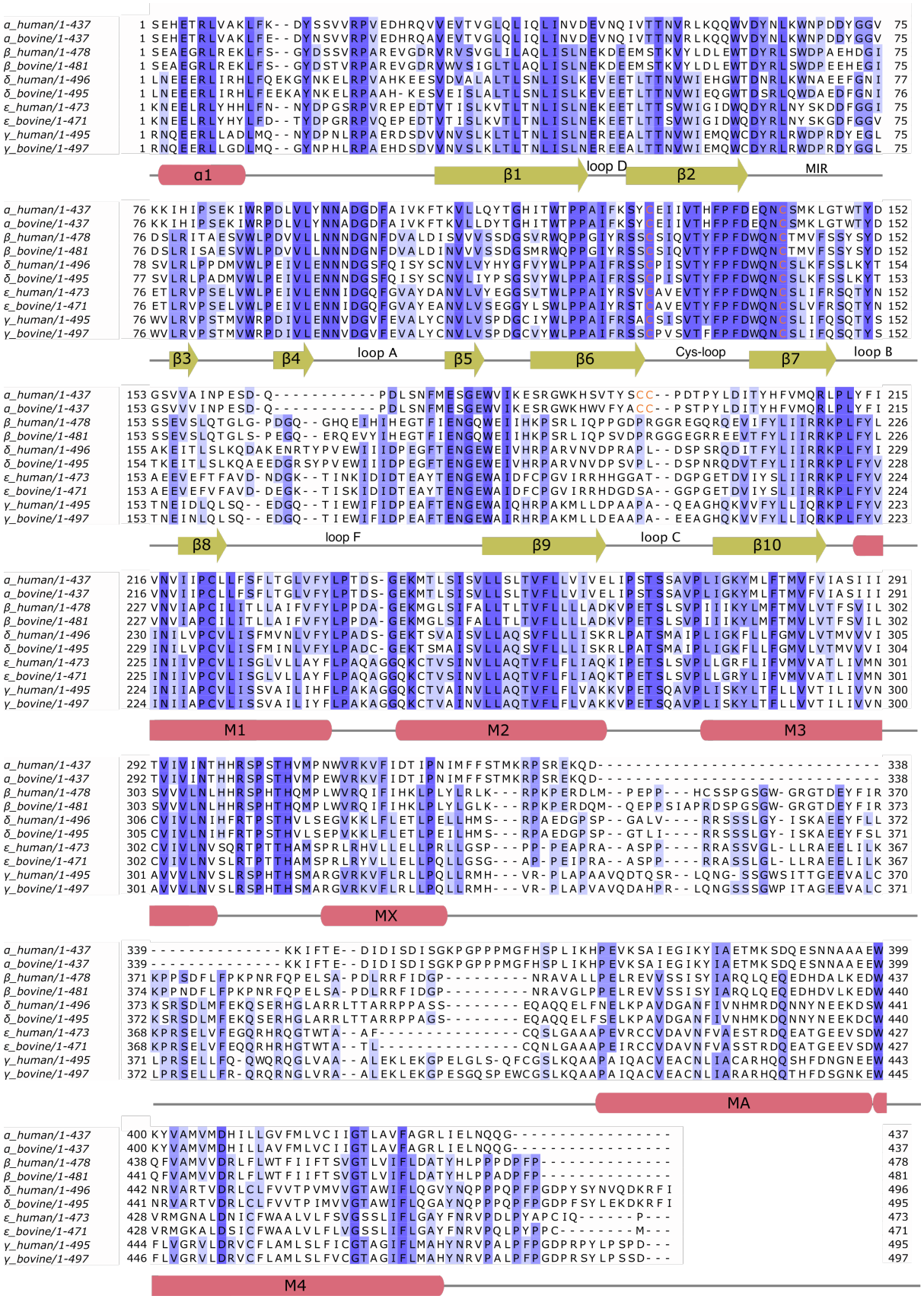

Figure S12: Sequence alignment of human versus bovine muscle-type AChR subunits. Pipes and arrows indicate approximate positions of α-helices and β-strands[7]. UniProt sequences (P02708, P02709, P11230, P04758, Q07001, P04759, Q04844, P02715, P07510, P13536)

were aligned with Tcoffee in Jalview[11]. Signal peptides were removed from residue numbering according to positions in original publications[12-17]. Cysteines involved in disulphide bonding are coloured orange.

Table S1: Protein identification by in-gel digest mass spectroscopy

Band	Protein Score	Coverage (%)	emPAI	#Significant Sequence	Average Mass	Name	Description
1	10356	41	1.68	20	54662	ACHE_HUMAN	Acetylcholine receptor subunit epsilon OS=Homo sapiens OX=9606 GN=CHRNE PE=1 SV=2
2	4214	46	1.5	20	58858	ACHD_HUMAN	Acetylcholine receptor subunit delta OS=Homo sapiens OX=9606 GN=CHRND PE=1 SV=1
3	3859	37	1.38	19	58858	ACHD_HUMAN	Acetylcholine receptor subunit delta OS=Homo sapiens OX=9606 GN=CHRND PE=1 SV=1
4	7597	37	1.24	17	56663	ACHB_HUMAN	Acetylcholine receptor subunit beta OS=Homo sapiens OX=9606 GN=CHRNB1 PE=1 SV=3
5	13193	44	1.68	19	51805	ACHA_HUMAN	Acetylcholine receptor subunit alpha OS=Homo sapiens OX=9606 GN=CHRNA1 PE=1 SV=3
6	1657	36	1.07	14	51805	ACHA_HUMAN	Acetylcholine receptor subunit alpha OS=Homo sapiens OX=9606 GN=CHRNA1 PE=1 SV=3
7	1473	28	1.41	4	11594	KACB_RAT	Ig kappa chain C region, B allele OS=Rattus norvegicus OX=10116 PE=1 SV=1

Table S2: Cryo-EM data collection, processing, refinement and validation statistics

	αBuTx-detergent (EMD-51568) (PDB 9GU0)	**αBuTx-nanodisc** (EMD-51569) (PDB 9GU1)	**100 µM ACh-nanodisc** (EMD-51570) (PDB 9GU2)	**1 mM ACh-nanodisc** (EMD-51571) (PDB 9GU3)
Data collection and processing				
Magnification	130,000	105,000	130,000	130,000
Voltage (kV)	300	300	300	300
Electron exposure (e–/Å^2)	50	46	50	52.2
Defocus range (μm)	-1.2 to -2.4	-0.8 to -2.2	-0.8 to -2.4	-1.0 to -2.2
Pixel size (Å)	0.932	0.832	0.921	0.65
Symmetry imposed	C1	C1	C1	C1
Initial particle images (no.)	696904	795093	933302	1713360
Final particle images (no.)	31022	319381	175800	434976
Map resolution (Å)	2.96	2.48	2.73	2.64
FSC threshold	0.143	0.143	0.143	0.143
Map resolution range (Å)	2.5 – 6.5	2.3 – 6.0	2.5 – 6.0	2.6 – 6.0
Refinement				
Initial model used (PDB code)	Alphafold2	9GU0	Alphafold2/ModelAngelo	9GU2
Model resolution (Å)	3.31	2.74	2.88	2.91
FSC threshold	0.5	0.5	0.5	0.5
Map sharpening *B* factor (Å^2)	-20	-25	-40	-25
Model composition				
Non-hydrogen atoms	22876	21896	21623	19563
Protein residues	2956	2740	2748	2564
Ligands	0	0	20	20
B factors (Å^2)				
Protein	113.08	128.10	114.50	162.27
Ligand	-	-	48.01	74.35
R.m.s. deviations				
Bond lengths (Å)	0.002	0.005	0.002	0.003
Bond angles (°)	0.497	0.616	0.488	0.504
Validation				
MolProbity score	1.23	1.32	1.34	1.32
Clashscore	2.46	3.63	3.38	4.47
Poor rotamers (%)	0.21	0.21	0.44	0.46
Ramachandran plot				
Favoured (%)	96.76	97.08	96.65	97.55
Allowed (%)	3.24	2.92	3.35	2.45
Disallowed (%)	0	0	0	0
Overall Q-score	0.4970	0.5060	0.4970	0.4480

Table S3: Sequence variants identified in cases of suspected congenital myasthenic syndrome

Gene	Amino acid variant (from first codon of mature peptide)	RefSeq_mRNA/hgvs_DNA/hgvs_protein
CHRNA1	αI49T	NM_000079.4 (CHRNA1): c.206C>T (p.Ile69Thr)
CHRNA1	αT133I	NM_000079.4 CHRNA1: c.458C>T (p.Thr153Ile)
CHRNA1	αT281S	NM_000079.4 (CHRNA1): c.902C>G (p.Thr301Ser)
CHRNB1	βI285S	NM_000747.3 (CHRNB1): c.923T>G (p.Ile308Ser)
CHRNB1	βV296A	NM_000747.3 (CHRNB1) c.956T>C (p.Val319Ala)
CHRND	δD180N	NM_000751.3 (CHRND): c.601G>A (p.Asp201Asn)
CHRND	δL272P	NM_000751.3 (CHRND): c.878T>C (p.Leu293Pro)
CHRNE	εS235A	NM_00080.4 (CHRNE): c.763T>G (p.Ser255Ala)

Table S4: Single channel kinetics of WT and mutant AChR expressed in HEK293T cells [a]									
Mutation	a1	τ1 (ms)	a2	τ2 (ms)	a3	τ3 (ms)	a4	τ4 (ms)	Number of patches[b]
WT adult	0.28 ± 0.01	0.14 ± 0.01	0.34 ± 0.02	1.301 ± 0.10	0.38 ± 0.01	**5.58 ± 0.34**[c]			29
WT foetal	0.39 ± 0.04	0.09 ± 0.01	0.24 ± 0.03	1.71 ± 0.38	0.38 ± 0.02	**11.28 ± 0.73**			4
αI49T	0.35 (± 0.01)	0.17 (± 0.05)	0.21 (± 0.01)	1.83 (± 0.08)	0.33 (± 0.01)	11.77 (± 0.07)	0.12 (± 0.02)	**56.96 (± 0.13)**	Combined from 4 patches
αT133I	0.49 ± 0.03	0.40 ± 0.05	0.51 ± 0.03	**1.86 ± 0.13**					5
αT281S	0.39 ± 0.02	0.14 ± 0.01	0.23 ± 0.01	1.72 ± 0.19	0.38 ± 0.01	**18.11 ± 2.43**			7
βI285S	0.33 ± 0.03	0.09 ± 0.02	0.44 ± 0.02	0.44 ± 0.07	0.23 ± 0.04	**1.81 ± 0.29**			6
βV296A	0.40 ± 0.01	0.10 ± 0.01	0.33 ± 0.01	0.98 ± 0.10	0.27 ± 0.004	**48.07 ± 2.08**			5
δD180N	0.54 ± 0.05	0.24 ± 0.01	0.46 ± 0.05	**1.05 ± 0.04**					3
δL272P	0.41 +-/ 0.03	0.17 ± 0.01	0.23 ± 0.03	3.58 ± 0.62	0.36 ± 0.03	**26.09 ± 3.43**			5
εS235A	0.42 (± 0.01)	0.39 (± 0.05)	0.24 (± 0.02)	9.19 (± 0.10)	0.34 (± 0.02)	**69.88 (± 0.07)**			Combined from 7 patches
εD163E + εD173F	0.39 ± 0.02	0.11 ± 0.01	0.32 ± 0.04	1.07 ± 0.21	0.28 ± 0.05	**4.17 ± 1.05**			6

[a] Related to Figure 4.

[b] Due to low activity in individual patches, defined bursts from multiple patches were combined and fitted to multiple exponential functions. SEM for these entries represent fitting error.

[c] Values **in bold** represent longest burst durations for each sample.

Table S5: CMS variants affecting AChR kinetics[a]	
SCCMS	**FCCMS**
αI49T[b]	**αT133I**
αG153S/A[18]	αV132L
αV156M	αV188M
αN217K	αF256L
αV249F/G[19]	αV285I
αT254I	αG378D[20]
αS269I	βP248L[21]
αG275V[22]	**βI285S**
αT281S	δE59K
αC418W	δD140N[23]
βV229F	**δD180N**
δL272P	δP250Q
βL262M	εT38K
βT265S	εW55R
βV266M/A[24]	εP121L
βV296A	εD175N
δI261T[25]	εN182Y
δS268F	εE184K
δL273F[26]	εR218W[27]
εL221F [28]	εA411P
εS235A	εc.1254ins18
εP245L[29]	εN436del
εV259L/F[30]	
εT264P	
εV265A	
εL269F[c] [31]	
εS278del[32]	

[a] Table was updated from a 2015 review article[33], related to Figure 4A.

[b] Additional CMS variants are included with reference, variants from this study are **in bold**.

[c] A separate εL269F variant arose from an unrelated family.

References

1. Bepler, T., Morin, A., Rapp, M., Brasch, J., Shapiro, L., Noble, A.J., and Berger, B. (2019). Positive-unlabeled convolutional neural networks for particle picking in cryo-electron micrographs. Nat Methods *16*, 1153-1160. 10.1038/s41592-019-0575-8.
2. Punjani, A., Rubinstein, J.L., Fleet, D.J., and Brubaker, M.A. (2017). cryoSPARC: algorithms for rapid unsupervised cryo-EM structure determination. Nat Methods *14*, 290-296. 10.1038/nmeth.4169.
3. Zheng, S.Q., Palovcak, E., Armache, J.P., Verba, K.A., Cheng, Y., and Agard, D.A. (2017). MotionCor2: anisotropic correction of beam-induced motion for improved cryo-electron microscopy. Nat Methods *14*, 331-332. 10.1038/nmeth.4193.
4. Zivanov, J., Nakane, T., Forsberg, B.O., Kimanius, D., Hagen, W.J., Lindahl, E., and Scheres, S.H. (2018). New tools for automated high-resolution cryo-EM structure determination in RELION-3. Elife *7*. 10.7554/eLife.42166.
5. Punjani, A., Zhang, H., and Fleet, D.J. (2020). Non-uniform refinement: adaptive regularization improves single-particle cryo-EM reconstruction. Nat Methods *17*, 1214-1221. 10.1038/s41592-020-00990-8.
6. Li, H., Teng, J., and Hibbs, R.E. (2024). Structural switch in acetylcholine receptors in developing muscle. Nature. 10.1038/s41586-024-07774-6.
7. Rahman, M.M., Teng, J., Worrell, B.T., Noviello, C.M., Lee, M., Karlin, A., Stowell, M.H.B., and Hibbs, R.E. (2020). Structure of the Native Muscle-type Nicotinic Receptor and Inhibition by Snake Venom Toxins. Neuron *106*, 952-962 e955. 10.1016/j.neuron.2020.03.012.
8. Camerman, N.C., A.; Sarkar, B. (1976). Molecular design to mimic the copper(II) transport site of human albumin. The crystal and molecular structure of copper(II) – glycylglycyl-L-histidine-N-methyl amide monoaquo complex. Canadian Journal of Chemistry *54*, 1309-1316. 10.1139/v76-185.
9. Groom, C.R., Bruno, I.J., Lightfoot, M.P., and Ward, S.C. (2016). The Cambridge Structural Database. Acta Crystallogr B Struct Sci Cryst Eng Mater *72*, 171-179. 10.1107/S2052520616003954.
10. Camara-Artigas, A. (2014). Crystal structure of the c-Src-SH3 domain in complex with the high affinity peptide VSL12. https://doi.org/10.2210/pdb4RTZ/pdb.
11. Troshin, P.V., Procter, J.B., and Barton, G.J. (2011). Java bioinformatics analysis web services for multiple sequence alignment--JABAWS:MSA. Bioinformatics *27*, 2001-2002. 10.1093/bioinformatics/btr304.
12. Beeson, D., Brydson, M., Betty, M., Jeremiah, S., Povey, S., Vincent, A., and Newsom-Davis, J. (1993). Primary structure of the human muscle acetylcholine receptor. cDNA cloning of the gamma and epsilon subunits. Eur J Biochem *215*, 229-238. 10.1111/j.1432-1033.1993.tb18027.x.
13. Beeson, D., Brydson, M., and Newsom-Davis, J. (1989). Nucleotide sequence of human muscle acetylcholine receptor beta-subunit. Nucleic Acids Res *17*, 4391. 10.1093/nar/17.11.4391.
14. Luther, M.A., Schoepfer, R., Whiting, P., Casey, B., Blatt, Y., Montal, M.S., Montal, M., and Linstrom, J. (1989). A muscle acetylcholine receptor is expressed in the human cerebellar medulloblastoma cell line TE671. J Neurosci *9*, 1082-1096. 10.1523/JNEUROSCI.09-03-01082.1989.
15. Noda, M., Furutani, Y., Takahashi, H., Toyosato, M., Tanabe, T., Shimizu, S., Kikyotani, S., Kayano, T., Hirose, T., Inayama, S., and et al. (1983). Cloning and sequence analysis of calf cDNA and human genomic DNA encoding alpha-subunit precursor of muscle acetylcholine receptor. Nature *305*, 818-823. 10.1038/305818a0.

16. Schoepfer, R., Luther, M., and Lindstrom, J. (1988). The human medulloblastoma cell line TE671 expresses a muscle-like acetylcholine receptor. Cloning of the alpha-subunit cDNA. FEBS Lett *226*, 235-240. 10.1016/0014-5793(88)81430-3.
17. Shibahara, S., Kubo, T., Perski, H.J., Takahashi, H., Noda, M., and Numa, S. (1985). Cloning and sequence analysis of human genomic DNA encoding gamma subunit precursor of muscle acetylcholine receptor. Eur J Biochem *146*, 15-22. 10.1111/j.1432-1033.1985.tb08614.x.
18. Dejthevaporn, C., Wetchaphanphesat, S., Pulkes, T., Rattanasiri, S., Engel, A.G., and Witoonpanich, R. (2022). Treatment of slow-channel congenital myasthenic syndrome in a Thai family with fluoxetine. J Clin Neurosci *96*, 85-89. 10.1016/j.jocn.2021.12.016.
19. Gooneratne, I.K., Nandasiri, S., Maxwell, S., Webster, R., Cossins, J., Beeson, D., Gunaratne, K., Herath, L., Senanayake, S., and Chang, T. (2021). Slow-Channel Congenital Myasthenic Syndrome due to a Novel Mutation in the Acetylcholine Receptor Alpha Subunit in a South Asian: A Case Report. J Neuromuscul Dis *8*, 163-167. 10.3233/JND-200566.
20. Brugnoni, R., Maggi, L., Canioni, E., Moroni, I., Pantaleoni, C., D'Arrigo, S., Riva, D., Cornelio, F., Bernasconi, P., and Mantegazza, R. (2010). Identification of previously unreported mutations in CHRNA1, CHRNE and RAPSN genes in three unrelated Italian patients with congenital myasthenic syndromes. J Neurol *257*, 1119-1123. 10.1007/s00415-010-5472-0.
21. Shen, X.M., Di, L., Shen, S., Zhao, Y., Neumeyer, A.M., Selcen, D., Sine, S.M., and Engel, A.G. (2020). A novel fast-channel myasthenia caused by mutation in beta subunit of AChR reveals subunit-specific contribution of the intracellular M1-M2 linker to channel gating. Exp Neurol *331*, 113375. 10.1016/j.expneurol.2020.113375.
22. Peyer, A.K., Abicht, A., Heinimann, K., Sinnreich, M., and Fischer, D. (2013). Quinine sulfate as a therapeutic option in a patient with slow channel congenital myasthenic syndrome. Neuromuscul Disord *23*, 571-574. 10.1016/j.nmd.2013.04.001.
23. Kondo, H., Tsuji, Y., Lee, T., Saito, Y., and Nishino, I. (2022). Severe congenital myasthenic syndrome with novel variants in the CHRND gene. Pediatr Int *64*, e15342. 10.1111/ped.15342.
24. Shen, X.M., Okuno, T., Milone, M., Otsuka, K., Takahashi, K., Komaki, H., Giles, E., Ohno, K., and Engel, A.G. (2016). Mutations Causing Slow-Channel Myasthenia Reveal That a Valine Ring in the Channel Pore of Muscle AChR is Optimized for Stabilizing Channel Gating. Hum Mutat *37*, 1051-1059. 10.1002/humu.23043.
25. Tawara, N., Yamashita, S., Takamatsu, K., Yamasaki, Y., Mukaino, A., Nakane, S., Farshadyeganeh, P., Ohno, K., and Ando, Y. (2021). Efficacy of salbutamol monotherapy in slow-channel congenital myasthenic syndrome caused by a novel mutation in CHRND. Muscle Nerve *63*, E30-E32. 10.1002/mus.27166.
26. Shen, X.M., Milone, M., Wang, H.L., Banwell, B., Selcen, D., Sine, S.M., and Engel, A.G. (2019). Slow-channel myasthenia due to novel mutation in M2 domain of AChR delta subunit. Ann Clin Transl Neurol *6*, 2066-2078. 10.1002/acn3.50902.
27. Shen, X.M., Brengman, J.M., Shen, S., Durmus, H., Preethish-Kumar, V., Yuceyar, N., Vengalil, S., Nalini, A., Deymeer, F., Sine, S.M., and Engel, A.G. (2018). Mutations causing congenital myasthenia reveal principal coupling pathway in the acetylcholine receptor epsilon-subunit. JCI Insight *3*. 10.1172/jci.insight.97826.
28. Croxen, R., Hatton, C., Shelley, C., Brydson, M., Chauplannaz, G., Oosterhuis, H., Vincent, A., Newsom-Davis, J., Colquhoun, D., and Beeson, D. (2002). Recessive inheritance and variable penetrance of slow-channel congenital myasthenic syndromes. Neurology *59*, 162-168. 10.1212/wnl.59.2.162.

29. Ohno, K., Quiram, P.A., Milone, M., Wang, H.L., Harper, M.C., Pruitt, J.N., 2nd, Brengman, J.M., Pao, L., Fischbeck, K.H., Crawford, T.O., et al. (1997). Congenital myasthenic syndromes due to heteroallelic nonsense/missense mutations in the acetylcholine receptor epsilon subunit gene: identification and functional characterization of six new mutations. Hum Mol Genet *6*, 753-766. 10.1093/hmg/6.5.753.
30. Fidzianska, A., Ryniewicz, B., Shen, X.M., and Engel, A.G. (2005). IBM-type inclusions in a patient with slow-channel syndrome caused by a mutation in the AChR epsilon subunit. Neuromuscul Disord *15*, 753-759. 10.1016/j.nmd.2005.07.009.
31. Tan, J.Z., Man, Y., and Xiao, F. (2016). A Missense Mutation in Epsilon-subunit of Acetylcholine Receptor Causing Autosomal Dominant Slow-channel Congenital Myasthenic Syndrome in a Chinese Family. Chin Med J (Engl) *129*, 2596-2602. 10.4103/0366-6999.192780.
32. Finlayson, S., Spillane, J., Kullmann, D.M., Howard, R., Webster, R., Palace, J., and Beeson, D. (2013). Slow channel congenital myasthenic syndrome responsive to a combination of fluoxetine and salbutamol. Muscle Nerve *47*, 279-282. 10.1002/mus.23534.
33. Engel, A.G., Shen, X.M., Selcen, D., and Sine, S.M. (2015). Congenital myasthenic syndromes: pathogenesis, diagnosis, and treatment. Lancet Neurol *14*, 461. 10.1016/S1474-4422(15)00010-1.